Buoyant miscible displacement flows of Newtonian and non-Newtonian fluids: stationary and oscillating geometries

Thèse

Amin Amiri

Doctorat en génie chimique
Philosophiæ doctor (Ph. D.)

Québec, Canada

Buoyant miscible displacement flows of Newtonian and non-Newtonian fluids: stationary and oscillating geometries

Thèse

Amin Amiri

Sous la direction de:

Seyed Mohammad Taghavi, directeur de recherche
Faïçal Larachi, codirecteur de recherche

Résumé

Cette thèse vise l'étude des écoulement de déplacement de fluides miscibles à l'intérieur d'un long tuyau stationnaire vertical et d'un tuyau en mouvement. Concernant la géométrie des mouvements, le tuyau oscille comme un pendule inversé avec une fréquence maximale faible, c'est-à-dire, $\hat{f} = 0.2$ (Hz) et une oscillation maximale de faible amplitude, soit 15 (°) par rapport à l'axe du tuyau. Les écoulement de déplacement se produisent à un nombre de Péclet élevé et aux petits nombres d'Atwood. L'accent est mis sur les types de fluides et de géométries (tuyau fixe ou en mouvement). Les approches expérimentales détaillées sont utilisées de manière intégrée. Dans cette thèse, la configuration de densité est la densité instable. La majeure partie des travaux en cours se concentre sur les écoulements de déplacement de fluides Newtoniens isovisqueux, mais nous étudions également l'écoulement de déplacement à contrainte au seuil de plasticité dans un long tuyau vertical.

Pour un écoulement de déplacement Newtonien isovisqueux dans un tuyau stationnaire, nous remarquons un effet stabilisant imposé au débit principal et signalant l'existence de deux régimes d'écoulement principaux à long moment introduits par un écoulement de déplacement stable et un écoulement de déplacement instable. La transition entre ces deux régimes se produit à un nombre critique de Reynolds modifié ($Re_t|_{Critical}$), en fonction du nombre de Froude (Fr). En étudiant en détail le régime d'écoulement stable : nous constatons que, premièrement, le modèle de lubrification, associé à une simple formule d'accélération initiale, suggère une prédiction de la vitesse frontale de déplacement pénétrante dépendante du temps et que, deuxièmement, deux sous-régimes sont remarqués pour l'écoulement de déplacement stable, à savoir les écoulement à reécoulement prolongé et les écoulement à reécoulement non prolongé. La transition entre les deux sous-régimes est un état d'écoulement d'interface stationnaire marginal, qui est également bien prédit par le modèle de lubrification.

Pour l'écoulement de déplacement newtonien isovisqueux dans le tuyau en mouvement, trois régimes d'écoulement différents sont introduits : un écoulement stable non diffusif (à $Re/Ro < 70$ & $Re_t/Fr < 35$), un écoulement stable diffusif (à $Re/Ro > 70$ & $Re_t/Fr < 35$) et un écoulement instable diffusif (à $Re_t/Fr > 35$) où Re, Re_t et Ro représentent le nombre de Reynolds, le nombre de Reynolds modifié et le nombre de Rossby, respectivement. De plus, les vitesses frontales pénétrantes ainsi que les coefficients de diffusion macroscopiques sont mesurés. Les résultats indiquent clairement qu'en fonction de la valeur de la différence de densité et de la vitesse moyenne d'écoulement imposée, les mouvements géométries peuvent avoir des effets différents et même opposés, par exemple, une augmentation ou une diminution légère de la vitesse frontale. Le mouvement du tuyau semble également augmenter légèrement le coefficient de diffusion macroscopique.

Enfin, pour le rendement des écoulement de déplacement à contrainte au seuil de plasticité dans la conduite fixe, deux régimes principaux sont observés en fonction du nombre de Bingham Newtonien (B_N) : un régime de couches résiduelles en mouvement (pour $B_N < 100$) et un régime de couches résiduelles stationnaires (pour $B_N > 100$). En outre, cinq sous-régimes sont identifiés. Les transitions entre ces sous-régimes sont des fonctions de nombre de Reynolds effectif (Re_N^*), nombre de flottabilité (χ) et Re_N/Fr. En fonction des valeurs de la limite de contrainte au seuil de plasticité, les résultats montrent que la force de flottabilité indique des effets différents sur le comportement d'écoulement de déplacement. De plus, nous pourrions prédire certains comportements d'écoulement en utilisant un modèle de lubrification, par exemple la transition entre des couches résiduelles stationnaires et en mouvement. Enfin, nous utilisons des simulations numériques de la dynamique des fluides dans une géométrie 2D, permettant de prédire certains des comportements d'écoulement clés.

Abstract

This thesis aims to investigate buoyant displacement flows of miscible fluids in a long, vertical stationary pipe or a moving pipe. For the case of the moving geometry, the pipe oscillates like an inverted pendulum with a small maximum frequency, i.e. $\hat{f} = 0.2$ (Hz) and a small maximum oscillation amplitude, i.e. 15 (°) with respect to the pipe axis. The displacement flows occur at the high Péclet number and small Atwood numbers. The focus is on the type of fluids and geometries (stationary or moving pipe). Detailed experimental approaches are employed in an integrated fashion. The density configuration in this thesis is the density unstable. The main part of the current work is concentrated on displacement flows of iso-viscous Newtonian fluids. We also study the yield stress displacement flow in a long vertical pipe.

For iso-viscous Newtonian displacement flow in a stationary pipe, we uncover the stabilizing effect of the mean imposed flow and report the existence of two main flow regimes at long times introduced as a stable displacement flow and an unstable displacement flow. The transition between these two regimes occurs at a critical modified Reynolds number ($Re_t|_{Critical}$), as a function of Froude number (Fr). We investigate deeply the stable flow regime: first, a lubrication model combined with a simple initial acceleration formulation suggests a prediction of the time-dependent penetrating displacing front velocity. Second, we find two sub-regimes for the stable displacement flow, namely sustained-back-flows and no-sustained-back-flows. The transition between the two sub-regimes is a marginal stationary interface flow state, which is also well predicted by the lubrication model.

For the iso-viscous Newtonian displacement flow in the moving pipe, three different flow regimes are introduced: a stable flow that is non-diffusive (at $Re/Ro < 70$ & $Re_t/Fr < 35$), a stable-diffusive flow (at $Re/Ro > 70$ & $Re_t/Fr < 35$) and an unstable-diffusive flow (at $Re_t/Fr > 35$) where Re, Re_t and Ro represent the Reynolds number, the modified Reynolds number, and the Rossby number, respectively. In addition, penetrating front velocities as well as macroscopic diffusion coefficients are measured. The results indicate that depending on the value of the density difference and the mean imposed flow velocity, the geometrical movements can have different and even opposite effects, e.g. slightly increase or decrease the front velocity. The pipe motion seems to also slightly increase the macroscopic diffusion coefficient.

Finally, for the yield stress displacement flow in the stationary pipe, two main flow regimes are observed as a function of the Newtonian Bingham number (B_N): a moving residual layer regime (for $B_N < 100$) and a stationary residual layer regime (for $B_N > 100$). In addition, five sub-regimes are identified. The transitions between these sub-regimes are functions of effective Reynolds number (Re_N^*), Buoyancy number (χ), and Re_N/Fr. Depending on yield stress values, the results show that the buoyancy force has different effects on the displacement flow behaviour. Moreover, we could predict some of the flow behaviours using a lubrication model, e.g. the transition between stationary and moving residual layers. Finally, we use computational fluid dynamics simulations in a 2D geometry, predicting some of the key flow behaviours.

Table of contents

List of tables

List of figures

Nomenclature

At	Atwood number
B_N	Newtonian Bingham number
B_N^*	effective Bingham number
c	dimensionless fluid concentration
C	dimensionless concentration
$\bar{C}_x$	averaged concentration with respect to x
$\bar{C}_{xy}$	averaged concentration with respect to x & y
$\bar{C}_{xyz}$	averaged concentration with respect to x, y & z
$\hat{D}$	pipe diameter, m
$\hat{D}_m$	molecular diffusivity, m^2/s
$\hat{D}_M$	macroscopic diffusion coefficient, m^2/s
$\hat{D}_M^s$	pseudo macroscopic diffusion coefficient, m^2/s
$\hat{f}$	pipe motion angular frequency, 1/s
Fr	densimetric Froude number
$\hat{g}$	acceleration due to gravity, m/s^2
$\hat{L}$	length of the pipe, m
$\hat{L_d}$	pipe length below the gate valve, m
$\hat{L_u}$	pipe length above the gate valve, m
$\hat{Q}$	flow rate, m^3/s
m	viscosity ratio
m^*	effective viscosity ratio
n	power-law index
p	dimensionless pressure
Pe	Péclet number
Re	Reynolds number
Re_h	hydraulic Reynolds number
Re_N	Newtonian Reynolds number
Re_N^*	effective Reynolds number
Re_t	modified Reynolds number
Ro	Rossby number
$\mathbf{u}$	dimensionless fluid velocity vector

V_f	dimensionless front velocity
$\hat{V}_f$	front velocity, m/s
$\hat{V}_t$	characteristic inertial velocity, m/s
$\hat{V}_\nu$	characteristic viscous velocity, m/s
$\hat{V}_0$	mean imposed flow velocity, m/s
V^*	dimensionless terminal velocity
$(\hat{x}, \hat{y}, \hat{z})$	Cartesian coordinates, m
$(\hat{r}, \hat{\theta}, \hat{z})$	cylindrical coordinates, m
$\hat{z}_0$	radial distance between the gate valve & the rotation center
Z_0	characteristic dimensionless radial distance between the gate valve & rotation center

Greek letters

$\mathscr{A}$	pipe oscillation (rotation) maximum amplitude
β	pipe inclination angle
δ	ratio of pipe diameter to pipe length
$\hat{\mu}$	fluid dynamic viscosity, Pa.s
μ^*	viscosity ratio
$\hat{\kappa}$	fluid consistency index, Pa.s^n
$\hat{\nu}$	fluid kinematic viscosity, m^2/s
$\hat{\rho}$	fluid density, kg/m^3
$\hat{\bar{\rho}}$	mean density, kg/m^3
$\hat{\tau}_y$	yield stress, Pa
$\hat{\omega}_0$	pipe motion angular speed, rad/s
Ω	dimensionless rotation vector
$\Re$	normalized dimensionless position vector
ϕ	linear interpolation function
χ	buoyancy number

Subscripts

f	front position
H	heavy displacing fluid
L	light displaced fluid
s	stationary interface
t	derivative with respect to time

Superscripts

Lub	lubrication model

Dedicated to my lovely wife and
my beloved parents for their love,
endless support, encouragement
& sacrifices

You can never cross the ocean
unless you have the courage to
lose sight of the shore.

Christopher Columbus

Acknowledgement

Firstly, I would like to specify my sincere gratitude to my loving wife Sara for her immense support during this long way. I also express my deep and sincere gratitude to my father, my mother, and my family for supporting me spiritually in the whole period of my life.

I would like to gratefully and sincerely thank my supervisor, Prof. Seyed Mohammad Taghavi, for his guidance, patience, and most importantly, his support and help during my Ph.D. I also thank my co-supervisor, Prof. Faïçal Larachi, for the continuous support of my Ph.D. study.

I thank Jérôme Noël, Jean-Nicolas Ouellet, and Marc Lavoie, technicians at the Chemical Engineering Department, for their help in the construction of the experimental apparatus and for the very useful technical discussions. I thank Roozbeh Mollaabbasi (postdoctoral fellow) for assisting in calibrating the experimental apparatus and performing some preliminary experiments. I would like to thank Ali Eslami for valuable discussions in the rheology part. I also express my thank to all my friends at Laval University for their support.

Finally, I acknowledge the generous support of the Discovery Grant of the Natural Sciences and Engineering Research Council of Canada (NSERC) and of the Canada Foundation for Innovation (CFI). I also appreciate the partial scholarship support for me which was provided by Université Laval Aluminium Research Centre (REGAL-Laval).

Foreword

This thesis consists of different chapters. First, the introduction and background are presented which have been originally written by Amin Amiri and have never been published before. Chapters 1-3 include the results of this study presented in the form of scientific articles. Finally, the general finding and recommendations are highlighted for future studies. This thesis was supervised by Prof. Seyed Mohammad Taghavi (my supervisor) and Prof. Faïçal Larachi (my co-supervisor). The articles are listed below:

[1] A. Amiri, F. Larachi, S. M. Taghavi, Buoyant miscible displacement flows in vertical pipe. *Physics of Fluids*, 28, 102105, 2016.

[2] A. Amiri, F. Larachi, S. M. Taghavi, Displacement flows in periodically moving pipe: Understanding multiphase flows hosted in oscillating geometry. *Chemical Engineering Science*, 170, 437-450, 2017.

[3] A. Amiri, A. Eslami, R. Mollaabbasi, F. Larachi, S. M. Taghavi, Removal of a yield stress fluid by a heavier Newtonian fluid in a vertical pipe. *Journal of Non-Newtonian Fluid Mechanics*, 268, 81-100, 2019.

Some results in this thesis were presented in the following conferences:

[1] A. Amiri, F. Larachi, S. M. Taghavi, Displacement flows of viscoplastic fluids in an oscillating pipe. *Congress of Theoretical and Applied Mechanics*, Montreal, Canada, August 21-26, 2016.

[2] A. Amiri, F. Larachi, S. M. Taghavi, The effects of geometry movement on non-Newtonian displacement flows. *66th Canadian Chemical Engineering Conference*, Quebec, Canada, October 16-19, 2016.

[3] A. Amiri, F. Larachi, S. M. Taghavi, Displacement flows in a moving pipe: understanding multiphase flows hosted in a moving geometry. *13th International Conference on Gas-Liquid and Gas-Liquid-Solid Reactor Engineering*, Crown Plaza, Brussels, Belgium, May 27-30, 2017.

[4] A. Amiri, R. Mollaabbasi, An experimental study of yield stress displacement flows in a moving annulus. *Proceedings of the Canadian Society for Mechanical Engineering International*

Congress 2018, Toronto, On, Canada, August 20-23, 2018.

Introduction

I Synopsis

I.I Problem of study

This thesis aims to investigate buoyant displacement flows of miscible fluids in stationary or moving geometries. The density configuration is the density unstable configuration (a light fluid is displaced by a heavy fluid). Although a significant driving force in this study is the buoyancy force, a mean flow is imposed in the downward direction. The effects of the mean imposed flow velocity ($\hat{V}_0$), the density difference, defined by the Atwood number ($At = \frac{\hat{\rho}_H - \hat{\rho}_L}{\hat{\rho}_H + \hat{\rho}_L}$, $\hat{\rho}_H$ and $\hat{\rho}_L$ are the densities of heavy and light fluids, respectively) [1], rheology of fluids and geometry (stationary or moving) are studied. The imposed flow is generally laminar. The pipe aspect ratio is large enough and satisfies $\delta^{-1} = \frac{\hat{L}}{\hat{D}} \gg 1$ in which $\hat{L}$ and $\hat{D}$ are the pipe length and the pipe diameter, respectively. The initial interface is placed far away from both ends of the pipe and it is transverse to the pipe axis. Fluids employed in this work are Newtonian and yield stress fluids. Fig. I indicates a schematic view of the problem.

Displacement flows of one fluid by another one are common in the oil and gas industries such as well cementing, in order to remove gelled drilling fluid from the walls of a well (1; 2; 3), food industries (4; 5), nature (6), plastic manufacturing (7), and other applications (8; 9; 10; 11). Our focus is on the displacement flows in the oil and gas industries. These processes are either related to well construction (e.g. primary cementing process in which cement slurry displaces drilling fluid) or production (e.g. pipelining), as well as in other parts of the oil and gas industries (e.g. Floating Production Storage and Offloading (FPSO)). In this thesis, we attempt to understand the principal mechanisms of displacement flows. It helps us to design a displacement flow process as effective as possible. From a fluid mechanics perspective, in the primary cementing process, it would be desirable to displace as much drilling fluid as possible by pumping as little cement slurry as required. Let us note that in all these processes, the flow is often laminar and the fluids are mostly non-Newtonian.

Understanding the physical and parametric complexity of the displacement flow is the main

---

[1] Throughout the thesis we shall adopt the convention of denoting dimensional quantities with hat (e.g. $\hat{\rho}_H$) and dimensionless quantities without.

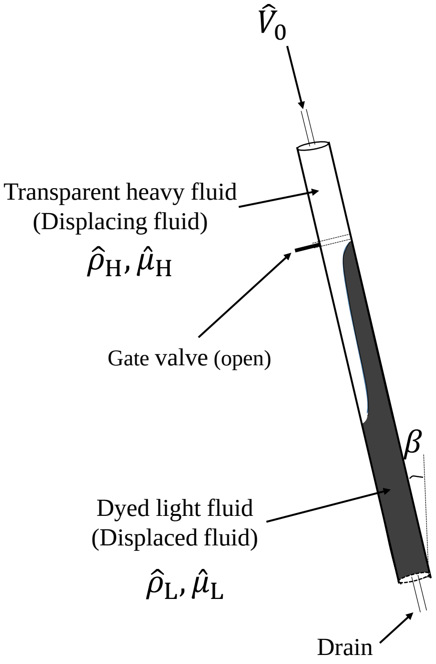

FIGURE I – Schematic view of the problem geometry. A dyed light fluid is displaced by a transparent heavy fluid. The pipe has the transverse diameter $\hat{D}$. The direction of the mean imposed flow with velocity $\hat{V}_0$ is along the pipe axis. $\hat{\rho}$ and $\hat{\mu}$ show the density and viscosity of fluids, respectively.

challenge involved in the primary cementing process. Type of geometry (pipe, annulus, etc.), geometry inclination, gravitational acceleration, physical properties of fluids, and considering two fluids of the displacement are the parameters which can be gathered in the form of 10-12 dimensionless groups to describe the fluid behavior (12). Moreover, external forces that are used to maximize the efficiency of the displacement flow and rheological properties of fluids (13; 14) are so wide and complex that it would be elusive to provide a comprehensive study of the displacement flow. Therefore, it would be necessary to simplify these complex phenomena to more clearly understand the displacement flow.

To date, many investigations have been done to understand the different features of displacement flows. Exchange flows and miscible displacement flows of Newtonian fluids in different geometries with different inclinations have been investigated in details. However, investigation of non-Newtonian displacement flows has been less developed due to the complex rheological behaviour of non-Newtonian fluids. Furthermore, there are only a few investigations in the literature which can be directly relevant to displacement flows with moving geometries. Therefore, our aim is to investigate how the mean imposed flow velocity, the Atwood number, and adding external force (e.g. geometry motion) affect the displacement flow efficiency. In addition, we study the effects of the yield stress value on the formation of new regimes.

I.II Fundamental interests and applications

As we mentioned earlier, the displacement flow of one fluid by another one (with different properties in a confined flow geometry) is one of the widespread phenomena, known in a diverse range of physical and engineering applications. The density difference and the rheology of fluids are two main parameters in all industrial displacement flows. Many investigations have reported experimentally and computationally the effects of the density difference on displacement flows in various geometries including near horizontal geometry (15; 16; 17), inclined geometry (18; 19; 20), vertical geometry (21) and non-uniform geometry (22; 23), but in this work we focus specifically on strictly vertical or moving geometries. In addition, displacement flows of non-Newtonian fluids have also been studied experimentally and numerically (1; 24; 25; 26; 27; 28; 29; 30; 31; 32; 33). The motivation of our work stems from different operations presented in the oil and gas industries (e.g. the primary cementing process) which often involves the displacement of one fluid by another one in a pipe, annulus or duct-like with large aspect ratios. There are two types of displacement flows: laminar and turbulent displacement regimes. The latter is typically more effective, but it is not always possible owing to process constraints. Therefore, our flows are laminar.

On the one hand, we know that different types of displacement flows and various flow regimes can occur depending on the contribution of different parameters and balances between participating forces (buoyancy, inertial and viscous, etc.). Therefore, many aspects of displacement flows, e.g. the fluid properties are really hard to predict. On the other hand, failure to achieve an effective displacement flow leads to contamination of fluids and increases the environmental pollution in primary cementing applications. In addition, the productivity decreases and the related costs strongly increase. Therefore, a better understanding of these flows is a strong industrial motivation. The application of this knowledge to improve the process design leads to the reduction of the environmental impacts and the related costs and increasing the productivity.

I.III Outline

The outline of this thesis is as follows: In the introduction, we study the industrial background and the related fundamental investigations and finally, the conclusions and research objectives are presented. Chapter 1 is devoted to the investigation of buoyant miscible displacement flows in a vertical pipe. Chapter 2 looks into displacement flows of two miscible, Newtonian fluids in a long, moving pipe while comparing the results with the corresponding displacement flows in a stationary vertical pipe. In Chapter 3, we observe the effect of increasing the yield stress of the displaced fluid on displacement flow behaviours. The thesis is concluded in general conclusions and future perspectives by highlighting the novel contributions of the research, some concluding, and future perspectives.

II Background

In 2013, a study was performed by Energy Information Administration (EIA) that was published in the International Energy Outlook 2013 (IEO2013) indicating a significant growth of world energy consumption by 56% between 2010 and 2040 from 553 to 865 quadrillion [2] kilojoules (kJ). Most of this demand for energy will come from non-OECD countries (non-Organization for Economic Cooperation and Development). While the energy consumption is ceaselessly increasing in the world (see Fig. II), the crude oil and the natural gas will remain the main sources of energy at least for the next few decades (34). Since 1850, the analysis indicates that the usage of fossil fuels (oil, gas, and coal) has increased globally and dominated the world energy consumption. Due to a sharp rise in fossil fuel combustion, CO_2 emissions (which cover 80% of greenhouse gas emissions) have increased rapidly. Subsequently, the most important environmental concern in these decades can be global warming (35).

The growth in worldwide energy consumption is forced primarily by China, India, Africa, the Middle East, and Southeast Asia. Investigations indicate that Canada consistently has been selected among the top 10 energy providers in the world (36). Canada energy productions are more than domestic consumption. Canada is rich in oil, petroleum, and natural gas. According to the U.S. EIA and Market Realist, Canada is the fifth-largest oil producer in the world, the third in natural gas production, and the third in crude oil reserves (see Fig. III). Therefore, it is vital to study the various aspects of improving oil and gas production to reduce the related costs.

One of the main processes that frequently occur in oil and gas industries is the displacement of one fluid by another one. This phenomenon is observed in many parts of oil and gas industries including constructing and completing of an oil well (e.g. primary cementing (2)), Floating Production Storage and Offloading (FPSO) (e.g. conditions like a start-up or shut-down of an operation), etc. In all the cases, geometries can be stationary or moving. The fluids in displacement flows in oil and gas industries often exhibit rheological properties and density difference. Geometries are generally pipe or annulus with large aspect ratios. In this chapter, we introduce the associated fundamental investigations that help us better understand the displacement flow problem.

This chapter is organized into three main sections. First, we describe the main related engineering background of our problem. The primary cementing process is our principal example. Second, we explain the associated fundamental investigations of our problem. Finally, we conclude this chapter with a brief summary of the main findings.

---

[2] In the USA, a quadrillion is a mere 10^{15}.

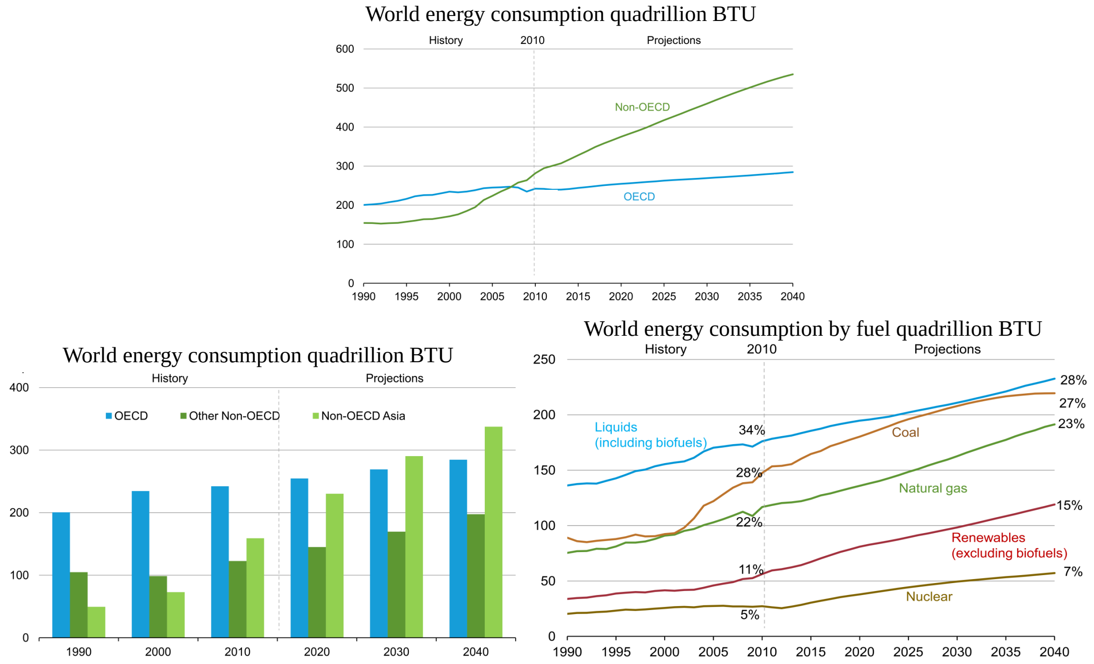

FIGURE II – World energy consumption (34).

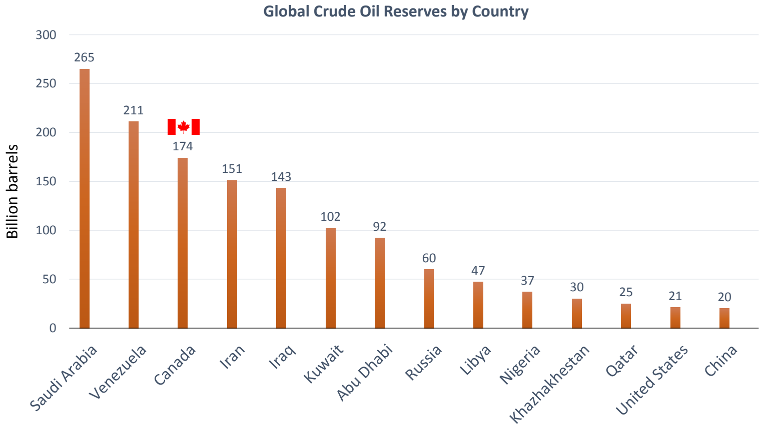

FIGURE III – Global reserved oil by country (36).

III Primary cementing process

In the oil and gas industries, one of the main operations performed at least once in every well is the primary cementing, which is a technique to place cement slurries in the annular gap between the casing and the well. The cement then becomes hard to hydraulically seal the oil and gas wells, which prevents the migration of formation fluids in the annular gap and increases the well productivity.

TABLE I – Rheological properties and flow parameters in the primary cementing. $\hat{\kappa}$, n, $\hat{\tau}_y$, $\hat{Q}$, $\hat{\rho}$ indicate consistency, power-law index, yield stress, flow rate, and density, respectively (2; 37).

$\hat{\kappa}$ (Pa.s^n)	n	$\hat{\tau}_y$ (Pa)	$\hat{Q}$ (1/min)	$\hat{\rho}$ (kg/m^3)
(3 – 3000)$\times 10^{-3}$	(1 – 10)$\times 10^{-1}$	0 – 20	(3 – 30)$\times 10^{2}$	(9 – 22)$\times 10^{2}$

III.I Physical description of the primary cementing

As we mentioned previously, the hydraulic seal of the annular gap is the primary cementing aim in all oil and gas wells. To achieve this objective, the drilling fluid must be fully removed from the annulus, and then the annular gap must be completely filled with the cement slurry. Usually, during the primary cementing operation, the fluids are pumped down the casing and then up the annulus.

A schematic geometry of the problem study is given in Fig. IV, which indicates a vertical casing filled with a series of fluids with different properties. Fig. IV indicates that the drilling fluid is being displaced by pumping spacer and cement slurry in the casing and then in the annulus. Ideally, when the cementing job is completed, there should be only a cement slurry in the annular gap to hydraulically seal the well.

Depending on the depth and location of the oil wells, the inclination angle of the pipe varies from horizontal to vertical. Due to large volumes of the fluids pumped, the fluids may be considered separated. A wide range of fluids is available for use in the primary cementing process. The displacing fluids (e.g. cement slurries) are typically 100-600 (kg/m^3) heavier than the displaced fluids (e.g. drilling mud). The properties of the spacer and cement slurries are designed in order to improve the displacement of the drilling mud in the annulus, all within the constraints of maintaining well security (1). Typical ranges of flow parameters and fluid properties are presented in Table I (2; 37).

Using Table I, typical ranges of dimensionless parameters can be provided for iso-viscous Newtonian displacement flows in the pipe as indicated in Table II (37). We can increase the Atwood number (At), up to 500×10^{-3}. The Reynolds number (Re), varies between 40 and 40000 which covers laminar and turbulent flows. The ratio of inertial forces to buoyant forces is represented by the Froude number ($0.1 < Fr < 50$). The pipe inclination (β), varies from nearly horizontal to strictly vertical. Moreover, there are other dimensionless groups involved such as the Péclet number (Pe), which is the ratio of advective to diffusive transport rate and rheological parameters e.g. the power-law index (n).

As mentioned previously, the complexity of the fluid displacement is the main challenge of understanding the cementing process. There are many parameters such as the fluid properties, the geometry, the inclination angle, gravitational acceleration, and the flow (38) that affect

Table II – Typical ranges of dimensionless parameters for displacement flow in a pipe. $\hat{\rho}_H$, $\hat{\rho}_L$, and $\hat{\rho}$ indicate the heavy, light, and mean densities of fluids, respectively. $\hat{V}_0$, $\hat{D}$ and $\hat{g}$ are the mean imposed flow velocity, pipe diameter, and gravitational acceleration. $\hat{\mu}$ and $\beta°$denote the viscosity and the pipe inclination angle (37).

$At = \frac{\hat{\rho}_H - \hat{\rho}_L}{\hat{\rho}_H + \hat{\rho}_L}$	$Re = \frac{\hat{\rho}\hat{V}_0\hat{D}}{\hat{\mu}}$	$Fr = \frac{\hat{V}_0}{\sqrt{At\hat{g}\hat{D}}}$	$\beta°$
$(1 - 500)\times10^{-3}$	$(4 - 4000)\times10^{1}$	$(1 - 500)\times10^{-1}$	$0 - 90$

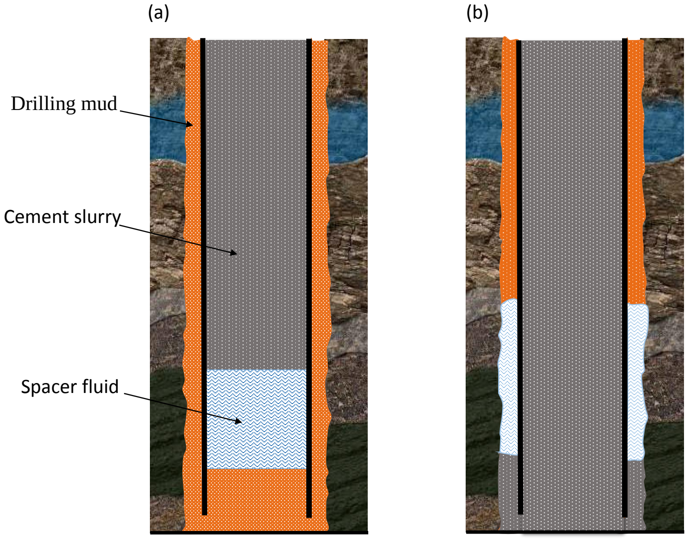

Figure IV – Schematic of the primary cementing operation indicating different stages of mud removal in which the drilling fluid in the system is being displaced by spacer and cement slurry fluids (a) in the casing (b) in the annulus.

the fluid behaviours. Using a dimensional analysis, we will have more than ten dimensionless groups (38). In addition, there are other aspects that reinforce the difficulty of the investigation of the primary cementing process. Therefore, a precise and comprehensive study of the displacement flow is really hard. The main aim of this work is to investigate the primary cementing process inside a pipe.

III.II Primary cementing challenges

Cementing is a complex and crucial step of the well construction in the oil and gas industries. However, failure of the cementing process leads to the occurrence of disasters such as the one observed at the Deepwater Horizon site in the Gulf of Mexico (39) (see Fig. V). The well-integrity failure and the hydrostatic control loss were two causes of the explosion in this site (39). Of course, there are a large number of problems associated with failures in the primary cementing process. Two main problems that stem from a clear fluid mechanics origin are:

Figure V – Deepwater Horizon accident site (39).

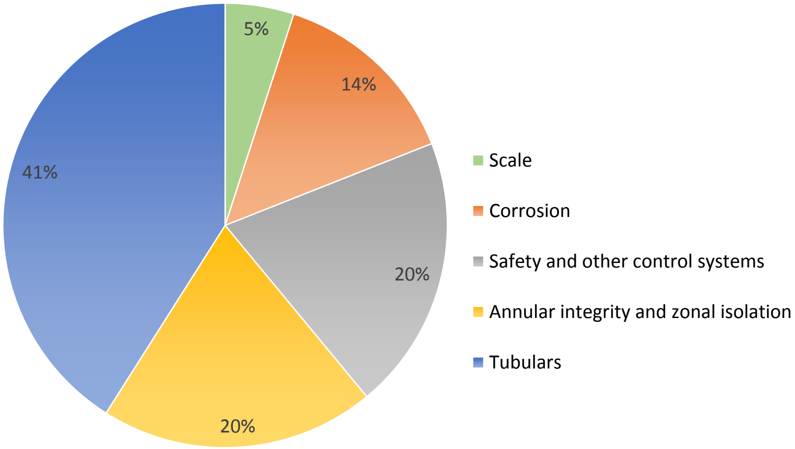

Figure VI – Failure distributions, affecting the performance and well integrity (39).

- The displacement is not efficient in the annulus and the mud is not completely removed.

- Contamination of the cement slurry by other fluids.

Both cases compromise the hydraulic seal of the well, which leads to a significant decrease in productivity, and a remarkable increase of the environmental and safety hazards. As we mentioned, there are many parameters that affect the primary cementing process. It is not clear how these parameters can impact the cementing process. Some examples of these parameters are the properties of cement and mud fluids, flow rate, and geometry of the well. Fig. VI indicates the failure distributions, affecting the performance and well integrity (39).

IV Associated fundamental investigations

Until now, many investigations have been devoted to different aspects of fluid displacement flows, which can help to understand the primary cementing process. Exchange flows and miscible displacement flows of Newtonian fluids have been studied deeply. In the case of exchange flows, the only driving force is the buoyancy, which is dissipated by either the viscous force or the inertial force. Debacq *et al.* (40; 41), Séon *et al.* (42; 43; 44; 45; 46), and Znaien *et al.* (47) have experimentally studied buoyant miscible exchange flows in a vertical or an inclined pipe. They have classified various flow regimes that may exist in the exchange flow configuration, e.g. inertial, viscous and diffusive. Two phenomena have been focused in their works: the interpenetrating front velocity ($\hat{V}_f$) and the macroscopic diffusion coefficient ($\hat{D}_M$). Debacq *et al.* (40; 41) showed that the latter characterizes the diffusive flow in which the extent of the axial diffusion is much larger than the molecular diffusivity. The former was found helpful to recognize whether the exchange flow is viscous or inertial. In addition, they found that $\hat{V}_f$ and $\hat{D}_M$ are functions of the density ratio, the fluid viscosity, and pipe diameters.

The miscible and immiscible displacement flows were investigated experimentally, theoretically and computationally in various geometries, including a strictly vertical geometry (21; 23), an inclined geometry (18; 19; 20; 48; 49), a near horizontal geometry (15; 16; 17), and a non-uniform geometry (22; 23). In comparison with an exchange flow, in the displacement flow, a mean imposed flow was imposed to the system. Thus, the focus of their studies was on quantifying the effects of $\hat{V}_0$ on the displacement flow behavior. In addition, we have found only very few studies in the open literature which can be directly relevant to displacement flows with moving geometries (50; 51; 52; 53; 54; 55; 56).

In comparison with the Newtonian displacement flows, the study of the non-Newtonian displacement flows has been less developed due to the complex rheological behaviour of the non-Newtonian fluids. To date, non-Newtonian displacement flows have been investigated experimentally and computationally in the Hele-Shaw cell (1; 33; 57), uniform geometries (25; 26; 30; 31; 32; 58; 59; 60) and complex geometries (27; 28; 61). In addition, several studies have been directed to understand the effects of non-Newtonian parameters such as the shear-thinning (62; 63), the shear-thickening (62), and the yield stress (12; 21; 58; 64; 65; 66; 67; 68) on the displacement flow. In the following subsections, we describe in details the studies related to the primary cementing.

IV.I Exchange flow

The exchange flow occurs in the absence of an imposed flow, e.g. when the end of the pipe is closed. Debacq *et al.* (40) studied the buoyant mixing of two miscible fluids in a long vertical tube in the absence of the mean imposed flow velocity. They found that depending on At, the diffusive behavior of the system is different. For a large At, they demonstrated that the effective diffusivity is 10^5 times higher than the molecular diffusion. At lower Atwood number, a sharp front limits the diffusive domain. The diffusive behavior disappears at Atwood numbers below the threshold. The series of experiments performed by Debacq *et al.* (41) indicated that the gravity-induced mixing in long vertical tubes is diffusive over a wide range of Atwood numbers, viscosities, and tube diameters.

Following a procedure similar to (41), Séon *et al.* (42) investigated experimentally the mixing of two fluids with different properties in a long tube that could be tilted at different angles, $0° < \theta < 90°$. An important finding was that by increasing θ, the macroscopic diffusion coefficient increases strongly. On the other hand, it was found that the dependency of the macroscopic diffusion coefficient on the Atwood number is not strong: for example, if the Atwood number increases from $At = 4 \times 10^{-3}$ to $At = 3.5 \times 10^{-2}$, the macroscopic diffusion coefficient only increases by 30%. In addition, Séon *et al.* (43) studied the buoyancy driven miscible front dynamics in tilted tubes as a function of the Atwood number, pipe inclination, and fluid viscosity. They found that by increasing θ and keeping all the other parameters fixed, three different flow regimes are observed. As θ increases the front velocity increases sharply (θ changes between 10° to 65°). It is due to the Boycott effect (the heavy fluid is locally separated from the light fluid and therefore sedimentation velocity increases (69)). Close to the front tip, the flow is turbulent and the transverse mixing is strong (regime 1). By increasing θ, $65° < \theta < 82°$, the front velocity reaches a plateau and remains at a maximum value (regime 2). In this regime, the segregation of the displacing and the displaced fluids is strong and the transverse mixing is not observed. In addition, the mean concentration profile is not diffusive. In the third regime, $\theta > 82°$, the fluid layers are separated into two counter currents, which are almost parallel. The control parameter is the viscosity and therefore this regime is called the viscous regime. In this regime, by increasing the pipe inclination, the front velocity decreases.

Owing to the interesting features of the plateau regime, Séon *et al.* (44) studied the buoyancy driven mixing in tilted tubes using Laser Induced Fluorescence (LIF) technique. They looked more precisely at the point-wise concentration field and studied the penetrating front inside the pipe. Fig. VII illustrates the images of the concentration field for the exchange flow obtained at different pipe inclinations using LIF. This figure proves the segregation induced by tilting the tube. The front velocity ($\hat{V}_f$), and the macroscopic diffusion coefficient ($\hat{D}_M$), in the strong mixing regime in a tilted tube were studied experimentally as a function of the Atwood number, the viscosity, and the tube diameter by Séon *et al.* (46). They found that the normalized front velocity, ($\hat{V}_f/\hat{V}_t$), and the normalized macroscopic diffusion coefficient, $\hat{D}_M/(\hat{V}_t\hat{D})$, are scaled respectively as $Re_t^{-3/4}$ and $Re_t^{-3/2}$ when $Re_t = \hat{V}_t\hat{D}/\hat{\nu} \leq 1000$ where $\hat{V}_t$ and $\hat{D}$ and $\hat{\nu}$ are the characteristic inertial velocity, the pipe diameter, and the kinematic viscosity, respectively. In addition, they showed that the front velocity increases linearly with $\tan\theta$ and $\hat{D}_M/\hat{V}_f^2$ and changes in the order of $(35 \pm 10)\hat{D}/\hat{V}_t$ in a wide range of control parameters. Moreover, they investigated the transient buoyancy-driven front dynamics in a long tube with small inclination

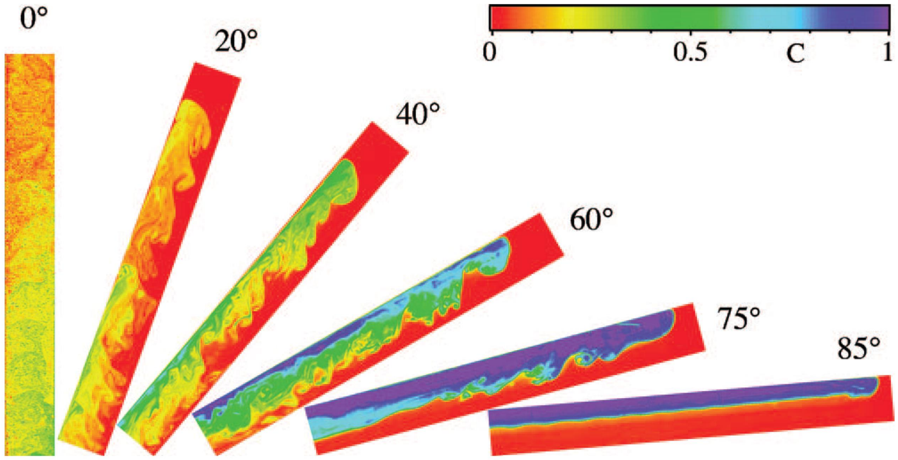

Figure VII – Images of the concentration field for the exchange flow along the pipe at different pipe inclinations using Laser Induced Fluorescence (LIF). The field of view that is covered by the camera is $\approx 20 \times 300$ (mm^2). The colour bar for the normalized concentration is indicated at the top right of the figure (44).

angles close to the horizontal (45). They considered for pipe inclinations greater than the critical values, the front velocity is controlled by the inertial force. But at lower inclinations, the inertial force initially controls the front velocity which is later controlled by viscous effects. The flow structure and the momentum transport for the buoyancy driven mixing flows were investigated by Znaien *et al.* (47). The velocity and the relative concentration profile were measured using Particle Image Velocimetry (PIV), and Laser Induced Fluorescence (LIF) methods as functions of θ and At. They indicated that by increasing At and decreasing θ, the regime changes from laminar to turbulent by passing from intermittent destabilizations. For a small At and a large pipe inclination ($\theta = 60^\circ$), a stable flow was observed. In contrast, for a large Atwood number and pipe inclination close to the vertical, a turbulent flow was observed.

More recently, Varges *et al.* (70) looked experimentally at exchange flows between yield stress materials and less dense Newtonian oils in a vertical tube. They considered three different flow regimes namely the stable (no flow), the quasi-stable and the unstable regimes. The latter is a wavy core-annular flow with the denser fluid in the core region. In the quasi-stable regime, due to thixotropic and elastic effects, a slow plug flow starts after a time delay. In the stable regime, the exchange speed is low. Fig. VIII indicates a mapping of flow regimes for the range of experimental parameters.

There are other papers that studied numerically the exchange flow in different geometries (71; 72). Hallez *et al.* (71) investigated the effects of the channel geometry on the exchange flow. They observed that there are significant differences between 2D and 3D geometries during a long-time evolution of the flow due to differences between the dynamics of the vorticity in

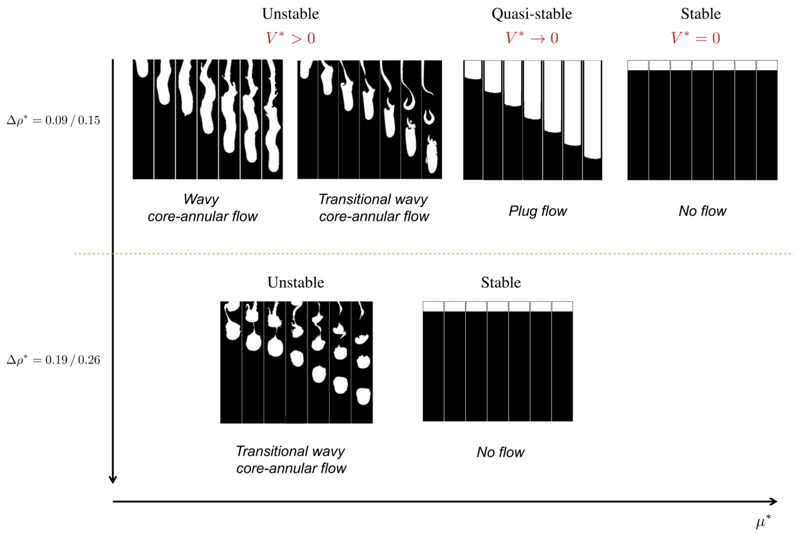

Figure VIII – Flow morphology as a function of dimensionless numbers and stability regimes. The dimensionless density difference, the dimensionless terminal velocity, the reduced gravity, and the viscosity ratio are introduced by $\Delta\rho^* = \Delta\hat{\rho}/\hat{\rho}_1$, $V^* = \hat{V}/\sqrt{\hat{g}'\hat{D}}$, $\hat{g}' \equiv \Delta\hat{\rho}/\hat{\rho}_1\hat{g}$ and μ^* where $\Delta\hat{\rho}$, $\hat{\rho}_1$, $\hat{\rho}_2$, $\hat{g}$, $\hat{V}$ and $\hat{D}$ are the density difference, the density of fluid 1, the density of fluid 2, the acceleration due to gravity, the terminal velocity and pipe diameter, respectively. (70).

those geometries. In the 2D geometry, vortices periodically cut the channel of pure fluid that feeds the penetrating front. In contrast, 3D geometries allow for the segregation effect to preserve a fluid channel near the front of each current. In their next study, Hallez *et al.* (72) studied numerically horizontal viscous gravity currents of immiscible fluids in the exchange flow configuration. They found a criterion that predicts which kind of viscous regime instantly succeeds the slumping phase. Their finding also showed the successive appearance of two different viscous regimes during the life of given flows.

IV.II Displacement flow in near horizontal to strictly vertical geometries

Well cementing process involves displacing of a cement slurry down a casing. Usually, drilling fluids are lighter than cement slurries, so the displacement flow mechanism is density unstable. Therefore, it is of interest to study density unstable displacement flows in pipes. It is worth again noting that by imposing a mean imposed flow velocity to the exchange flow, displacement flows in nearly-horizontal, inclined and strictly vertical ducts have been investigated profoundly. This problem is complex and therefore researchers have studied it under several and different conditions and assumptions: for example, the displacement flow can be miscible or immiscible with stable or unstable density differences and different viscosity ratios and other conditions. This problem originally investigated by Taylor (73). After, it was generalized by considering the Newtonian displacement flows (74; 75; 76; 77), Newtonian-non-Newtonian displacement flows (58; 78) and non-Newtonian displacement flows (25; 30; 79). In addition, Petitjeans and Maxworthy (80) experimentally investigated miscible displacement flows in capillary tubes at high Péclet number flows and low to moderate Reynolds numbers. They found a very good agreement with the numerical results (81). Scoffoni *et al.* (82) studied the effects of viscosity ratio and flow rate in vertical displacement flows. They determined a stable finger. In addition, they identified two other modes: axisymmetric mode and a corkscrew one. There are other investigations of displacement flows in vertical geometries which studied the effects of viscosity and density on instabilities (83; 84). These studies are more structured than flows observed in the primary cementing process. Therefore, investigation of the displacement flow found in the cementing process must be extended systematically.

Focusing initially on Newtonian displacement flows, the effects of a mean imposed flow on the stability of gravity currents in a pipe close to horizontal was investigated by Taghavi *et al.* (85). The buoyancy is the driving force in the gravity currents, but these flows may be limited by physical mechanisms such as inertial or viscosity depending on the different parameters, including geometry, type of fluids, and the mean imposed flow velocity (45). Taghavi *et al.* (85) found that the front velocity and physical mechanisms can be affected significantly in the presence of the mean imposed flow velocity. In addition, they identified three different flow regimes by increasing $\hat{V}_0$ from zero. In the first regime, when $\hat{V}_0 \rightarrow 0$, they considered the exchange flow dominated, in which the effect of the mean imposed flow on the dynamics of the exchange flow is negligible. In the second regime, there is a balance between dissipative forces and the pressure gradient, but the buoyancy driven flow is weaker than the mean imposed flow. In this regime, the relation between the front velocity and the mean imposed flow velocity is linear ($\hat{V}_f/\hat{V}_0 \approx 1.3$). An interesting behavior of this regime is that although the buoyancy force plays an important role to govern the dynamics of the flow, the slope $\hat{V}_f/\hat{V}_0$ does not change remarkably with the Atwood number. In the third regime, the mean imposed velocity value is large, $\hat{V}_0 > 150 - 200$ (mm/s), and a second linear regime is observed ($\hat{V}_f/\hat{V}_0 \approx 1$). In this regime, the effect of the buoyancy force is negligible in comparison with the mean imposed flow velocity. In addition, they studied the effect of the mean imposed flow velocity on the stability of the flow (see Fig. IX). They found that at small velocities, the Kelvin–Helmholtz instability is observed (Fig. IXa) and the instability develops the mixing at the interface between two fluids. Fig. IXb shows that by increasing the mean imposed flow velocity, a stable flow is observed. Therefore, there is no Kelvin–Helmholtz instability and no mixing at the interface between two fluids. Finally, in Fig. IXc by further increase of the mean imposed flow velocity, a third flow regime is considered. In this regime, the buoyancy force is negligible and the interface between two fluids is combined due to transverse mixing induced by the turbulent mean imposed flow. In this case, the displacement is complete. Therefore, the two fluids are separated by a mixing zone.

Taghavi *et al.* (86) studied in depth the physics of the transition between an exchange flow

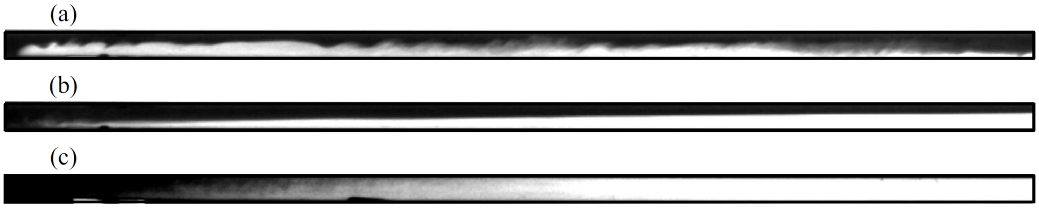

FIGURE IX – Snapshots of video images taken for different mean imposed flows are obtained at $\theta = 83°$, $\hat{\mu} = 10^{-3}$ (Pa.s), $At = 10^{-2}$ and different mean imposed flow velocities (a) $\hat{V}_0 = 8.6$ (mm/s) (b) $\hat{V}_0 = 71$ (mm/s) (c) $\hat{V}_0 = 343$ (mm/s) (85).

dominated regime and a laminarised viscous displacement regime. By increasing the mean imposed flow velocity from zero, the regime is changed from an exchange flow dominated regime to another regime in which there is a linear relationship between $\hat{V}_0$ and $\hat{V}_f$. An interesting phenomenon was uncovered during the transition. This phenomenon can be explained as a static layer of the displaced fluid stayed at the top of the pipe during the entire duration of displacement flows. In other words, this study indicates a transition between back-flow and instantaneous displacement flows. The instantaneous displacement means that the displaced fluid does not go upstream of the gate valve. By analysing the results, Taghavi *et al.* (86) found that stationary interfaces can be observed for each pipe inclination only at a critical balance in equation 1,

$$\hat{V}_\nu \cos\beta \approx 58.16\hat{V}_0, \tag{1}$$

where $\hat{V}_\nu$ is the viscous velocity and is defined by $\hat{V}_\nu = At\hat{g}\hat{D}^2/\hat{\nu}$.

Later, Taghavi *et al.* (16) confirmed the previous results obtained in Taghavi *et al.* (85; 86) with a wider range of experimental parameters. In addition, the dynamics of all regimes were investigated in more details. Finally, they focused on the issue of finding a way to model inertial effects. After modeling the problem, there was a comparable agreement between the front velocity calculated by the lubrication model and the experimental front velocity.

Next, Redapangu *et al.* (87) investigated the pressure-driven displacement flow of two immiscible fluids in an inclined channel in the presence of viscosity and density gradients. They used a multiphase lattice Boltzmann approach. Their results showed that increasing the viscosity ratio leads to a decrease of the displacement rate, and has a non-monotonic impact on the velocity of the leading front. However, they observed that by increasing the viscosity ratio, the velocity of the trailing edge decreases. In addition, they found that the displacement rate of the thin-layers increases with increasing the inclination angle which is due to the increase of the interfacial instabilities when the inclination angle increases. This leads to a better cleaning of the channel. This also includes the finding of (16).

The main focus of Taghavi *et al.* (31; 88) was on the investigation of the buoyant miscible displacement flow of two fluids with different viscosities in near-horizontal ducts. The viscosity ratio is introduced by $m = \frac{\hat{\mu}_1}{\hat{\mu}_2}$ in which $\hat{\mu}_1$ and $\hat{\mu}_2$ are the viscosity of heavy and light fluids, respectively. It is expected that when $m < 1$ the displacement is more efficient and for $m > 1$ the efficiency of the displacement flow decreases. They showed that as m decreases ($m < 1$), the ratio of $\frac{\hat{V}_f}{\hat{V}_0}$ decreases and the efficiency of the displacement flow increases. In addition, the variation of $\hat{V}_f$ with $\hat{V}_0$ is almost linear. However, for $m > 1$, as m increases, the value of the front velocity does not change significantly. In other words, by increasing m the efficiency of the displacement flow remains approximately unchanged.

By increasing the pipe inclination angle from the near horizontal position, Alba *et al.* (18; 19; 78; 89; 90) investigated miscible displacement flows of Newtonian and non-Newtonian fluids in a long tube. They found that there is a non-monotonic relation of the displacement flow efficiency with the Atwood number when there is a transition from positive (density unstable) to negative (density stable) Atwood numbers. Highly efficient displacement flows can be observed at the density stable configuration. In this case, the interface between the displaced and the displacing fluids moves steadily with the same velocity of the mean imposed flow. In addition, the stream-wise distance between the leading and trailing fronts, introduced by the stretch length and presented by L, was found and measured in inclined geometries. They found a correlation between the stretch length and the other experimental parameters (see equation 2):

$$L - \tan\beta = -3680/\chi, \tag{2}$$

where χ is the ratio of the buoyancy force to the viscous stress and β is the pipe angle from the vertical position (89).

For the density unstable configuration, various flow regimes were observed by Alba *et al.* (18), including the well mixed fully diffusive, the instantaneous, the inertial and the viscous regimes, all with the variation of the stability degree. They found that each regime can be explained in the dimensionless planes of Fr and $Re\cos\beta/Fr$. In addition, they considered that when the regime is viscous, the lubrication model is an effective method to predict the front velocity when there is no bulk diffusion. On the other hands, in the fully diffusive regime, the displacement efficiency increases strongly and $\hat{V}_f \approx \hat{V}_0$.

As we discussed before, the investigations of non-Newtonian displacement flows have been less developed due to the complex rheological behavior of non-Newtonian fluids. Taghavi *et al.* (31) studied the buoyant miscible displacement flows of yield stress fluids in long near-horizontal pipe. They obtained two different flow regimes: a central-type and a slump-type displacement flow regimes. In the latter case, the displacing fluid moves along the bottom of the pipe. They observed two propagating displacement fronts: the fast front which moves near the bottom of the pipe and the slow front which displaces a thicker layer of the yield stress fluid. They found that the transition between these two regimes is a function of the ratio of the Reynolds number to the densimetric Froude number and is independent of other dimensionless numbers. In addition, Alba *et al.* (90) investigated the effect of the yield stress on the displacement flow for a wide range of pipe inclinations from 0 to 85°. They found that the slump and the center-type displacement flows can be obtained over a wide range of the pipe inclinations. An interesting pattern here is that these flow regimes occur approximately at the same ratio of Re/Fr as in the near-horizontal case.

It is worth noting that in Chapter 3, the displacement flow of yield stress fluids in a vertical pipe is investigated experimentally. Particularly, we are interested in studying the displacement of a yield stress fluid by a less viscous Newtonian fluid. There are studies in the literature which can be directly related to this work. For example, Cole *et al.* (59) investigated the cleaning of a yield stress fluid from surfaces at two length scales: the laboratory scale and the pilot scale. They considered that the cleaning time is affected by the temperature and the velocity of the displacing fluid. In addition, they showed that the pipe length does not seem to have a significant effect on the cleaning time. Dimakopoulos and Tsamopoulos (26) investigated the displacement flow of a yield stress fluid by a Newtonian fluid in a straight tube and suddenly constricted tube. They found that unyielded regions arise in front of the displacing fluid in the straight tube. In addition, unyielded regions are considered near the recirculation corners for the constricted tube. More recently, Moisés *et al.* (58) experimentally investigated the isodense displacement of yield stress fluids by a Newtonian fluid in a horizontal pipe. They considered three different flow regimes named as the smooth, the wavy and the corrugated. The variation of the residual layer level along the pipe is a key factor to make the difference between various regimes. Based on dimensionless numbers, they found that the transition between these regimes is a function of the Reynolds number.

The formation of the stationary residual layer of the displaced fluid on the wall is a serious aspect related to yield stress displacement flows. The difficulty in removing these layers, especially from the interior sections of flow geometries needs more attention. Allouche *et al.* (25) showed that the residual layer usually remains on the wall when the yield stress of the displaced fluid is larger than that of the displacing fluid. They found that due to the yield stress effect, the residual wall layer for viscoplastic fluids can be completely stationary. Poslinski *et al.* (91) experimentally investigated the displacement of a viscoplastic fluid by air in a tube. They found that the thickness of the residual layers is much larger compared to Newtonian fluids. Recently, Zare *et al.* (21; 92) studied miscible displacement flows when a Newtonian fluid displaces a Bingham fluid for both the density stable and the density unstable configurations in a plane channel. They measured the residual wall layer thickness (h), close to the end of their channel. By comparing the value of h with the maximal static wall layer thickness (h_{max}), they found that the residual layer is classified into moving or static regimes. It should be mentioned that they calculated h_{max} using the following equations:

$$4\chi^* y_{i,min}^4 - (2\chi^* - 4B_N)y_{i,min}^3 - 3 = 0, \tag{3}$$

$$h_{max} = 1/2 - y_{i,min}, \tag{4}$$

where $\chi^* = 2Re/Fr$ is the buoyancy parameter and B_N is the Newtonian Bingham number. It is worth mentioning that the flow in $(-y_i, y_i)$ is a Newtonian Poiseuille flow. If $h_{max} = 0$, the wall layer is moving. If $h_{max} > 0$, there are two different situations: $h < h_{max}$ means that the wall layers are static; otherwise the wall layers are moving. In the case of the density unstable flow (21), the displaced fluid was heavier than the displacing fluid and the flow direction was upwards. They showed that in the density unstable situation the static residual wall layers can be observed for yield stresses below the minimum value for the density stable regime. In addition, by comparing the results with the density stable flow, they considered that the layers may be thicker in the density unstable situation.

There are few published investigations related to displacement flows in moving geometry. Savery *et al.* (93) studied multiple aspects of the mud displacement during the cementing process using computational fluid dynamics (CFD). Two and three dimensional computational approaches were used to investigate how the casing motion can affect the displacement flows in oil well completion applications. They discovered that the rotation of the inner casing during the cementing job increases the efficiency of the primary cementing and decreases the possibility of supplementary works such as liner top and zonal isolation squeezes (94).

Carrasco-Tejaand and Frigaard (52; 53) studied analytically the displacement flows of Newtonian and non-Newtonian fluids in a horizontal, eccentric annulus with a moving inner cylinder. The focus of Carrasco-Tejaand and Frigaard (52) was on the displacement flows between two Newtonian fluids with different densities and viscosities. Similar to static walls (95; 96), they found analytically that the steady traveling wave displacement can be observed in small buoyancy numbers. They found that the inner cylinder rotation decreases the expansion of the interface between fluids in the axial direction. On the other side, using computational simulations, they observed that at large buoyancy numbers and when the axial extension is enough large, there is a local buoyancy-driving fingering instability. It is worth noting that the local fingering is controlled by the rotation of the casing and the annular eccentricity. The local fingering can be replaced by the steady extension of the diffusive interfacial region that propagates gradually due to dispersion. In the case of non-Newtonian fluid displacements, Carrasco-Tejaand and Frigaard (53) derived a lubrication-style model and found that the leading order interface is symmetric. They indicated that the inner cylinder rotation changes the length of the leading-order interface only for non-Newtonian fluids with shear-thinning properties. Recently, Bu *et al.* (97) studied the effect of casing rotation to improve the cementing quality. In the case of non-rotation, they found that the displacement flow efficiency increases as the density difference increases. In addition, they considered that increasing the casing eccentricity results in the decreasing of the displacement flow efficiency. Under the same conditions, they showed that the casing rotation can improve the displacement flow efficiency. Most recently, Lyu *et al.* (56) studied experimentally the effects of a pipe axial rotation on the stratified displacement flow in the presence of two Newtonian fluids. They found that the transverse mixing is induced by increasing the pipe rotation speed. Consequently, complete removal of the displaced fluid occurs at a critical transition number introduced by $Ro \approx 5Fr(1-Fr)^{-1}$ where Ro is the Rossby number, indicating the ratio of inertial to Coriolis forces.

In the other investigations, the authors reported the effect of pulsating flows on the displacement flow efficiency. Oscillating flows of yield stress fluids have been investigated mathematically and analytically (98; 99; 100). For pulsating displacement flow rates, Wielage *et al.* (30) found that the layer thickness is significantly decreased by the pulsation.

V Conclusions and research objectives

Through a literature review, we have seen that the buoyant miscible displacement flow problem is attractive from both fundamental and industrial points of views. In this chapter, a summary of the most relevant works is wrapped up and the research objectives are outlined.

Gravity currents and exchange flows are two areas which have been investigated analytically, numerically and experimentally. These flows have been studied deeply for the Newtonian fluids for different inclination angles and different Atwood numbers. Of course, they are still open subjects to study, especially for non-Newtonian fluids.

Adding a mean imposed flow to the exchange flow leads to the appearance of another area introduced by the displacement flow. Displacement flows have been investigated as a function of different parameters in details in nearly-horizontal, inclined, and strictly vertical geometries. Combination of these parameters, i.e. inclination angles (β), the density difference (At) and the mean imposed flow velocity ($\hat{V}_0$) helps to better understand the behavior of these flows, uncovering new phenomena and presenting new flow regime maps. In this thesis, producing reliable data to understand the flow characteristics is of major importance. Another contribution of this research is studying the effect of moving geometry and rheological measurements on the displacement flow behavior.

By increasing the mean imposed flow velocity, the turbulent flow is observed. This flow is a limit in our research. In this condition, the mixing is strongly efficient and the dispersion of fluids occurs along the pipe. Therefore, there is not much potential to improve the efficiency of the displacement flow. In addition, the Taylor dispersion theory well explains this turbulent regime (101). Therefore, there is no strong motivation to investigate this regime. Consequently, in this work, we prefer to investigate the displacement with a laminar imposed flow.

The effects of the viscosity ratio in buoyant miscible displacement flows have been investigated in many previous studies. Of course, due to the importance of the related applications, there are still motivations to study this field more deeply. Industrial buoyant miscible displacement flows often include the viscosity ratio. Therefore, studying the effects of increasing or decreasing the fluid viscosities is extremely important. Moreover, considering industrial applications of the displacement flow, the investigation of yield stress flows needs even more attention. Here, when the displaced fluid has a yield stress, it is of more interest due to the appearance of residual wall layers. The appearance of these layers of the displaced fluid is common for yield stress displacement flows. The static or moving form of residual wall layers and their thicknesses should be studied in more depth.

The technical and scientific goals of the current research are to provide reliable knowledge to be employed in the primary cementing process by investigating buoyant miscible displacement flows of Newtonian and non-Newtonian fluids in a pipe. The physical and parametric complexity of the fluid displacement are the main challenges of understanding the cementing process. A key objective is to understand the effect of each parameter individually on the displacement flow and its efficiency. This starts by investigating the effects of the mean imposed flow velocity, the density difference, rheological parameters, and the flow geometry motion.

The literature review shows that despite some developments in understanding basic mechanisms in displacement flows, our understanding of the different effects of controlling parameters is not comprehensive. This requires an in-depth analysis of the effects of various flow parameters, such as the mean imposed flow velocity, the rheological parameters, the geometry motion, etc., on displacement flows.

In this thesis, we attempt to advance our knowledge of the displacement flow in the stationary and the moving geometries. To do this, scaled laboratory displacement flow experiments are conducted in a long vertical pipe. In addition, to produce desirable motion, our setup is placed on a hexapod robot, which has six degrees of freedom. We consider a realistic range of flow parameters and fluid properties. The displacement flow efficiency is investigated by determining the effect of each parameter. In addition, we provide flow regime maps to identify the principal flow types. We have considered the following parts:

- First, we investigate the buoyant miscible displacement flow of Newtonian fluids by changing the main parameters at a wide range of fluid properties to consider the effect of each parameter on the behavior of flows and determine the main flow regimes. Then, we provide the most relevant flow regime maps.

• Second, the effect of a flow geometry motion on the displacement flow of Newtonian fluids is studied by imposing an inverted pendulum motion. Compared to the stationary case, we investigate the displacement flow mechanisms of the moving geometry and study the effect of each parameter on the displacement flow. Then, we provide a flow regime map to identify the main flow features.

• Finally, experiments are performed using yield stress fluids as the displaced fluid in a stationary pipe. The behavior of fluids is explained by investigating the effects of the rheological properties on displacement flows. The fluid behaviours are explained simply by introducing the yield stress ($\hat{\tau}_y$), the power-law index (n), and the consistency ($\hat{\kappa}$).

The aim of this research is to deliver a significant amount of reliable experimental data to address the knowledge gap in the literature about buoyant miscible displacement flows, by providing leading order predictions of the flow behaviours using the dimensionless numbers that govern the flow.

Chapitre 1

Buoyant miscible displacement flows in vertical pipe

Résumé

Le écoulement de déplacement de deux fluides Newtoniens miscibles est étudié expérimentalement dans un tuyau vertical de grand allongement ($\delta^{-1} \approx 210$). Les fluides ont une faible différence de densité et ils ont la même viscosité. Le fluide de déplacement lourd est initialement placé au dessus du fluide de déplacement léger. Le écoulement de déplacement est dirigé vers le bas. Les expériences couvrent un large éventail de deux paramètres sans dimension décrivant en grande partie le écoulement : le nombre de Reynolds modifié ($0 \leq Re_t \leq 800$) et le nombre densimétrique de Froude ($0 \leq Fr \leq 24$). Nous rapportons l'effet stabilisant du écoulement imposé et découvrons l'existence de deux régimes d'écoulement principaux à long moment : un écoulement de déplacement stable et un écoulement de déplacement instable. La transition entre les deux régimes se produit à un nombre critique de Reynolds modifié $Re_t|_{Critical}$, en fonction de Fr. Nous étudions en détail le régime d'écoulement stable. Premièrement, un modèle de lubrification, associé à une simple formulation d'accélération initiale, permet de prédire de manière raisonnable la vitesse frontale de déplacement pénétrante dépendante du temps, deuxièmement, nous trouvons deux sous-régimes pour les déplacements stables, à savoir les écoulement à reécoulement prolongé et les écoulement à reécoulement non prolongé. La transition entre les deux sous régimes est un état d'écoulement d'interface stationnaire marginal, qui est également bien prédit par le modèle de lubrification. Le régime instable est associé aux instabilités et aux caractéristiques diffusives du écoulement. En outre, des schémas particuliers tels que le phénomène de détachement frontal apparaissent dans le régime d'écoulement instable, pour lequel nous quantifions les régions d'existence par rapport aux groupes sans dimension.

Abstract

The displacement flow of two miscible Newtonian fluids is investigated experimentally in a vertical pipe of long aspect ratio ($\delta^{-1} \approx 210$). The fluids have a small density difference and they have the same viscosity. The heavy displacing fluid is initially placed above the light displaced fluid. The displacement flow is downwards. The experiments cover a wide range of the two dimensionless parameters that largely describe the flow: the modified Reynolds number ($0 \leq Re_t \leq 800$) and the densimetric Froude number ($0 \leq Fr \leq 24$). We report on the stabilizing effect of the imposed flow and uncover the existence of two main flow regimes at long times: a stable displacement flow and an unstable displacement flow. The transition between the two regimes occurs at a critical modified Reynolds number $Re_t|_{Critical}$, as a function of Fr. We study in depth the stable flow regime: first, a lubrication model combined with a simple initial acceleration formulation delivers a reasonable prediction to the time-dependent penetrating displacing front velocity. Second, we find two sub-regimes for stable displacements, namely sustained back-flows and no-sustained back-flows. The transition between the two sub-regimes is a marginal stationary interface flow state, which is also well predicted by the lubrication model. The unstable regime is associated with instabilities and diffusive features of the flow. In addition, particular patterns such as a front detachment phenomenon appear in the unstable flow regime, for which we quantify the regions of existence versus the dimensionless groups.

1.1 Introduction

Displacement flows frequently occur in nature (e.g. in lung airways (102)) as well as in industry, e.g. the petroleum industry (2) (e.g. in the processes such as *primary cementing* and *top kill*), manufacturing (103) and food processing (5). In this work, we experimentally study high-Péclet-number miscible displacement flows of Newtonian fluids in a long, vertical pipe. Our scenario considers two fluids that have a small density difference (in the Boussinesq limit) and nearly identical viscosities. Buoyancy is a significant driving force but there is also a mean imposed flow in the downwards direction. The flow configuration is mechanically unstable and the flow is extremely susceptible to instabilities. Therefore, from the fluid mechanic's point of view, a fundamental question is where stable displacement flows may be found. This is the focus of the current study.

Our work extends from the exchange flow limit (i.e. buoyancy-driven flows with a zero mean imposed flow velocity). Miscible exchange flows in vertical pipe have been studied by Debacq *et al.* (40; 41), who experimentally observed stable and unstable counterflows. While the former was found to be associated with completely segregated streams of interpenetrating light/heavy fluids, the latter was related to inertial and diffusive flows with coarse (convective diffusive) or fine (turbulent diffusive) mixing at small and large buoyancy forces, respectively. Debacq *et al.* (41) characterized the velocity of the interpenetrating exchange flow fronts ($\hat{V}_f$ [1]) for which the relevant velocity scales were the characteristic viscous and inertial velocities ($\hat{V}_\nu$ & $\hat{V}_t$) for stable and unstable flow regimes, respectively. These are defined as $\hat{V}_\nu = At\hat{g}\hat{D}^2/\hat{\nu}$ and $\hat{V}_t = \sqrt{At\hat{g}\hat{D}}$, where $\hat{\nu}$ is the kinematic viscosity, At is Atwood number (i.e. the relevant dimensionless density ratio), $\hat{g}$ is gravitational acceleration, and $\hat{D}$ is the pipe diameter. They also showed that the transition between stable and unstable exchange flows occurs at a critical modified Reynolds number $Re_t|_{Critical} \approx \sqrt{48 \times 130} \approx 79$, where $Re_t = \hat{V}_\nu/\hat{V}_t$. In a series of detailed studies, Seon *et al.* (42; 43; 44; 45; 46) extended the work of Debacq *et al.* (40; 41) to various pipe inclinations from horizontal ($\beta \approx 90°$) to vertical ($\beta \approx 0°$). Among their interesting findings, they discovered that the boundary between stable and unstable flows was also a function of pipe inclination angle, β, which they successfully incorporated into the same dimensionless group proposed by Debacq *et al.* (41) to furnish $Re_t \cos\beta|_{Critical} \approx 50$ for highly inclined pipes.

It is appropriate to also mention a few relevant computational works. Hallez *et al.* found stable and unstable exchange flows while quantifying the effects of the flow geometry in channels (71; 72) and pipes (71; 104). Many flow features were studied in details. For example, they found that vortices in 2D geometries are strongly present, coherent and long persistent, leading to a periodic *cut* of the channels of pure fluid feeding the front; see (71). Sahu *et al.* (105) also computationally studied displacement flows of miscible fluids in 2D channels. They explored stable and unstable displacement flow regimes at various inclinations.

Miscible displacement flows in inclined and highly inclined pipes/channels have been studied extensively. Taghavi *et al.* (15; 16; 85; 86) studied stable and unstable displacement flows at nearly-horizontal inclinations in both 2D channels and pipes. They developed a thin-film/lubrication type model to predict front velocities for stable displacement flow regimes; see (15). The departure from the exchange flow configuration was studied in (85), where they found three flow stages as the mean imposed flow velocity ($\hat{V}_0$) was added to the exchange flow. The flow behaviours at small $\hat{V}_0$ were similar to their exchange flow counterparts at $\hat{V}_0 = 0$ (e.g. in (43)), where a *sustained-back-flow* against the direction of the mean imposed flow was observed. Increasing the mean imposed flow velocity resulted in the penetrating front velocity of displacing fluid $\hat{V}_f$ to vary linearly with $\hat{V}_0$. Another important effect of the mean imposed flow was that the amount of back-flow was progressively reduced. In addition, the mean imposed flow counter-intuitively stabilized the displacement flow. They suggested that the latter was due to the effect of increasing the local gradient Richardson number, Ri. For higher imposed flows, a turbulent flow regime was found, where $\hat{V}_f \approx \hat{V}_0$ (85). For a highly inclined geometry, Taghavi *et al.* (86) quantified the transition between the flows with a sustained back-flow and the ones without (*no-sustained-back-flow*) through a critical ratio:

---

[1] In this paper we adopt the convention of denoting dimensional quantities with the ˆ symbol and dimensionless quantities without.

$Re_t \cos\beta/Fr$, where Fr is the densimetric Froude number. This critical parameter evaluates the ratio of buoyancy stresses in the axial direction and viscous stresses induced by the mean imposed flow velocity. A complete picture of displacement flows in near-horizontal channels and pipes was presented in Taghavi *et al.* (16). This approach was extended by Alba *et al.* (18) to provide a flow regime classification over a wider range of inclination angles. They also quantified stable and unstable flow regimes (including inertial and diffusive flows) for displacement flows in inclined pipes.

Compared to the other studies in the field, buoyancy was significant in the exchange flow and displacement flow studies mentioned above. Due to the presence of large viscosity, stable density differences or slow flows, these other studies are structured flows in usually vertical geometries. Chen and Meiburg (81) and Petitjeans and Maxworthy (80) studied miscible displacement flows at high Péclet number computationally and experimentally, respectively. In a combined theoretical-experimental study, Lajeunesse *et al.* (106; 107; 108) studied miscible displacement flows in a vertical Hele-Shaw cell, and they looked into quantifying flow stability as a function of viscosity ratio and imposed flow rate. Interfacial instabilities in displacement flows have been studied, e.g. in Balasubramaniam *et al.* (84) and Scoffioni *et al.* (82) at various viscosity ratios. Other studies, e.g. Kuang *et al.* (83), have investigated the velocity distribution and finger tip shape in displacement flows. Jiao and Maxworthy (109) have investigated fingering patterns for displacement flows with density and viscosity contrasts. Hele-Shaw exchange flows have been also studied experimentally and computationally (110; 111; 112; 113).

The novelty of our current study can be summarized as follows. First, we show for the first time that stable displacement flows may exist in a highly mechanically-unstable configuration, i.e. a vertical pipe, despite hydrodynamic effects. We also quantify some of the leading order behaviours of stable and unstable displacement flows and delineate the boundary of their transition. Second, although displacement flows in inclined geometries have been studied in depth, our work fills an evident gap in the literature through studying these flows in a strictly vertical pipe. It should be highlighted that the results of these previous studies, e.g. (16; 18), cannot be directly interpreted to describe displacement flows in a vertical geometry configuration. Dimensionless groups in the previous works include $Re_t \cos\beta/Fr$, which for example implies that a flow with a certain Re_t in a pipe inclined at $\beta = 30^\circ$ is identical to another flow with $Re_t/2$ in a vertical pipe. However, these flows cannot be the same as at least some degree of symmetry is naturally present in the vertical case and it is quickly broken in inclined geometries. Thus, although the leading order predictions of the previous studies are acceptable for displacement flows at inclinations, these are inevitably achieved at the expense of hiding the effect of inclination as a separate parameter. In the current work, the pipe inclination is fixed to vertical; thus, our regime classification does not involve any unnecessary simplifications and reduction of the dimensionless groups. Third, our study delivers a wide range of valuable experimental results. For example, the range of the Atwood number studied here covers almost

TABLE 1.1 – Range of the dimensionless parameters used in our experiments. The dimensional parameters used to define the dimensionless parameters are introduced in Table 1.2. Note that in our experiments the minimum values of Re, Fr and Pe based on the minimum non-zero imposed flow velocity ($\hat{V}_0 \neq 0$) were 7, 0.15 and 3283, respectively.

Parameter	**Name**	**Definition**	**Range or value**
At	Atwood number	$\frac{\hat{\rho}_H - \hat{\rho}_L}{\hat{\rho}_H + \hat{\rho}_L}$	$(1 - 700) \times 10^{-4}$
Re	Reynolds number	$\frac{\hat{V}_0 \hat{D}}{\hat{\nu}}$	$0 - 1940$
Fr	Densimetric Froude number	$\frac{\hat{V}_0}{\sqrt{At \hat{g} \hat{D}}}$	$0 - 24$
Pe	Péclet number	$\frac{\hat{V}_0 \hat{D}}{\hat{D}_m}$	$0 - 970 \times 10^3$
δ^{-1}	Pipe aspect ratio	$\frac{\hat{L}}{\hat{D}}$	210

three orders of magnitude. Finally, further understanding of our stable displacement flows is gained through the development of a lubrication model. The model delivers predictions to a marginal state called the stationary interface flow to characterize the transition between sustained-back-flows and no-sustained-back-flows in a vertical pipe. In addition, the outcome of the lubrication model predictions for front velocities is combined with an initial acceleration formulation to furnish time-dependent displacing fluid front velocities.

1.1.1 Problem setting

The situation that we consider in this paper is that a heavy fluid (fluid H) displaces a light fluid (fluid L) along a long, vertical pipe. The pipe has a diameter $\hat{D}$ and the mean imposed displacement velocity is $\hat{V}_0$, in the downward direction. The fluids have the same viscosity $\hat{\mu}$, they are miscible and they have slightly different densities. Let us denote the density of the heavy displacing fluid by $\hat{\rho}_H$ and that of the light displaced fluid by $\hat{\rho}_L$. In general, we study laminar imposed flows. The length of the pipe satisfies $\delta^{-1} = \frac{\hat{L}}{\hat{D}} \gg 1$. The initial interface is horizontal, which is transverse to the pipe axis, and it is located away from both ends of the pipe. See Fig. 1.1 for a schematic view of the flow geometry.

From a modelling perspective, a natural formulation involves a concentration–diffusion equation coupled to the Navier–Stokes equations, in Cartesian $(\hat{x}, \hat{y}, \hat{z})$ or cylindrical coordinates $(\hat{r}, \theta, \hat{z})$. The change between pure heavy and light fluids can be modelled via a scalar concentration, c. We make the Navier–Stokes equations dimensionless using $\hat{D}$ as length scale, $\hat{V}_0$ as velocity scale, and subtracting a mean static pressure gradient before scaling the reduced pressure, we arrive at

$$(1-\phi At)\left(\mathbf{u}_t + \mathbf{u}.\nabla\mathbf{u}\right) = -\nabla p + \frac{1}{Re}\nabla^2\mathbf{u} - \frac{\phi\mathbf{e}_g}{Fr^2}, \tag{1.1}$$

$$\nabla.\mathbf{u} = 0, \tag{1.2}$$

$$c_t + \mathbf{u}.\nabla c = \frac{1}{Pe}\nabla^2 c. \tag{1.3}$$

Here, $\mathbf{e}_g = (0, 0, 1)$. The function $\phi(c) = 1 - 2c$ interpolates linearly between 1 and -1 for $c \in [0, 1]$, for displaced and displacing fluids, respectively. The three dimensionless parameters appearing in equation (1.1) are the Atwood number, At, representing a dimensionless density difference, the Reynolds number, Re, and the densimetric Froude number, Fr. The dimensionless parameters of the current paper are defined in Table 1.1. A fourth dimensionless group also appears in equation (1.3), i.e. the Péclet number. In lab/industrial scale flows, the Péclet number is usually very large, implying that for initially-separated fluids, the diffusive effects remain initially limited to thin interfacial layers of size $\sim 1/Pe^{1/2}$. Over experimental timescales in the absence of instability, mixing and dispersion, the interface remains sharp. Experimentally, we are dealing with fluids with large Pe so that we may set $Pe \to \infty$ and ignore the right-hand-side of equation (1.3). By this, we imply that molecular diffusivity does not affect in a major way the flows studied in the timescale of interest. We also restrict our attention to small density differences between the two fluids in the order of $0.02 - 15\%$ (which is the case in our experiments), i.e. $At < 0.075$. For such small density differences, the solution for $At \to 0$ would provide a reasonable approximation. This assumption of negligible At is also required for the incompressibility condition (1.2) to be valid for intermediate c (Boussinesq approximation). Therefore, in general, the effects of the density difference on the acceleration of individual fluids are ignored. However, it should be noted that for such situation, a significant buoyancy effect can still exist. Finally, the pipe aspect ratio (δ^{-1}) is large and fixed in our study. Therefore, the overall aim of the work is to build a quantitative description of various flow regimes, in terms of only two dimensionless parameters (or their combinations), i.e. Re and Fr, assuming $\delta^{-1} \gg 1$, $Pe \to \infty$ and $At \to 0$. Table 1.1 shows that our experiments cover a wide range of Re and Fr.

There are two important combinations of the dimensionless parameters:

$$\chi = \frac{2Re_t}{Fr}, \qquad Re_t = \frac{Re}{Fr}, \tag{1.4}$$

which arise naturally in the context of thin-film flows and exchange flows, respectively. The former represents a balance of buoyancy stresses and viscous stresses due to the imposed flow while the latter evaluates a balance of buoyancy stresses and viscous stresses driven by buoyancy.

1.1.2 Outline

The paper proceeds as follows. Section 1.2 describes the experimental setup and procedures. Various flow regimes are discussed qualitatively and quantitatively in §1.3 and §1.4, respectively. The latter also includes discussions on the stabilizing effect of the imposed flow and a regime classification, demonstrating stable and unstable flow regimes. Section 1.5 concludes the paper with a brief summary of the main findings.

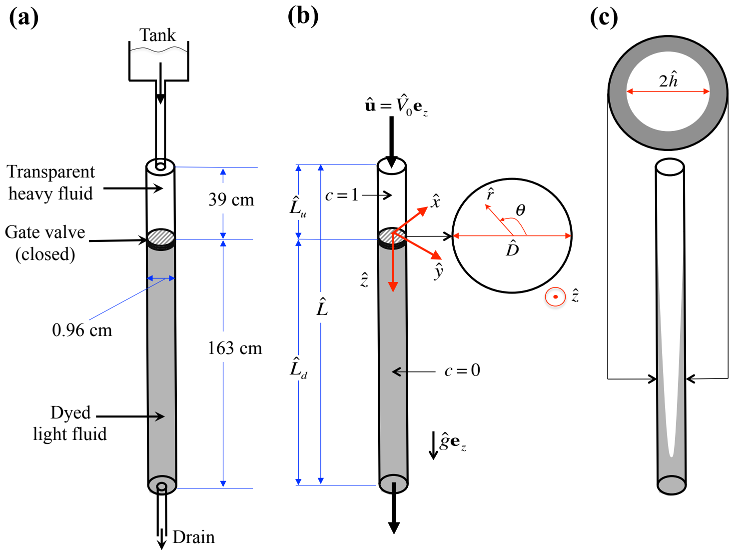

FIGURE 1.1 – Schematic view of (a) the experimental set-up, (b) the geometry with both Cartesian coordinates (appropriate for experimental analyses) and cylindrical coordinates (suitable for modelling) and (c) the stable displacement flow problem considered for the lubrication model (in §1.4.2). Note that the position of the camera for taking experimental images would be in the $\hat{x}$-direction, normalized to the $(\hat{y}, \hat{z})$-plane (in the middle subfigure).

1.2 Experimental setup, procedures, and details

Our experimental study was performed in a 202 (cm) long, 0.96 (cm) diameter, transparent vertical pipe (acrylic with 0.3 (cm) thickness). An automated mini gate valve (VAT Inc.) located 39 (cm) from the top end was included in the system. This gate valve initially separated the two parts of the pipe but it was quickly opened in a smooth way at the beginning of each experiment. Figure 1.1a shows a schematic of our experimental apparatus. All the experiments were performed at an ambient temperature kept at 24 ± 1 (°C).

Initially, the lower part of the pipe was filled using a Masterflex pump with a less dense fluid coloured with a small amount of ink (Fountain Pen India black ink) for visualization purposes. The small amount of the dye used does not change the fluid properties. Light absorption calibrations were performed in usual fashion, for which the amount of 0.6 g of ink per one liter of liquid was found to be a reasonable trade-off. The upper part of the pipe, above the gate valve, was filled by the denser salt-water solution (NaCl). In ambient temperature, the maximum amount of salt that can be dissolved into water (114) determines the possible range of At, which in our case was up to $\sim 0.07 - 0.08$. The densities of our experimental fluids were measured by a high-precision density meter (Anton Paar DMA 35). The viscosities of the solutions were measured in usual fashion, using AR-G2 TA Instrument digital controlled shear stress-shear rate rheometer. The maximum error in measurement of viscosity was 5%. The measurements revealed that the viscosity of the salt-water solutions remains close to that of water in our experiments: the kinematic viscosity was found to be $10^{-6} \leq \hat{\nu} \leq 1.5 \times 10^{-6}$ (m^2/s). For simplicity, in this work, we neglect the small viscosity ratio between the two fluids and consider a common, constant kinematic viscosity for displacing and displaced fluids, i.e. 10^{-6} (m^2/s).

To avoid pump disturbances and ensure smooth steady inflow, the displacing upper fluid was fed by gravity from a large elevated tank. This tank was initially filled with the denser fluid using a gear pump. After filling the upper and lower parts of the pipe by displacing and displaced fluids, air bubbles (if any) stuck in the pipe were released using a two-way straight stainless steel miniature ball valve, installed near the gate valve. The flow rate ($\hat{Q} = \pi \hat{D}^2 \hat{V}_0/4$) was controlled by a needle valve and it was measured by two rotameters, located downstream of the pipe. Each experiment was performed at a fixed density difference and a fixed imposed flow rate. A typical experimental sequence consisted of running a number of experiments at increasing flow rates (note that for each experiment the flow rate was fixed). At the start of the experiment, the gate valve was opened. Images of the displacement fluid were recorded using a high-speed camera (Basler acA2040, with 4096 gray-scale levels) covering ~ 80 (cm) below the gate valve, and they were subsequently post-processed using in-house Matlab codes, to quantify different aspects of the flow. To enhance the quality of the images, the pipe was back-lit using Light-Emitting Diode (LED) strips. In addition, to improve light homogeneity, a diffusive layer was placed between the pipe and the LED strips. Table 1.2 shows the ranges/values of the dimensional parameters in our experiments.

Before proceeding, we would like to clarify a point about molecular diffusion, the value of which does not affect the overall flow as long as it is small. In this work, we assume that molecular diffusivity between water and salt-water solutions in our experiment remains small, taken to be $\hat{D}_m \approx 2 \times 10^{-9}$ (m^2/s). This assumption is supported by the following argument. The self-diffusion coefficient for pure liquid water at an ambient temperature is 2.3×10^{-9} (m^2/s) (115). It is also known that for "structure-making" salts (like NaCl), by increasing salt concentration from 0 to 5.9 molalities (which roughly corresponds to the range of the salt concentration used in our experiments), self-diffusion coefficient of the water molecules decreases from 2.17×10^{-9} to 1.43×10^{-9} (m^2/s) (116; 117). Therefore, it seems that considering small $\hat{D}_m$ is a valid assumption.

In order to ensure about the performance and reliability of the experimental apparatus as well as validate our experimental results, various comparisons were made with the available data in the literature (18; 41; 46). In particular, the front velocities of the penetrating fronts were compared with those of displacement flows (18), exchange flows in vertical pipe (41) and exchange flows in inclined pipes (46). Reasonable agreement with the previous reports was found. For example, the comparison between our front velocities and those of (46) at $At = 10^{-2}$ in a pipe with a slightly different diameter showed a difference of $\sim 7\%$ (on

TABLE 1.2 – Range of the dimensional parameters used in our experiments.

Parameter	Name	SI Unit	Range or value
$\hat{V}_0$	Mean imposed flow velocity	m/s	$0 - 202 \times 10^{-3}$
$\hat{\rho}_H$	Heavy fluid's density	kg/m^3	$998.2 - 1148.2$
$\hat{\rho}_L$	Light fluid's density	kg/m^3	998
$\bar{\hat{\rho}} = \frac{\hat{\rho}_H+\hat{\rho}_L}{2}$	Mean fluid's density	kg/m^3	$998.1 - 1073.1$
$\hat{D}$	Pipe diameter	m	9.6×10^{-3}
$\hat{L}$	Total pipe length	m	2.02
$\hat{L}_u$	Pipe length (upstream) above the gate valve	m	0.39
$\hat{L}_d$	Pipe length (downstream) below the gate valve	m	1.63
$\hat{\nu} = \frac{\hat{\mu}}{\hat{\rho}}$	Kinematic viscosity	m^2/s	$\sim 10^{-6}$
$\hat{D}_m$	Molecular diffusivity	m^2/s	$\sim 2 \times 10^{-9}$

average), for various inclinations up to 15° from vertical. This difference is within the order of the accuracy of the front velocities measured. Even a number of experiments were performed for a density-stable configuration, for which a reasonable agreement was found with the available data in the open literature (i.e. $\hat{V}_f \approx \hat{V}_0$ at longer times) (89).

1.3 Qualitative description of various flows

We begin with a qualitative description of the main flow features observed in our displacement flow experiments. One of the novel aspects of the current work is studying displacement flows at a wide range of At, covering almost three orders of magnitude. For exchange flows ($\hat{V}_0 = 0$), almost the same range of At has been studied in details by Debacq *et al.* (40; 41). Therefore, as a first step, it is natural to examine how global qualitative behaviours observed for exchange flows in (40; 41) are affected by gradually introducing the mean imposed flow ($\hat{V}_0 > 0$). As a second step, it would be interesting to see various qualitative flow behaviours for a fixed non-zero mean imposed flow velocity at different values of At.

Fig. 1.2 shows a sequence of experimental images for a fixed small At. The experimental snapshots shown here are calibrated so that the colours vary between 0 (dark displaced fluid) and 1 (transparent displacing fluid). At $\hat{V}_0 = 0$, there exists a countercurrent flow (note that only the downstream is shown). In this case, at short times there are some instabilities between the finger of the heavy fluid and the surrounding displaced fluid; however, these instabilities are unable to mix the two fluids. In fact, the helical instability of the wave decays after a few pipe diameters particularly at much longer times; see also (41). The flow at long times demonstrates a stable countercurrent flow. By introducing a small mean imposed flow velocity, i.e. $\hat{V}_0 = 3$ (mm/s), the flow is significantly affected: two effects are clearly observed. First, it seems that at $\hat{V}_0 = 3$ (mm/s), we have transitioned from a countercurrent flow to

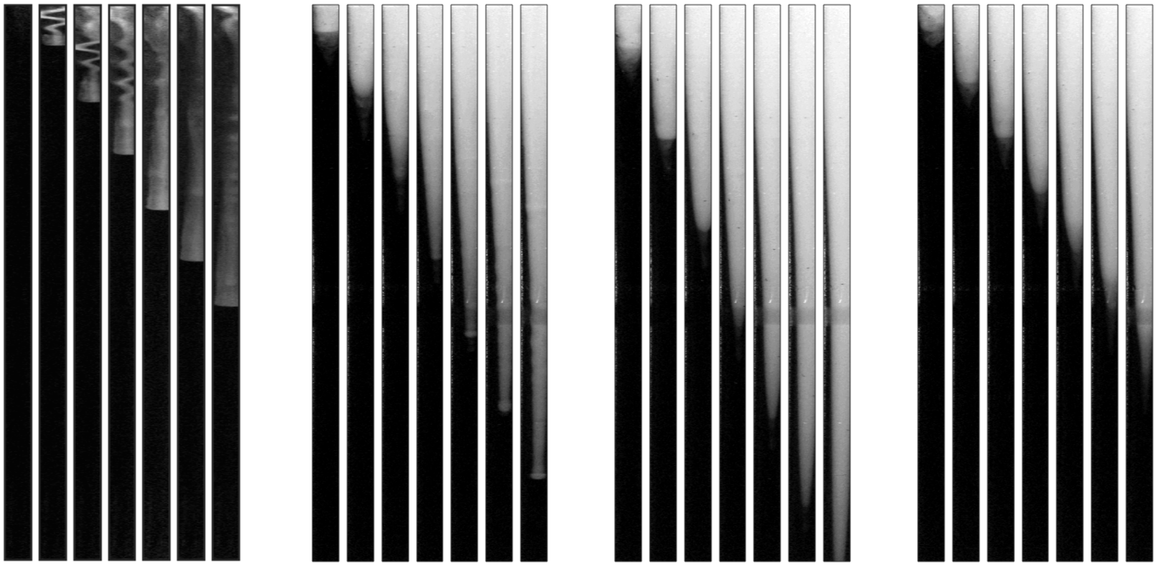

FIGURE 1.2 – Sequence of experimental images for a fixed Atwood number ($At = 10^{-4}$), showing that the inertial tip (i.e. bubble shape front) observed initially for $\hat{V}_0 = 0$ is progressively spread out by increasing the mean imposed flow velocity ($\hat{V}_0 \neq 0$). From left to right, $\hat{V}_0 = 0,\ 3,\ 8,\ 12$ (mm/s) in each panel. The experimental times in each panel are $\hat{t} = [25, 100, 200, 300, 400, 500, 600]$ (s), $\hat{t} = [16, 32, 48, 64, 80, 96, 112]$ (s), $\hat{t} = [8, 16, 24, 32, 40, 48, 56]$ (s), and $\hat{t} = [4, 8, 12, 16, 20, 24, 28]$ (s), from left to right. The field of view in each snapshot is 8×805 (mm^2), located 24 (mm) below the gate valve. In this and the other figures, the camera images shown have an offset of a few pixels with respect to the pipe center-line.

a displacement flow, where no upward motion of the displaced fluid is observed. Second, the mean imposed flow seems to have reduced the initial interfacial waves and the inertial tip is significantly smaller. At higher mean imposed flow velocities ($\hat{V}_0 = 8$ & 12 (mm/s)), the inertial tip disappears completely. The flow at longer times resembles a Poiseuille-like flow, although the shape of the interface is affected by the presence of the density difference. This is a stable buoyant displacement flow. Throughout this paper, unstable flows are consistently defined as those displacement flows where the interfacial instabilities significantly grow at long times and result in a complete mixing between the two fluids. Otherwise, the displacement flow is defined as stable.

Although in Fig. 1.2, we have observed the general stabilizing effect of the imposed flow, it should be noted that for higher imposed flows, the initial mixing at very short times is more pronounced for displacement flows. For $\hat{V}_0 \neq 0$, by looking at the concentration field, it is interesting to note the transition from a nearly uniform profile at short times to a Poiseuille-like profile at longer times.

Compared to the previous figure, Fig. 1.3 shows a sequence of experimental images for a fixed

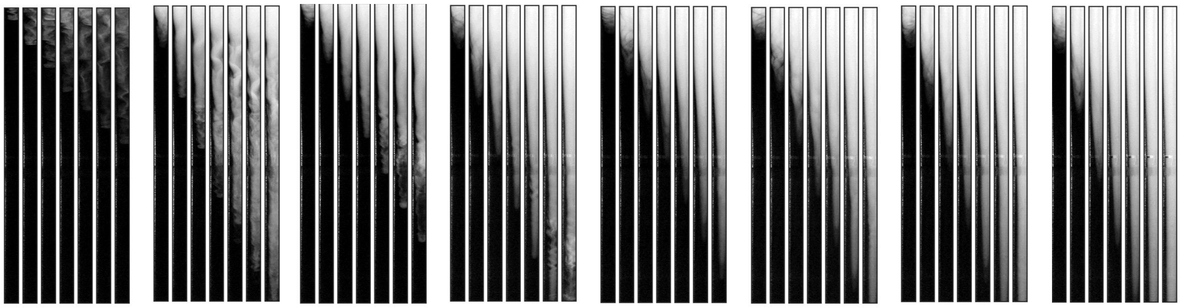

FIGURE 1.3 – Sequence of experimental images for $At = 10^{-3}$, showing that the inertial flow at small $\hat{V}_0$ transitions to a stable flow at larger $\hat{V}_0$. From left to right, $\hat{V}_0 = 0$, 15, 22, 34, 44, 55, 64, 75 (mm/s) in each panel. From left to right, the experimental times in each panel are $\hat{t} = [15, 30, 45, 60, 75, 90, 105]$ (s), $\hat{t} = [4, 8, 12, 16, 20, 24, 28]$ (s), $\hat{t} = [2, 4, 6, 8, 10, 12, 14]$ (s) (the 3^{rd} & 4^{th} panels form the left), $\hat{t} =[1.25, 2.5, 3.75, 5, 6.25, 7.5, 8.75]$ (s) (the 5^{th}, 6^{th}, 7^{th} & 8^{th} panels from the left). The field of view in each snapshot is 8×805 (mm^2), located 24 (mm) below the gate valve.

but higher Atwood number, i.e. $At = 10^{-3}$. This figure shows more clearly the stabilizing effect of the imposed flow at a higher Atwood number. At $\hat{V}_0 = 0$, the flow is evidently unstable and the fluids are mixed through a convective-diffusive mechanism (41), where the internal structure of the flow is visible. As the mean imposed flow velocity increases, the overall mixing seems to be reduced and finally, at a certain imposed flow velocity (here $\hat{V}_0 = 44$ (mm/s)), the flow is completely stabilized. Compared to Fig. 1.2, due to strong buoyancy, we need a much larger mean imposed flow velocity to completely stabilize the flow.

For very large values of Atwood number ($At \geq 0.01$), we never observed a complete stabilization of the flow at any values of $\hat{V}_0$. This might be expected as the mean imposed flow velocities necessary for stabilizing the displacement flow at higher imposed flow rates are perhaps so large that they fall into a regime characterized by a turbulent imposed flow, which itself would promote instability and mixing.

It is worth noting that Figs. 1.2 and 1.3 showed that at short times when the heavy fluid starts to penetrate into the light fluid, the fluids are accelerated initially. In fact, in all of our experiments we have observed that, regardless of the long time behaviour of the flow, the displacement flow at short times is inertial.

In a nutshell, Figs. 1.2 and 1.3 showed that by introducing the imposed flow to an exchange flow, the displacement flow in a vertical pipe could be stabilized. For nearly horizontal inclinations, it has also been found that an imposed flow can counter-intuitively stabilize the flow through increasing the local gradient Richardson number (85). Loosely speaking, increasing the local gradient Richardson number may be interpreted as increasing the densimetric Froude number, which is preferred as a model parameter. Therefore, the stabilizing effect of the imposed flow in our case can be related to the increase in the densimetric Froude number as $\hat{V}_0$

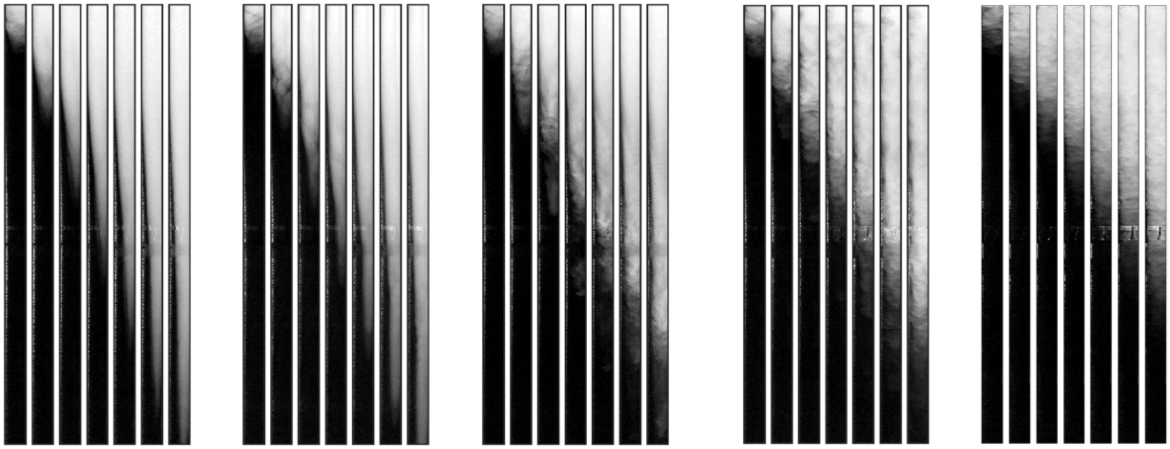

FIGURE 1.4 – Experimental image sequence for $\hat{V}_0 = 54 \pm 1$ (mm/s) and $At = 10^{-4}, 10^{-3}, 3.5 \times 10^{-3}, 10^{-2}, 7 \times 10^{-2}$ from left to right in each panel. The experimental times in each panel are $\hat{t} = [1.25, 2.5, 3.75, 5, 6.25, 7.5, 8.75]$ (s). The field of view in each snapshot is 8×805 (mm^2), located 24 (mm) below the gate valve.

increases. Alba *et al.* (18) have also studied displacement flows at various pipe inclinations, including a few experiments for the vertical case. They have reported mostly destabilizing effects due to the imposed flow along with some limited stabilizing effects observed for inclined pipes; however, they could not observe a completely stabilized flow in their vertical pipe. This is perhaps due to the fact that their study was limited to relatively larger Atwood numbers compared to our case and their experiments were performed in a pipe with a diameter larger than ours.

We mentioned in the introduction that the transition between stable and unstable exchange flows is governed by a single dimensionless number and it occurs at a critical $Re_t|_{Critical} \approx 79$. For displacement flows, Fr is added as another dimensionless parameter of the flow. Therefore, one can argue that, as the imposed flow is gradually added to the exchange flow, the critical transition between stable and unstable flows must depend on the value of Fr. As will be shown later, this proves to be true. We will further analyse this when discussing the overall regime classification.

Fig. 1.4 shows the difference between the displacement flows at various At, for a fixed value of the mean imposed flow velocity. As can be seen, for the flows at higher At, the level of disorder increases, the flows are more inertial, and the degree of transverse & axial mixing seems higher.

1.4 Quantitative results

We will start this section with semi-quantitative descriptions of the stabilizing effect of the imposed flow on our displacement flows. We will then take an extended look into stable and unstable flow regimes. We end this section by providing the overall regime classifications versus the dimensionless groups.

1.4.1 Stabilizing effect of the imposed flow

In the previous section, we observed that introducing or increasing the mean imposed flow velocity can stabilize some of the buoyant flows studied. In this section, we attempt to provide a further understanding of this interesting flow feature.

The normalized experimental images of the displacement flow captured by the camera provide a digital concentration map with a two-dimensional mesh of normally around $N \times M = 20 \times 2018$ pixels in the transverse and longitudinal directions of the pipe, respectively. This usually covers a field of view of $\sim 0.8 \times 80$ (cm^2) below the gate valve. Considering the location of the camera with respect to the pipe, each image shows the pipe side view in the $\hat{y}, \hat{z}$-plane (see Fig. 1.1b). Thus, through the images captured we do not have access to the real concentration field, i.e. $C(x, y, z, t)$, since the concentrations are already averaged over the $\hat{x}$ direction when an image is taken. Consequently, within the limits of the camera resolution, each normalized image provides us instead with a digital approximation to $\bar{C}_x\left(y, z, t\right) = \int_{-1/2}^{+1/2} C\left(x, y, z, t\right) dx$. For example, for a given t, each picture is a matrix delivering $\bar{C}_x\left(y_j, z_k, t\right)$ where $j \in [1, N]$ and $k \in [1, M]$.

One approach to quantify the amount of dispersion in the data sets of $\bar{C}_x\left(y_j, z_k, t\right)$ is to use the standard deviation, defined as $\sigma_y\left(z, t\right) = \sqrt{\frac{1}{N} \sum_{j=1}^{N} \left(\bar{C}_x\left(y_j, z, t\right) - \varsigma\left(z, t\right)\right)^2}$, where $\varsigma\left(z, t\right) = \frac{1}{N} \sum_{j=1}^{N} \bar{C}_x\left(y_j, z, t\right)$. Fig. 1.5 shows the variation of σ_y along the pipe length for various values of density difference and mean imposed flow velocity. For a given z, the value of σ_y provides a measure of the transverse mixing. For $At = 10^{-4}$, two observations can be made. First, large values of σ_y indicate a clear segregation between the displacing and displaced fluids. Second, by increasing $\hat{V}_0$ (from top to bottom), the differences between the graphs on the left are minor. This implies that after the initial stabilizing effect when an imposed flow is added to an exchange flow, a further increase in $\hat{V}_0$ does not modify the overall form of the displacement flow. For $At = 10^{-3}$, at lower $\hat{V}_0$, the curve of σ_y versus z is oscillatory. At larger mean imposed flow velocities, the curve is smooth. In addition, the maximum values of σ_y are slightly larger confirming that increasing the mean imposed flow velocity stabilizes the flow. As At increases, the differences between the graphs showing a sequence of increasing the imposed flow velocity become minor, for the range of $\hat{V}_0$ studied. In fact at $At = 0.07 \times 10^{-2}$, $\sigma_y \to 0$ for all values of z, implying a nearly complete transverse mixing throughout the pipe for all the values of

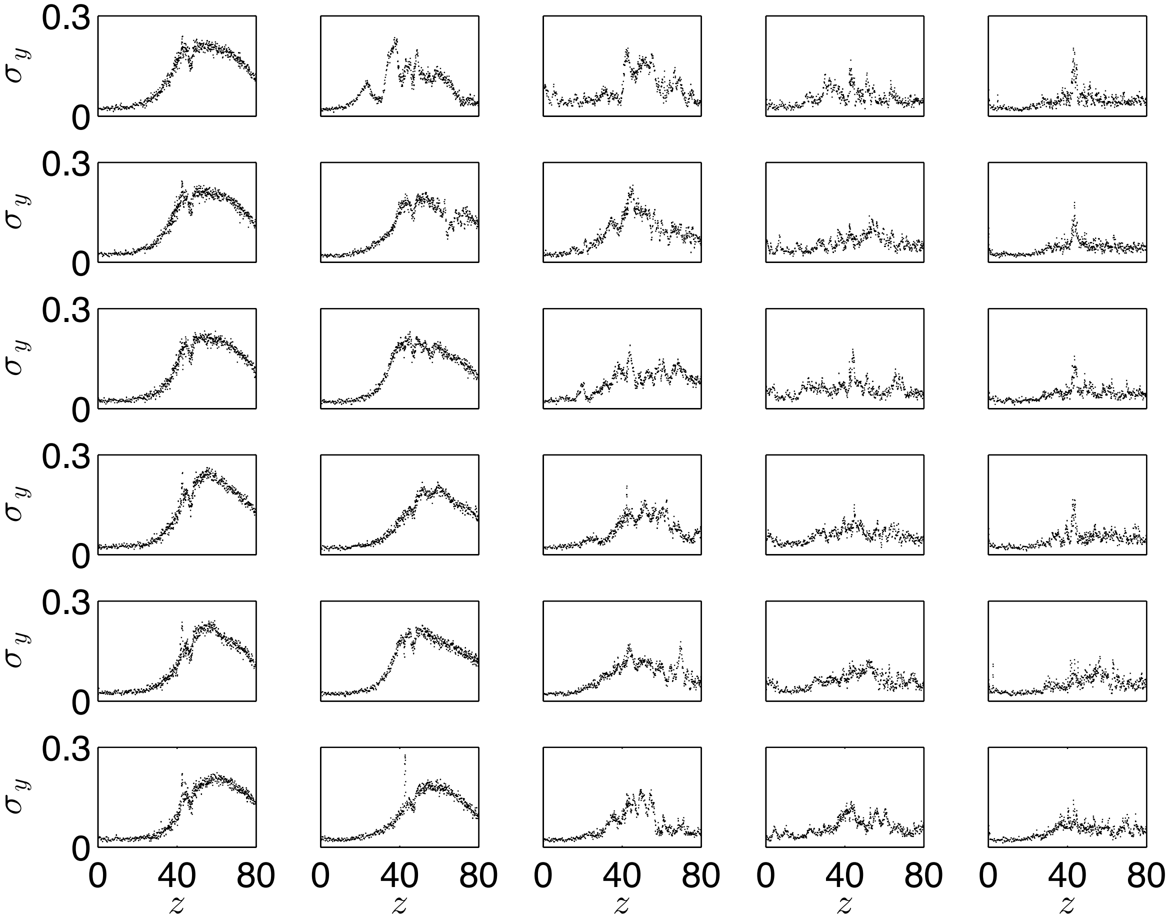

FIGURE 1.5 – Standard deviation σ_y versus z when the displacing front is at $z_f \approx 84$ and $t = 49 \pm 4$ for $At = 10^{-4}$, 10^{-3}, 3.5×10^{-3}, 10^{-2}, 7×10^{-2} (from left to right) and $\hat{V}_0 = 23 \pm 2$, 34 ± 1, 43 ± 1, 54 ± 1, 63 ± 2, 74 ± 1 (mm/s) (from top to bottom).

$\hat{V}_0$.

1.4.2 Stable flow regime

Displacement flows in the configuration that we study are highly susceptible to the growth of instabilities. However, we interestingly observe that for certain ranges of the dimensionless parameters, the flow is completely stable. Therefore, it is natural to attempt to develop a lubrication/thin-film type model for these stables flows to furnish predictions about the flow behaviours of interest.

Lubrication model

For small At and small imposed flow rates, within the initial few seconds after the beginning of each experiment, the fluids are highly accelerated so the flow is initially inertial. Due to this flow feature, the fluids are initially slightly mixed. However, after this period has passed, the two fluids are completely segregated and a relatively sharp displacement interface separates the two fluids. The flow away from the displacing front seems quite viscous and stable. At long times, as the interface is sufficiently stretched, the displacing fluid advances through the displaced fluid in a form that may resemble an axisymmetric core-annular shape flow. It is, therefore, useful to develop a standard thin-film/lubrication style model for such a flow. We use a cylindrical coordinate system, which is more appropriate for modelling, with (r, θ, z) and $\mathbf{u} = (u_r, u_\theta, u_z)$. Due to the axisymmetric condition of the flow, the problem reduces to (r, z) and (u_r, u_z). The leading order equations are the momentum balances:

$$0 = -\frac{\partial P}{\partial r}, \tag{1.5}$$

$$0 = -\frac{\partial P}{\partial Z} + \frac{1}{r}\frac{\partial}{\partial r}\left(r\frac{\partial u_z}{\partial r}\right) \pm \frac{\chi}{2}, \tag{1.6}$$

and the incompressibility condition for each layer

$$\frac{1}{r}\frac{\partial\left(rU_r\right)}{\partial r} + \frac{\partial u_z}{\partial Z} = 0, \tag{1.7}$$

where ± present the heavy and light fluids, respectively. We have rescaled the system using $\delta z = Z$, $\delta t = T$, $\delta p = P$, and $u_r = \delta U_r$, following standard methods (see, e.g. (118)).

At the walls $\mathbf{u} = 0$ and at the interface both velocity and traction vectors are continuous. In the middle we apply the symmetric condition for the velocity profile. For the flows considered, in our experiments $\hat{V}_0$ is imposed by an elevated tank in the positive $\hat{z}$-direction. Thus, the additional flow constraint

$$\frac{1}{4} = \int_0^h 2ru_{z,H}dr + \int_h^{1/2} 2ru_{z,L}dr \tag{1.8}$$

has to be satisfied by the solution. We eliminate pressure in usual fashion and derive the evolution equation

$$\frac{\partial \alpha}{\partial T} + \frac{\partial q}{\partial Z} = 0, \tag{1.9}$$

where $h \in [0, 1/2]$ and $\alpha = h^2$ is the area fraction occupied by the heavier fluid. The solution is simplified to finding the flux, which is scaled with $\pi\hat{D}_0^2\hat{V}_0$, as

$$q = -2\chi h^8 + 2h^6\chi - \left(4 + \frac{1}{2}\chi\ln(h) + \frac{3}{8}\chi + \frac{1}{2}\chi\ln(2)\right)h^4 + 2h^2 \tag{1.10}$$

The interface advances with a shock speed $V_i(h)$ given by

$$V_i(h) = \frac{1}{2h}\frac{\partial q(h,\chi)}{\partial h}. \tag{1.11}$$

The total volume of fluid behind the interface must conserve mass; therefore, introducing V_f^{Lub} and h_f, respectively, as the displacing front speed and height (radius) at long times, we can write

$$V_f^{Lub} = \frac{q\left(h_f, \chi\right)}{h_f^2}, \tag{1.12}$$

where h_f must be found through the use of the conventional *equal areas rule*:

$$\frac{h_f}{2}\frac{\partial q\left(h_f, \chi\right)}{\partial h} = q\left(h_f, \chi\right). \tag{1.13}$$

Using truncated series expansion and after some algebra, the front velocity can be obtained as

$$V_f^{Lub} = 2 - \left(8 + \chi\left(\ln\left(2h_f\right) + 1\right)\right) h_f^2 + O(h_f^4), \tag{1.14}$$

where

$$h_f = \exp\left(-\frac{\chi\left(4\ln\left(2\right) + 5\right) + 32}{4\chi}\right) + O(h_f^2). \tag{1.15}$$

We have so far found the penetrating interface front height and front velocity versus the governing parameter of the lubrication problem, i.e. χ. In addition, the lubrication model can be exploited to extract more information about the stable flows. In particular, we are able to quantify a marginal state called the stationary interface flow for displacement flows in a vertical pipe. Taghavi *et al.* (86) were perhaps first to discover the existence of a stationary interface propagation in Newtonian displacement flows. Their cases of study were the displacement flows in near-horizontal pipes and 2D channels. In these flows, a displaced fluid layer is apparently stationary with a constant flow rate of displacing heavy fluid. Mathematically speaking, in our case, this implies that the interfacial speed is zero while the dimensionless flux is 1/4 at the interface. In fact, we observe that in our experiments, the interface remains stationary for the duration of the experiment while the flow rate of displacing heavy fluid is constant. The calculations result in finding the critical buoyancy number (χ_s) and a critical interface height (h_s) for stationary interface flows:

$$h_s \approx 0.377 \tag{1.16}$$

$$\chi_s \approx 230 \tag{1.17}$$

As we will see in §1.4.4, the marginal state of stationary interface flow (which occurs at $\chi_s \approx 230$) provides a prediction of the transition between two sub-regimes in stables flow, i.e. sustained-back-flow and no-sustained-back-flow regimes.

Table 1.3 – Values of the critical buoyancy number (χ_s), the total stationary layer width (W_s) and the ratio of the stationary layer volume to the tube volume ($\cancel{V}_s$) for displacement flows in various 3D pipe and 2D channel flow configurations. The length scale used is either the pipe diameter or the channel thickness. (1) See the main text for the development details. (2) See Appendix A for development details. (3) This value is taken from Taghavi *et al.* (86). For consistency with the previous works, the buoyancy number can be defined as $\chi = 2Re_t \cos\beta/Fr$, where β is the geometry inclination angle with respect to the vertical.

Flow configuration	χ_s	W_s	$\cancel{V}_s$
Displacement flow in a strictly vertical pipe	$230^{(1)}$	0.25	0.44
Displacement flow in a strictly vertical channel	$118^{(2)}$	0.34	0.34
Two-layer displacement flow in a near-horizontal pipe	$116^{(3)}$	0.28	0.23
Two-layer displacement flow in a near-horizontal channel	$70^{(3)}$	0.29	0.29

Note on the effect of geometry & flow configuration on the stationary interface state

Before proceeding, it is interesting to compare the value of the critical buoyancy number χ_s for our displacement flow in a vertical pipe with those in the literature for other geometries & flow configurations. Table 1.3 shows such comparison. In this table, the critical buoyancy number (χ_s), the total stationary layer width (W_s), and the ratio of the stationary layer fluid volume left behind ($\cancel{V}_s$) are given for each flow configuration & geometry. The lubrication model for a symmetric displacement flow in a vertical channel is also developed in the appendix A, to complete the picture. The values of χ_s for the two other geometries are taken from the literature. The first trend that can be seen is that χ_s is the largest for the vertical pipe geometry and it is the smallest for the near-horizontal 2D channel. In addition, while the thickness of the static layer is the smallest for the vertical pipe flow, the volume of the fluid behind the interface at the stationary interface flow condition is the largest (which is just a geometrical effect).

Front velocity in the stable regime

For the stable flows, we may expect the lubrication model to deliver a good approximation to the penetrating front velocity at longer times. However, as mentioned before, we have experimentally seen that the flow undergoes an initial acceleration and the front velocity rapidly increases to attain its nearly steady-state value. For a single purely viscous liquid, the solution of the startup Poiseuille flow reveals that the characteristic time required for such acceleration through a viscous balance would scale with $\frac{\hat{D}^2}{\hat{\nu}}$, for example, ~ 92 (s) for a typical flow. However, our experimental observations reveal that the initial acceleration time, which we may define as the time when $\hat{V}_f(t)$ reaches 99% of its final value, is much shorter. Therefore, the flow has to accelerate through a different mechanism, which includes a significant contribution from inertial effects. We have already seen that the initial inertial

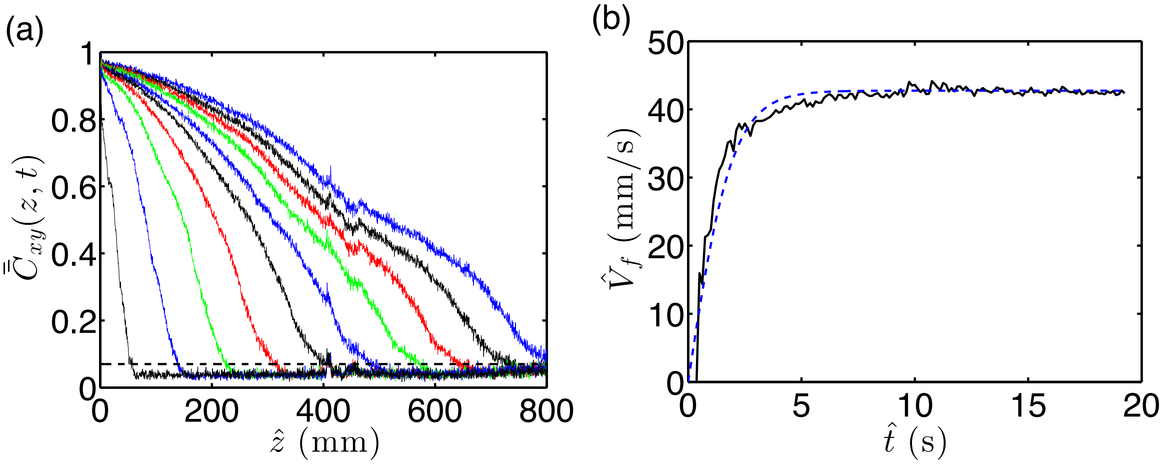

FIGURE 1.6 – Experimental results for $At = 10^{-4}$ and $\hat{V}_0 = 22$ (mm/s): (a) Evolution of the depth-averaged concentration field, $\bar{\bar{C}}_{xy}(z,t) = \int_{-1/2}^{+1/2} \bar{C}_x(y,z,t)\,dy$ with time, $\hat{t} = [2, 3.875, 5.875, 7.75, 9.75, 11.625, 16.625, 15.5, 17, 19.375]$ (s), and streamwise location, $\hat{z}$, measured from the gate valve. The horizontal dashed lines show $\bar{\bar{C}}_{xy}(z,t) = 0.07$, just above the noise level, which is used for measuring the displacing front velocity, $\hat{V}_f$, consistently for all the experiments. (b) Evolution of the front velocity value, $\hat{V}_f$, with time for the same experiment (solid line). The dashed line shows the prediction of the model, as explained in the text.

acceleration also induces slight mixing between the two fluids, which we ignore for simplicity in our analysis in this section.

Fig. 1.6a shows an example of the evolution of the average concentration field with time and streamwise location. The figure shows that the interface evolves stably and smoothly. The front velocity of the penetrating heavy displacing fluid can be approximated by following the $\hat{z}$-location of a small $\bar{\bar{C}}_{xy}$ above the noise, e.g. $\bar{\bar{C}}_{xy} \approx 0.07$ to give $\hat{V}_f \approx \left.\frac{\hat{z}}{\hat{t}}\right|_{\bar{\bar{C}}_{xy}=0.07}$. Ideally, since the fastest penetration is expectedly at the pipe center-line, the front should be defined and quantified at $\bar{\bar{C}}_{xy} = 0$, which is not possible due to experimental noise. Instead, $\bar{\bar{C}}_{xy} \approx 0.07$ has been found as the minimum value of $\bar{\bar{C}}_{xy}$ which always remains above the experimental noise for all of our experiments. Thus, it may be expected that the front velocities measured slightly underestimate the largest penetration velocity at the pipe center-line. The line in Fig. 1.6b shows the front velocity that corresponds to the same parameters of the subfigure on the left. The dashed line shows the prediction of our model that will be described below.

For a comparable system to ours where a purely inviscid fluid flows from a large tank into a long pipe, it can be easily shown that the flow velocity is $\sqrt{2\hat{g}\hat{H}}\tanh\left(\frac{\hat{t}}{\hat{\tau}}\right)$, where $\sqrt{2\hat{g}\hat{H}}$ corresponds to the final velocity in the inviscid flow, $\hat{H}$ is the tank height, and $\hat{\tau}$ is the time constant of the dynamic system. Using an analogy to the system described, we can postulate a time-dependent form for the displacing front velocity as $\hat{V}_f(t) = \hat{V}_f^{\infty}\tanh\left(\frac{\hat{t}}{\hat{\tau}}\right)$, where $\hat{V}_f^{\infty}$ is

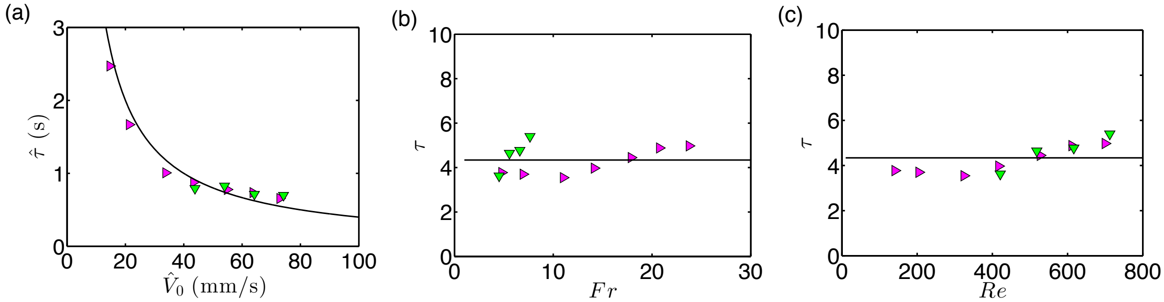

FIGURE 1.7 – (a) Variation of the time constant of the dynamic system $\hat{\tau}$ versus $\hat{V}_0$ for $At = 10^{-3}$ (green filled pointed-down triangle) and $At = 10^{-4}$ (magenta filled pointed-right triangle), which both belong to stable flows. (b) Variation of the dimensionless time constant of the dynamic system τ with Fr. (c) Variation of the dimensionless time constant of the dynamic system τ with Re. In all the subfigures, the line illustrates $\tau = 4.34$, which is simply an average of the dimensionless time constants, with a standard deviation of 0.64.

the final front velocity at long times. Our experimental results have shown that $\hat{V}_f^{\infty} \approx \hat{V}_f^{Lub}$ (results are not shown). In a given experiment, the values of $\hat{V}_f$ versus $\hat{t}$ and $\hat{V}_f^{\infty}$ are available; therefore, $\hat{\tau}$ can be directly calculated for each experiment.

Fig. 1.7a shows the variation of the time constant of the dynamic system $\hat{\tau}$ extracted for a number of experiments versus $\hat{V}_0$. Figs. 1.7b and 1.7c show that the dimensionless form of the time constant is not so much dependent on Fr and Re for a wide range of these parameters. This allows us to use the average time constant (from all the experiments shown) to propose the following relation for the time-dependent front velocity:

$$V_f = V_f^{Lub} \tanh\left(\frac{t}{\tau}\right), \tag{1.18}$$

where $\tau = 4.34$.

Fig. 1.8 compares time-dependent front velocities from our experiments and those from equation (1.18) for many data sets. The agreement between the model and the experiments is reasonable. However, at long times, the values of V_f from experiments are generally slightly smaller than their model counterparts. This may be at least due to two factors: First, the experimental front velocities are measured at $\bar{\bar{C}}_{xy} \approx 0.07$, not exactly in the middle of the channel (where the flow is expectedly faster); second, the fluids initially slightly mix, which reduces the density difference near the front (thus buoyancy becomes weaker) and this may contribute to smaller front velocities measured from our experiments.

1.4.3 Unstable flow regime

We now turn to describe some of the features of the unstable flow regime.

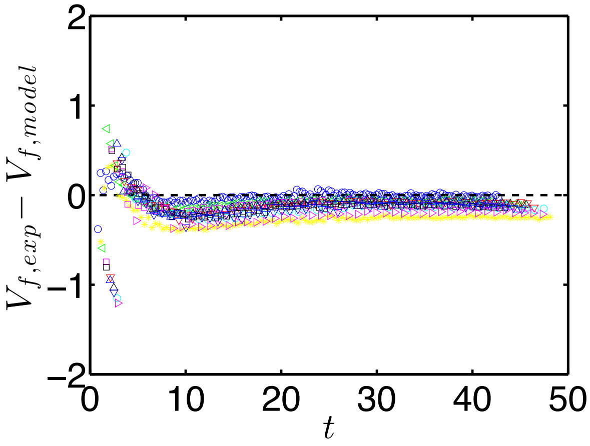

FIGURE 1.8 – $V_{f,exp} - V_{f,model}$ against t: comparison between the dimensionless experimental front velocity ($V_{f,exp}$) and the predicted model front velocity ($V_{f,model}$) from equation (1.18) versus time, for many sets of experiments in the stable flow regime.

Front detachment

Using direct numerical simulation (DNS) in tilted channels, Hallez *et al.* (71) studied buoyant mixing of miscible fluids for an exchange flow configuration. They reported striking differences between the flow dynamics in 2D channels and 3D pipes, which they attributed to strong, coherent and persistent vortices, over long times in 2D. This resulted in discovering the phenomena of cutting front in 2D geometries. Later, again through numerical simulations of flow in 2D channels, Alba *et al.* (19) observed similar phenomena for miscible displacement flows, which they termed front detachment. However, front cutting or detachment has not been seen before in 3D pipe geometries so that previous reports have concluded that this feature might be only relevant to 2D displacements (which are not essentially physical or relevant to realistic fluid flows). Interestingly, even fluid flows featuring instability, interfacial waves and mixing have not been previously found to be prone to cutting of the stream between the front and the bulk heavy fluid. For example, Hallez *et al.* (71) found that 3D pipe allows for the penetrating buoyant front to always remain connected to the bulk of the heavy fluid following from behind. Here, we report for the first time the occurrence of front detachment for 3D pipe flow experiments. In the following section, we will also characterize this phenomenon versus the relevant dimensionless parameters.

The top subfigure in Fig. 1.9 is the image sequence showing the concentration field at different times for an unstable flow experiment. The front, for which the streamwise location is defined as $\hat{z}|_{\bar{C}_{xy}=0.07}$, is initially attached to the displacing layer. However, at longer times the front is cut off from the rest of the bulk flow of the displacing fluid. When this piece of the fluid is cut, a new front is formed behind. This piece of fluid falls down faster than the rest of the fluid but due to instabilities, it is quickly mixed with the surrounding displaced liquid and finally

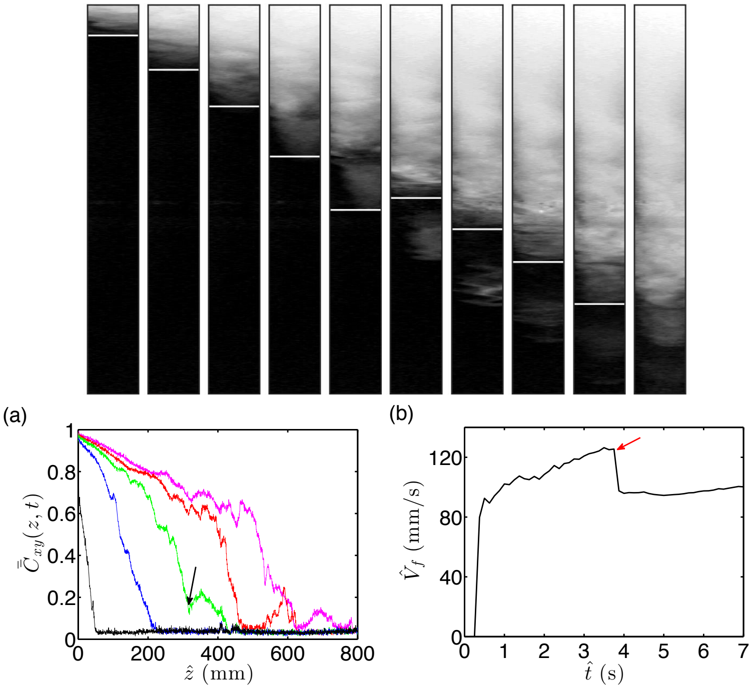

FIGURE 1.9 – Experimental results for $At = 3.5 \times 10^{-3}$ and $\hat{V}_0 = 65$ (mm/s): (Top) Image sequence showing the detachment of the front: from left to right $\hat{t} = [0.75, 1.5, 2.125, 2.875, 3.625, 4.375, 5.125, 5.75, 6.5, 7.25]$ (s). The horizontal line is the position of the defined front. The field of view in each snapshot is 7×805 (mm^2), located 24 (mm) below the gate valve. (a) Evolution of the depth-averaged concentration field $\bar{\bar{C}}_{xy}(z,t) = \int_{-1/2}^{+1/2} \bar{C}_x(y,z,t)\,dy$ with times $\hat{t} = [0.75, 2.125, 3.625, 5.125, 6.5]$ (s), and streamwise location, $\hat{z}$, measured from the gate valve. The arrows show the position where the front is detached from the bulk displacing flow. (b) Evolution of the front velocity value, $\hat{V}_f$, with time for the same experiment. The arrows show the time when the front is detached from the bulk flow.

diminishes. Fig. 1.9a shows the depth-averaged concentration field versus $\hat{t}$ and $\hat{z}$, where the formation and diminishing processes are more visible. The change in concentration near the frontal region is evident. Fig. 1.9b shows the variation of the front velocity with time, where a significant drop in the value of the front velocity measured is also evident.

For a 2D channel geometry, simulations of Alba *et al.* (19) looked into the vorticity field, which is generated close to the front, and which decays behind the front. They showed that for inclined channel displacement flows, there exist both negative and positive values of vorticity on the upper and lower sides of the front. This implies that there are tiny rotational regions of current creating local back-flow and mixing, for which the cause is instability close to the interface and within the two fluid regions. Although our configuration and more importantly our geometry are different, the same mechanism may also be present and be the cause of the front detachment in our case. However, it should be noted that our 3D geometry allows for azimuthal secondary flows, which can modify the vorticity field. It seems that more research

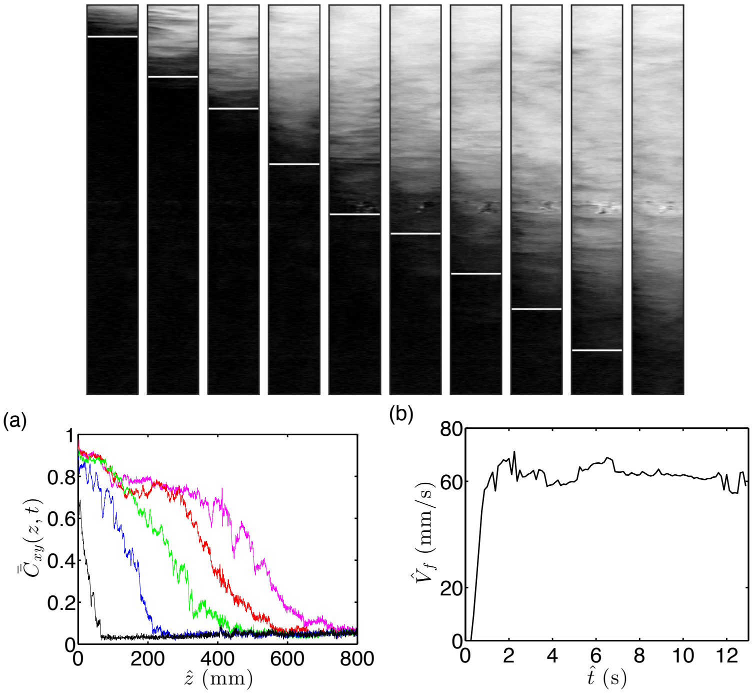

FIGURE 1.10 – Experimental results for $At = 10^{-2}$ and $\hat{V}_0 = 34$ (mm/s): (Top) Image sequence showing the detachment of the front: from left to right $\hat{t}$ =[1.25, 2.625, 3.875, 5.25, 6.5, 7.75, 9.125, 10.375, 11, 13] (s). The horizontal line is the position of the defined front. The field of view in each snapshot is 7×805 (mm^2), located 24 (mm) below the gate valve. (a) Evolution of the depth-averaged concentration field, $\bar{\bar{C}}_{xy}(z,t) = \int_{-1/2}^{+1/2} \bar{C}_x\,(y,z,t)\,dy$ with time, $\hat{t}$ =[1.25, 3.875, 6.5, 9.125, 11] (s), and streamwise location, $\hat{z}$, measured from the gate valve. (b) Evolution of the front velocity value, $\hat{V}_f$, with time for the same experiment.

must be conducted for the 3D geometry pipe displacement flow to shed light on the exact mechanism for the front detachment. High quality numerical simulations in 3D and particle image velocimetry (PIV) or Ultrasonic Doppler Velocimetry (UDV) experiments are among the possible options for future research.

Within the unstable flows, the front detachment phenomena occur at relatively smaller density differences and higher imposed velocities. Both of these imply that for the front to be cut, the relative buoyancy stress must be smaller. For higher buoyancy forces, the density contrast at the front is small due to efficient mixing; in fact, the front is formed within a highly diffusive layer where it seems to be continuously mixed with the displaced fluid and therefore it is continuously consumed by the displaced layer. In this case, there would be no opportunity for the front to keep a significant density difference and then be cut and fall down separately. Hence, displacement flows with front detachment and those without are phenomenologically different. The top image sequence in Fig. 1.10 illustrates a case where the density difference is larger and the front is not cut. Fig. 1.10a shows the depth-averaged concentration field versus $\hat{t}$ and $\hat{z}$, where the concentration field is oscillatory but there is no significant cut at the front.

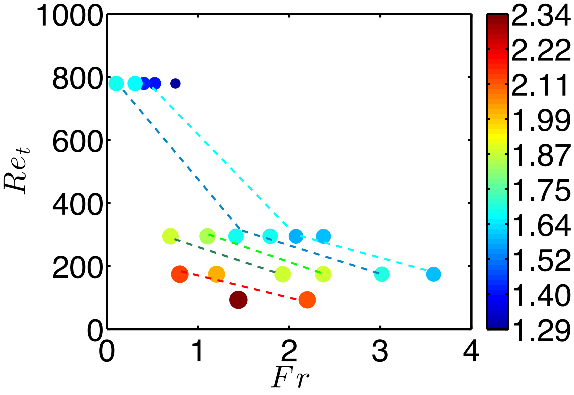

FIGURE 1.11 – Average front velocity V_f at long times, plotted against Fr and Re_t, for the unstable flows. The dashed lines are illustrative to suggest possible contour lines over which the normalized velocities are nearly constant.

Fig. 1.10b shows the variation of the front velocity with time.

Front velocity in the unstable regime

Front velocities in the unstable regime cannot be predicted by the lubrication model. Although buoyancy is strong, mixing and diffusion dominate the flow and the front velocities are much smaller than those predicted by the lubrication model. Fig. 1.11 shows the values of some of the experimental front velocities for unstable flows plotted in the plane of Re_t and Fr. This figure helps to understand two aspects of the flow. First, there is a clear trend in terms of the dimensionless parameters. For a given Re_t, increasing Fr leads to a decrease in the front velocity. Similarly, for a given Fr, increasing Re_t leads to the same effect. It is also evident from the figure that the flows with different V_f are clearly scattered but illustrative contour lines can be superposed on the figure to suggest a possible form for the variation of V_f over some range of the dimensionless parameters. Obviously, more research must be conducted to understand the front dynamics in these flows.

1.4.4 Overall regime classification

In this section, we aim to assemble our quantitative findings of the two main flow regimes at long times in our experiments: the unstable flow, for which the two fluids mix due to the presence of instabilities and the stable flow, for which the two fluids remain segregated over the timescale of our interest. It might be *a priori* expected that the two flow regimes must be described by two dimensionless parameters of the flow, namely the modified Reynolds number and the densimetric Froude number.

To provide an overall perspective of the various flow regimes and where they occur, Fig. 1.12a presents the classification of our flows for the full range of experiments. We observe that the

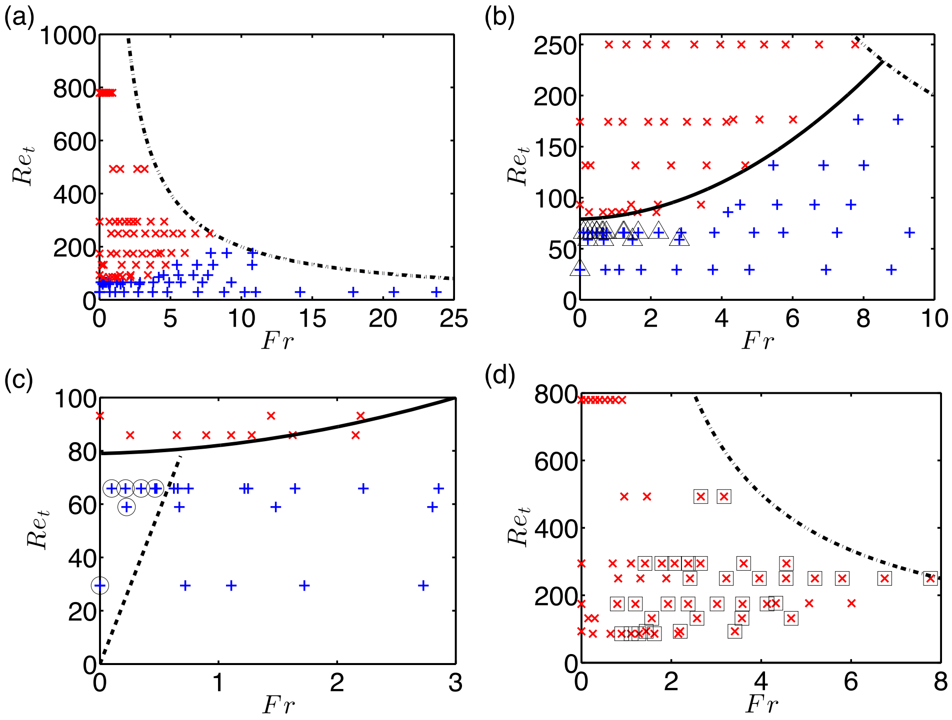

FIGURE 1.12 – Classification of our results for the full range of experiments: (a) Data points indicated by + are stable and by × are inertial. The dashed-dotted line curve is only illustrative and shows an estimate for the turbulent shear flow transition, roughly based on $Re \approx 2000$ (119). (b) The same as subfigure a (zoomed in). The thick line shows the leading order approximation for the transition from stable to unstable flow regimes ($Re_t|_{Critical} = 79 + Fr + 2Fr^2$). The flows with decaying helical waves are marked by superposed triangles. (c) The same as subfigure a (zoomed in). Stable, sustained-back-flows are marked by the superposed circles. The oblique dashed line shows $\chi = 2Re_t/Fr \approx 230$. The thick line is the same as in subfigure b. (d) The same as subfigure a (zoomed in) but showing unstable flows only. Here the flows with a front detachment are marked by squares.

data points belonging to stable and unstable flows are clearly separated. The data points are more concentrated close to the transition region between stable and unstable flows, where more experiments were purposefully performed to delineate the transition boundary. In this figure, three regions are distinguishable in the plane of Re_t and Fr. First, for smaller Fr and larger Re_t, the displacement flow is unstable due to the presence of strong buoyancy. On the other hand, for smaller Re_t and larger Fr, the displacement flow is stable. The third region is the one above the dashed-dotted line curve, for which the imposed flow itself is assumed turbulent: $Re > 2000$.

Let us now discuss the transition between stable and unstable flows in Fig. 1.12b. For $Fr = 0$, Debacq *et al.* (41) have quantified that $Re_t|_{Critical} \approx 79$ marks the transition from stable to unstable flows. As also mentioned earlier, we argue that for $Fr \neq 0$, this transition should be a function of Fr. Indeed, a coarse analysis can estimate $Re_t|_{Critical} = f(Fr) \approx f(0) +$

$f'(0)Fr + f''(0)Fr^2/2 + ...$, where we experimentally find $f'(0) = f''(0)/4 = 1$ and we take $f(0) = 79$ from (41), as a leading order approximation to the stable–unstable transition. This has been superposed on as a thick line on Fig. 1.12b.

Within the stable flows in Fig. 1.12b, there are flows (marked by superposed triangles) where helical waves are observed at the interface. These waves are usually observed at shorter times. However, they are unable to completely mix the fluids and they decay progressively. As most of the experimental data with wavy interfaces are located close to the boundary to unstable flows, they may be also appropriately called transitionary displacement flows. Fig. 1.12b shows that this feature of the flow disappears at higher imposed flows (i.e. larger Fr), which may be justified by considering the general stabilizing effect of the imposed flow.

Fig. 1.12c shows the same data points as the ones in Fig. 1.12a, but the figure has been zoomed in for clearer visualization. Let us focus on the stable flows. These flows can be divided into two sub-regions (sub-regimes): the no-sustained-back-flow regime where there is no sustained upward motion of the light fluid above the gate valve against the mean imposed flow direction and the sustained-back-flow regime which is related to the buoyancy driven upward flow of the lighter fluid, i.e. against the mean imposed flow direction. These two regimes are different in that sustained-back-flows will be never completely displaced by the imposed flow. In Fig. 1.12c, the oblique dashed line shows the critical χ_s, obtained through the lubrication model, for the stationary interface flow state which identifies the transition between the two sub-regimes mentioned. As can be seen, the prediction of the lubrication model for the transition point is good.

Finally, Fig. 1.12d illustrates a secondary feature within the unstable flow regime, i.e. the flows with a front detachment, marked by squares. It is seen that the front detachment is generally absent in zero and small imposed flow velocities and in very large density differences.

1.5 Conclusions

We have experimentally investigated miscible displacement flows in a vertical pipe. The fluids were Newtonian, with a small density difference and nearly-identical viscosities. The problem analysis was reduced to two dimensionless parameters, i.e. the modified Reynolds number (Re_t) and the densimetric Froude number (Fr), for which our experiments covered a wide range.

We have identified two main flow regimes as stable and unstable displacement flows. The transition between these two regimes is quantified by $Re_t|_{Critical}$ as a function of Fr. Displacement flows that satisfy the condition of $Re_t|_{Critical} < 79 + Fr + 2Fr^2$ are stable and otherwise they are unstable. This implies that increasing the mean imposed flow (or increasing Fr) stabilizes the displacement flow for certain ranges of the dimensionless groups. Most of the focus of the paper has been on the stable flow regime, which is, of course, easier to analyse. The two fluids in the stable regime are segregated and there is a visible interface between them. In this regime, the displacing fluid invades the displaced one in a locally axisymmetric way in the middle of the pipe. The unstable displacement flows, on the other hand, are associated with instabilities, mixing, and diffusion.

Within the stable flow regime, the flows can be phenomenologically divided into sustained-back-flows and no-sustained-back-flows. In the former sub-regime, found at higher ratios of buoyancy to viscous stresses, the displaced fluid is able to continuously move upward above the gate valve and against the direction of the mean imposed flow. In the latter sub-regime, the buoyancy is not sufficiently strong to induce a sustained movement of the displaced fluid above the gate valve. The transition between these two regimes occurs at a marginal stationary interface flow state, which corresponds to the critical buoyancy number $\chi_s \approx 230$, well predicted by the lubrication model.

There exist interesting patterns within the unstable flow regime, one of which is the front detachment phenomena associated with the cutting of the front from the bulk displacing layer. This pattern had been observed computationally before, but never experimentally in 3D. We have delineated the region of the existence of the phenomena in the plane of Re_t versus Fr.

Finally, front velocities of the penetrating displacing fluid have been also analysed. For the stable flow regime, the lubrication model developed also delivers the front velocity at longer times V_f^{Lub}, when viscous forces dominate inertial forces in balancing buoyancy. A combination of a velocity scale formulation for the initial inertial acceleration and V_f^{Lub} provides a predictive model for $V_f(t)$, which agrees reasonably with the experimental data (although at long times the values of V_f from experiments are generally slightly smaller than their model counterparts). For the unstable regime, it seems that the front velocities at longer times are scattered in the plane of Re_t and Fr, where reasonable trends versus these two parameters may be distinguished. However, due to the complexity of the flow problem, we leave the modelling of the front velocities of these flows for a future work.

Chapitre 2

Displacement flows in periodically moving pipe: understanding multiphase flows hosted in oscillating geometry

Résumé

Dans le présent travail, nous étudions expérimentalement les écoulements de déplacement de deux fluides miscibles Newtoniens à l'intérieur d'un long tuyau mobile vertical tout en comparant les résultats avec les écoulements de déplacement correspondants d'un tuyau fixe. En mouvement, le tuyau oscille lentement comme un pendule inversé. Les deux fluides ont une faible différence de densité et une viscosité presque identique. Le fluide de déplacement le plus dense est placé au-dessus du fluide déplacé. Globalement, le flux de déplacement dans la conduite en mouvement est au moins contrôlé par trois groupes sans dimension, à savoir le nombre de Reynolds, le nombre de Froude densimétrique et le nombre de Rossby. Des images expérimentales du front pénétrant du fluide lourd qui se déplace dans le fluide léger ont été analysées pour une large gamme de ces groupes sans dimension. On observe en particulier trois régimes d'écoulement différents pour les écoulements de déplacement dans une conduite en mouvement : un flux stable non diffusif (pour $Re/Ro \lesssim O\left(10^2\right)$ & $Re/Fr^2 < 35$), un flux stable-diffusif (pour $Re/Ro \gtrsim O\left(10^2\right)$ & $Re/Fr^2 < 35$) et un flux instable diffusif (pour $Re/Fr^2 > 35$). De plus, les vitesses avant de pénétration ainsi que les coefficients de diffusion macroscopiques ont été quantifiés. Les résultats montrent clairement qu'en fonction de la valeur de la différence de densité et de la vitesse moyenne d'écoulement de déplacement imposé, le mouvement géométrique peut avoir des effets différents et même opposés, par exemple une augmentation ou une diminution légère de la vitesse avant. Le mouvement du tuyau semble également augmenter légèrement le coefficient de diffusion macroscopique. Bien que les résultats de cette étude puissent aider à comprendre les principaux effets associés à un mouvement de géométrie d'écoulement sur les écoulements de déplacement, ils peuvent être d'une grande importance pour les applications industrielles et pour le développement de théories pertinentes de la mécanique des fluides.

Abstract

In the present work, we experimentally study displacement flows of two Newtonian, miscible fluids in a long, vertical moving pipe while comparing the results with the corresponding displacement flows in a stationary pipe. When in motion, the pipe slowly oscillates like an inverted pendulum. The two fluids have a small density difference and a nearly-identical viscosity. The denser displacing fluid is placed above the displaced fluid. Overall, the buoyant displacement flows in the moving pipe is at least controlled by three dimensionless groups, namely the Reynolds number, the densimetric Froude number, and the Rossby number. Experimental images of the penetrating front of the heavy displacing fluid into the light displaced one have been analysed for a wide range of these dimensionless groups. In particular, three different flow regimes are observed for displacement flows in a moving pipe: a stable flow that is non-diffusive (for $Re/Ro \lesssim O\left(10^2\right)$ & $Re/Fr^2 < 35$), a stable-diffusive flow (for $Re/Ro \gtrsim O\left(10^2\right)$ & $Re/Fr^2 < 35$) and an unstable-diffusive flow (for $Re/Fr^2 > 35$). In addition, penetration front velocities, as well as macroscopic diffusion coefficients, have been quantified. The results show in details that depending on the value of density difference and the mean imposed displacement flow velocity, the geometrical movement can have different and even opposite effects, e.g. slightly increase or decrease the front velocity. The pipe motion seems to also slightly increase the macroscopic diffusion coefficient. While the findings of this study can help to understand the leading order effects associated with a flow geometry movement on displacement flows, they can be of great importance for industrial applications and for development of relevant fluid mechanics theories.

2.1 Introduction

In simple words, displacement flows occur when a fluid is imposed to push another fluid of different properties in a flow geometry that is usually confined. Displacement fluid flows are among the most widespread phenomena in nature (6; 102), as well as in industry, e.g. in oil and gas industry (2; 120) and other applications (103). In the present work, we experimentally study high-Péclet-number miscible displacement flows of Newtonian fluids in a long, vertical, moving pipe. The two fluids have the same viscosity. The density difference between the two fluids is small so that the Boussinesq approximation is applicable. However, as the heavy fluid is placed on the top of the light fluid, buoyancy is still significant in driving fluid flow motion. At the same time, there is a downward laminar imposed flow, with a mean velocity, $\hat{V}_0$ [1]. In addition, during the displacement flow process, the test pipe slowly oscillates like an inverted pendulum (see Fig. 2.1). Buoyant displacement flows in stationary geometries have been studied in depth recently (see e.g. (16; 18; 121)) but the literature on buoyant displacement flows in moving geometries is almost non-existent. The focus of our study is to draw a comparison between buoyant miscible displacement flows in moving and stationary pipes, through studying a number of key and leading order features of these flows.

The literature of exchange flows is very relevant to work. Our displacement flows approach their exchange flow limit when the imposed displacement flow velocity becomes zero. In that case, the only driving force in the flow is buoyancy, which is dissipated by either viscosity or inertia. Debacq *et al.* (40; 41), Seon *et al.* (42; 43; 44; 45; 46), and Znaien *et al.* (47) have experimentally studied buoyant miscible exchange flows in vertical and inclined pipes and they have found/classified various flow regimes that may exist in an exchange flow configuration, e.g. inertial, viscous, diffusive, etc. Two fluid flow features have been of focus and interest in their works: the interpenetrating front velocity ($\hat{V}_f$) and the macroscopic diffusion coefficient ($\hat{D}_M$). Debacq *et al.* (40; 41) have shown that the latter can characterize diffusive flows, for which the extent of the axial diffusion is much larger than the molecular diffusivity. The former has been found helpful in recognizing whether the exchange flow is viscous or inertial, while they have found that $\hat{V}_f$ and $\hat{D}_M$ are functions of density ratios, fluid viscosities, and pipe diameter. Extending the same approach, Seon *et al.* (42; 43; 44; 45; 46) have studied buoyant miscible exchange flows in various pipe inclinations from horizontal to vertical and they have quantified the dependency of $\hat{V}_f$ and $\hat{D}_M$ on the flow parameters, including the inclination angle. Seon *et al.* (42) and Debacq *et al.* (41) have also looked into the transition between diffusive and non-diffusive flows as a function of the flow governing parameters.

Taghavi *et al.* (16; 15; 85; 86), Alba *et al.* (18) and more recently Amiri *et al.* (121) studied buoyant miscible displacement flows in nearly-horizontal, inclined and strictly vertical ducts, respectively. In comparison with an exchange flow, a mean flow velocity was imposed to the system; thus, the focus of their studies was on quantifying the effect of $\hat{V}_0$ on the flow. Using a combination of detailed experimental, computational and analytical approaches, Taghavi *et al.* (16) classified viscous and inertial regimes in near-horizontal inclinations. Their work enabled predictions to the penetrating displacement front velocity in the viscous regime using lubrication-type analytical models. For the inertial regime, they proposed experimental correlations to relate $\hat{V}_f$ to the flow governing parameters. Experimental study of Alba *et al.* (18) in inclined pipes showed the existence of a diffusive regime, in addition to viscous and inertial regimes, which they quantified and for which they proposed correlations to pre-

---

[1] In this paper we adopt the convention of denoting dimensional quantities with the ˆ symbol and dimensionless quantities without.

dict $\hat{D}_M$. Relevant to our work, there is also a large body of computational works studying buoyancy driven and displacement flows, e.g. (19; 71; 72; 105; 122). Buoyant displacement flows with a moderate viscosity ratio have been also studied (88). More structured (viscous-like) miscible displacement flows have been also studied in depth for uniform geometry flows, e.g. (81; 80; 106; 107; 108) and more recently for non-uniform geometry flows (22). Displacement flow instabilities in Hele-Shaw cells have been also the subject of numerous studies, e.g. (123; 124). The interested reader is also referred to a recent relevant review on instabilities of viscosity-stratified flows (125).

At zero density difference, axial diffusive spreading of displacement flows may be compared with Taylor dispersion for turbulent flows (101). Through modifying the Taylor's analysis, Tichacek *et al.* (126) demonstrated that as the flow approaches the laminar regime, the axial diffusive spreading significantly improves. Alba *et al.* (18) showed that the presence of buoyancy significantly modifies the axial diffusive spreading and $\hat{D}_M$ interestingly exceeds the corresponding Taylor dispersion coefficient, by up to an order of magnitude.

We have found only very few studies in the open literature which can be directly relevant to displacement flows with moving geometry. These are more application-oriented works, relevant to processes in oil and gas well cementing or floating production storage and offloading (FPSO) applications. For example, Savery *et al.* (93) used a mixed 2D and 3D computational approach to study the effect of a casing motion in displacement flows in oil well completion applications. Carrasco-Tejaand and Frigaard (52; 53) relied on a lubrication type-model to analytically study Newtonian and non-Newtonian fluid displacements. Their focus was on a horizontal narrow eccentric annuli geometry where the inner cylinder moves. Their scenario of consideration was a viscous flow at the limit of large buoyancy. Assima *et al.* (54) studied the emulation of gas-liquid flow in moving packed beds, relevant to offshore floating applications, where it has been shown that flow patterns, scalar transport in the liquid and maldistribution of the liquid across the cylindrical porous-medium vessel were sensitive in different manners to the type of perturbing degree of freedom. While our study can provide fundamental understanding about the displacement flows that occur in the industrial applications mentioned, it adds a new dimension to the body of the sparse previous works.

The novelty of the current investigation is that we study experimentally buoyant displacement flows in a moving pipe for the first time, and we quantify some of the leading order behaviours of the flow when the motion is imposed. The term "inverted pendulum-like motion" implies that the center of mass of the pipe lies above its pivot point. This flow geometry motion has been chosen due to its importance and simplicity as a classic problem in dynamics, which involves a single degree of freedom by affixing the pipe to an axis of rotation. Throughout this paper, unless otherwise stated, by motion we mean the inverted pendulum-like motion of the experimental pipe.

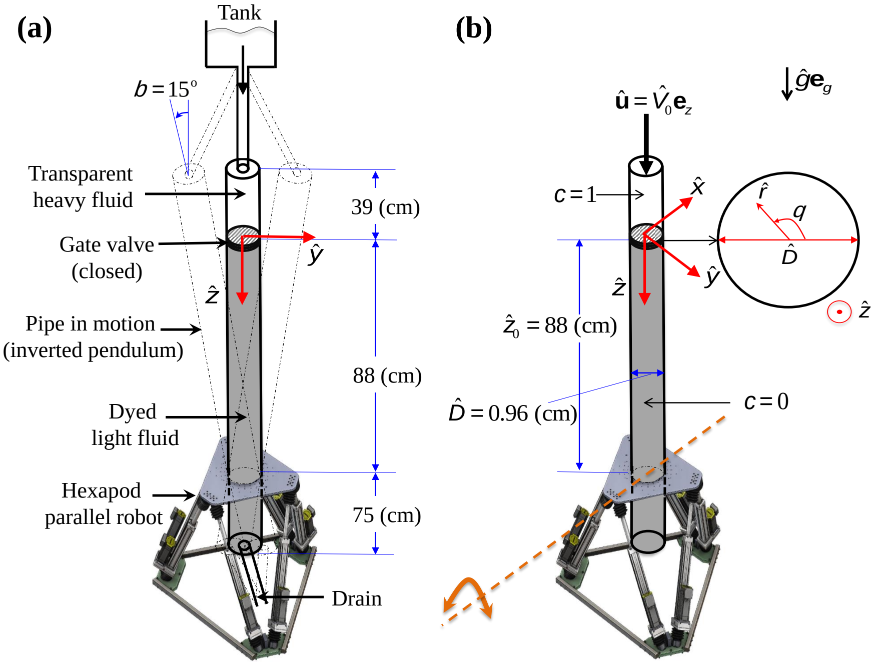

FIGURE 2.1 – Schematic view of the experimental displacement flow setup: (a) The pipe in motion and (b) Coordinates, dimensions, and other details.

The paper proceeds as follows. Section 2.2 discusses our displacement flows from a modeling perspective. Section 2.3 describes the experimental setup and procedures. Experimental results are presented in §2.4 where various flow regimes are discussed qualitatively and quantitatively. The focus will be on providing understanding about the effect of the pipe motion on buoyant displacement flows. Section 2.5 concludes the paper with a brief summary of the main findings.

2.2 Problem setting

We consider a situation where a heavy fluid (fluid H) displaces a light fluid (fluid L) along a long, vertical pipe which is in motion like an inverted pendulum, as illustrated in Fig. 2.1. We focus on small oscillatory motion frequencies, $\hat{f} = 0.2$ (Hz)[2], and a small maximum oscillation amplitude ($\hat{\mathscr{A}}$), i.e. 15 (°) with respect to vertical. The pipe has a diameter $\hat{D}$. The mean imposed displacement flow velocity ($\hat{V}_0$) is in the downhill direction. This imposed flow is laminar. The fluids have nearly the same dynamic ($\hat{\mu}$) or kinematic ($\hat{\nu} = \hat{\mu}/\hat{\bar{\rho}}$) viscosity, and they are miscible. The fluids also have slightly different densities. The length of the pipe is much larger than its diameter so that the aspect ratio satisfies $\delta^{-1} = \frac{\hat{L}}{\hat{D}} \gg 1$. As Fig. 2.1 shows, the two fluids are initially separated by a gate valve so that when it is opened the initial interface is transverse to the pipe axis and it is located away from both pipe ends.

---

[2] We have also carried out a wide range of experiments at $\hat{f} = 0.02$, 0.05 and 0.1 (Hz) to provide a detailed regime classification presented in Fig. 2.4.

TABLE 2.1 – Range of some of the dimensionless parameters used in our experiments for non-zero values of $\hat{V}_0$. D_m is taken to be $\sim 2 \times 10^{-9}$ (m^2/s).

Parameter	**Name**	**Definition**	**Range**
At	Atwood number	$\frac{\hat{\rho}_H - \hat{\rho}_L}{\hat{\rho}_H + \hat{\rho}_L}$	$10^{-4} - 7 \times 10^{-2}$
Re	Reynolds number	$\frac{\hat{V}_0 \hat{D}}{\hat{\nu}}$	$20 - 756$
Fr	Densimetric Froude number	$\frac{\hat{V}_0}{\sqrt{At \hat{g} \hat{D}}}$	$0.1 - 24$
Ro	Rossby number	$\frac{\hat{V}_0}{\hat{\omega}_0 \hat{D}}$	$0.17 - 65$
Pe	Péclet number	$\frac{\hat{V}_0 \hat{D}}{\hat{D}_m}$	$10.1 \times 10^3 - 378.2 \times 10^3$

Although this paper is exclusively about experimental results, it seems necessary to describe the equations of motion from a modelling perspective. A natural formulation of our miscible displacement flows involves a concentration–diffusion equation which must be coupled to the Navier–Stokes equations in a pipe-attached moving frame of reference. The change between pure heavy and light fluids can be modelled via a scalar concentration, c. We render the Navier–Stokes equations dimensionless using $\hat{D}$ as length scale, $\hat{V}_0$ as velocity scale, $\hat{\omega}_0 = 2\pi\hat{f}$ as angular velocity scale. Subtracting a mean static pressure gradient before scaling the reduced pressure, we arrive at

$$(1\text{-}\phi At)\,(\mathbf{u}_t + \mathbf{u}.\nabla\mathbf{u}) = -\nabla p + \frac{1}{Re}\nabla^2\mathbf{u} - \frac{\phi\mathbf{e}_g}{Fr^2} - \frac{1}{\delta Ro^2}\,(1\text{-}\phi At)\,\Omega\times(\Omega\times\Re) - \frac{2}{Ro}\,(1\text{-}\phi At)\,\Omega\times\mathbf{u}, \tag{2.1}$$

$$\nabla.\mathbf{u} = 0, \tag{2.2}$$

$$c_t + \mathbf{u}.\nabla c = \frac{1}{Pe}\nabla^2 c. \tag{2.3}$$

Here, the left-hand-side (LHS) shows the inertial acceleration terms, and on the right-hand-side (RHS), the first term is the pressure gradient, the second term is the viscous dissipative stress, the third term is buoyancy stress, the fourth term is centrifugal body stress, and the fifth term is the Coriolis stress. Also, in Cartesian coordinates, $\mathbf{e}_g = (0, -\sin\beta, \cos\beta)$, where β is the time-dependent pipe inclination angle (with respect to vertical), with a complicated functionality on $\mathscr{A}$, Ro and t, Ω is a function of Ro and t, and $\Re = (\delta x, \delta y, Z_0 - \delta z)$ with a fixed $Z_0 = \hat{z}_0/\hat{L} \approx 0.44$. The function $\phi(c) = 1 - 2c$ interpolates linearly between 1 and -1 for $c \in [0, 1]$, for displaced and displacing fluids, respectively. The five dimensionless parameters appearing in equation (2.1) are the angle of inclination from vertical (depending on time, Ro and $\mathscr{A}$), the Atwood number, At, the Reynolds number, Re, the densimetric Froude number, Fr, and the Rossby number, Ro. A sixth dimensionless group also appears in equation (2.3), the Péclet number. Five of the most relevant dimensionless parameters of our displacement flows are defined in Table 2.1.

There are a few assumptions that can simplify the complex problem. First, the Péclet number in our displacement flows is very large, implying that the fluids mix only due to hydrodynamic effects. Second, considering our interest in small density differences, for which $max(At) = 7\times 10^{-2}$, $At \to 0$ on the LHS of equation (2.1) provides a reasonable approximation. However, it must be noted that the force of buoyancy is still significant on the RHS. Finally, considering that δ, $\mathscr{A}$, and Z_0 are constant parameters, possible flow regimes in the simplified displacement problem may be described by three dimensionless groups only, i.e. Re, Fr & Ro, assuming $Pe \to \infty$ & $At \to 0$. Note that Re, Fr & Ro are constant parameters during each experiment. Table 2.1 shows that our experiments cover a wide range of these three parameters.

2.3 Experimental setup

Our experimental study was performed using a 202 (cm) long, vertical pipe, with an inner diameter of 0.96 (cm). The pipe was transparent so the visualization of the displacement flow process was possible. A gate valve located at 39 (cm), from the top end, was included in the system. The displacement flow setup was mounted on a hexapod robot, which is a motion simulator that has six degrees of freedom (see the schematic of the hexapod in Fig. 2.1). Based on the principle of the Stewart platform, the hexapod includes a fixed platform and a mobile platform, which are linked together by six actuators (hydraulic jacks). The actuators are mounted in pairs on the fixed platform and cross over to three mounting points on the mobile platform. A software was used to slowly move the mobile platform. The displacement setup placed on the platform could be moved to experience movement similar to a large inverted pendulum. Initially, the lower part of the pipe was filled with a less dense fluid coloured with a small amount of ink for visualization. The upper part of the pipe, above the gate valve, was filled with a slightly denser fluid. Salt was used as the weighting agent. To avoid pump disturbances, the displacing upper fluid was fed by gravity from a large elevated tank. The flow rate was controlled by a needle valve and it was measured by two rotameters, located downstream of the pipe. For extremely small mean imposed flow velocities, the flow rate was calculated by a graduated cylinder that measured the amount of the fluid exiting the pipe. In a typical experiment, the gate valve was opened and, at the same, the hexapod started to move the pipe from its completely vertical position. The displacement flow images were recorded using a high-speed camera (Blaser acA2040 model), covering 80 (cm) below the gate valve. Since the camera was mounted on the setup to move with it, reasonably clear images were obtained in a moving frame of reference. Note that the plane $(\hat{y}, \hat{z})$ where the images were obtained is perpendicular to the (virtual) axis of rotation of the pipe. To increase the quality of images, the pipe was back-lit using Light-Emitting Diode (LED) strips. In addition, to improve light homogeneity, a diffusive layer was placed between the pipe and the LED strips. Light absorption calibrations were performed in a usual fashion. The experimental images were then analysed to characterize different aspects of displacement flows.

Before running displacement flow experiments in a moving pipe, a number of experiments were performed in a stationary pipe and the results were compared with the available data in the literature (18; 41; 46). In the case of exchange flows, front velocities and macroscopic diffusions were successfully compared with the studies of (41; 46). For displacement flows, comparisons were made and reasonable agreement was found with the study of (18). Even a number of exchange flow tests (at $At = 10^{-2}$) were conducted in an inclined pipe and the results were compared with those of (46) in a pipe with a slightly different diameter, showing a difference of $\sim 7\%$ (on average), for various inclinations up to 15 (°) from vertical. Some experiments were also performed for density-stable displacement configurations and reasonable agreement was seen with the literature data (89). To the best of our knowledge, there is no literature on buoyant displacement flows in moving pipes; thus, no validation/benchmarking was possible in that case.

2.4 Results

In this section, we present our experimental results. We first begin with explaining the main features of our displacement flows. We then describe a method to approximate the real concentration profile to better analyse displacement flows. Afterward, we discuss two important parameters which characterize the flow, namely the displacing front velocity and the macroscopic diffusion coefficient.

2.4.1 Displacement flow main features

Fig. 2.2 compares displacement flows at a small density difference in moving and stationary pipes. Since the experimental snapshots are calibrated, the colours in this figure vary between 0 (dark displaced fluid) and 1 (transparent displacing fluid). The mean imposed flow velocities are relatively small for the cases shown here. Note that the field of view is only below the gate valve and that the images are in a moving frame of reference. Various observations can be made. First of all, with the exception of the two panels for $\hat{V}_0 = 0$, the displacement flows seem more or less stable. In the stationary and moving pipes, a finger of the displacing fluid seems to advance in the displaced fluid. In the stationary case, a clean interface between the two fluids is formed. However, for displacements in the moving pipe, although the overall flow is not unstable, the displacing front seems to diffuse; the interface, especially at the front, is not sharp anymore. Let us call these flows *stable* and *stable-diffusive* flows for stationary and moving pipe flows, respectively.

The case of $\hat{V}_0 = 0$ in Fig. 2.2 may deserve a separate attention. Firstly, when the pipe is stationary, the heavy fluid forms a finger into the light fluid and helical waves appear at the interface. As the penetration deepens further, these waves progressively decay and they eventually disappear. However, for the moving pipe flow, the heavy fluid does not significantly

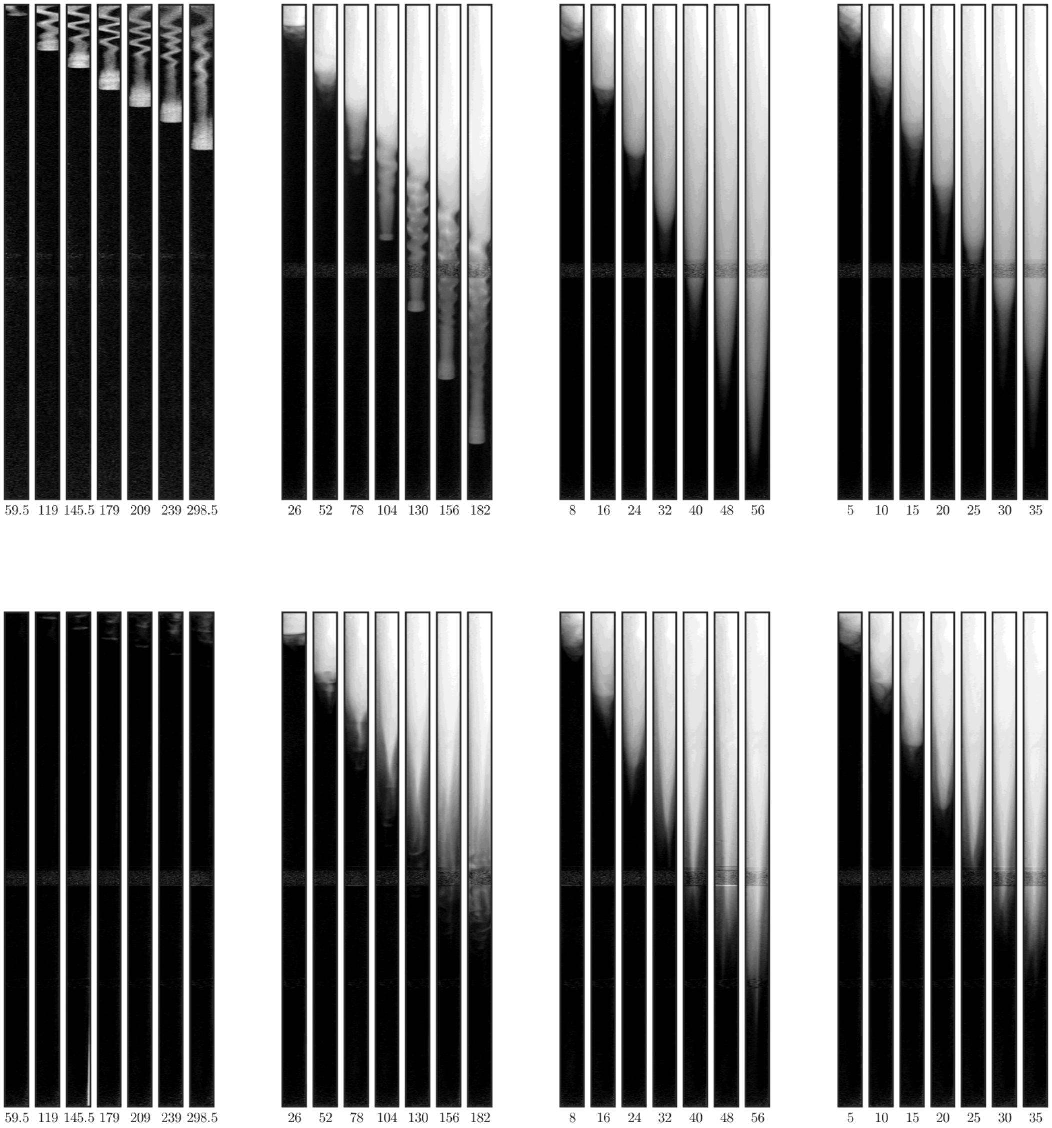

FIGURE 2.2 – Sequence of experimental images for a fixed Atwood number ($At = 10^{-4}$) for displacement flows in a stationary pipe (top row) and a moving pipe (bottom row). From left to right, $\hat{V}_0 = 0$, 2, 8, 12 (mm/s) in each panel. The experimental times (in seconds) are indicated below each snapshot. The field of view in each snapshot is 8×805 (mm^2), located 24 (mm) below the gate valve. In this and the other figures, the camera images shown have an offset of a few pixels with respect to the pipe center-line.

penetrate into the light fluid. In fact, the flow is far from stable and the interpenetration is due to the convective diffusive-like expansion of the mixed zone close to the gate valve. Therefore, the front velocity of the penetrating heavy fluid in a moving pipe is much lower than that in a stationary one. It seems that the pipe movement can more significantly affect the flow of small density difference when the mean imposed flow is zero (i.e. the exchange flow limit).

Fig. 2.3 shows the experimental image sequences for a fixed mean imposed flow velocity, i.e.

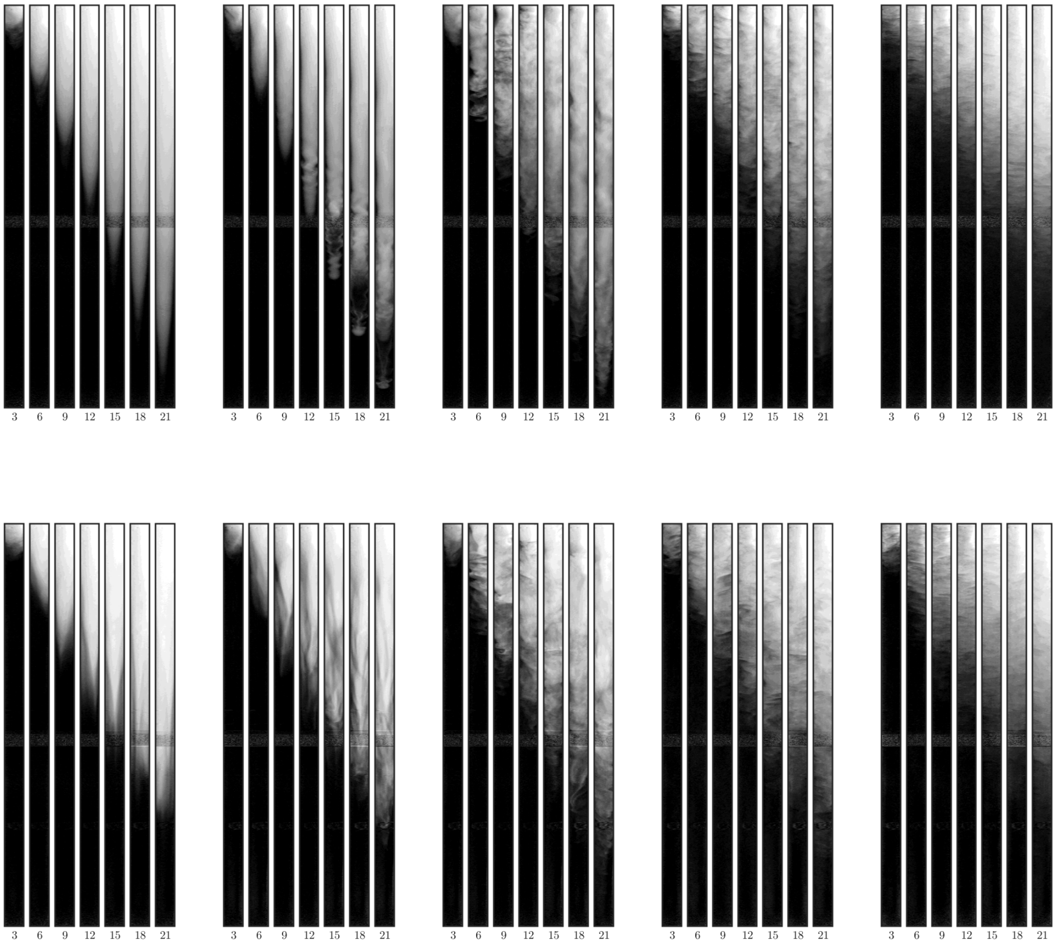

FIGURE 2.3 – Experimental image sequences for $\hat{V}_0 = 21\pm2$ (mm/s) and $At = 10^{-4}, 10^{-3}, 3.5\times 10^{-3}, 10^{-2}, 7\times 10^{-2}$ from left to right, for a stationary pipe (top row) and a moving pipe (bottom row). The experimental times (in seconds) are indicated below each snapshot. The field of view in each snapshot is 8×805 (mm^2), located 24 (mm) below the gate valve.

$\hat{V}_0 = 21 \pm 2$ (mm/s), and different density differences. The top row in this figure corresponds to displacement flows in a stationary pipe. By increasing the Atwood number of each panel from left to right, it can be observed that the flow transitions from a stable flow regime to an unstable flow regime with instabilities and diffusive mixing. In addition, by increasing the Atwood number, the quality of the transverse mixing is increased. In the bottom row, more or less the same qualitative behaviour is observed, although the quality of mixing seems to be at least visually different. Displacements at higher imposed flows show more or less the same behaviour as observed in Fig. 2.3 (the results are not shown for brevity). In order to quantify the effect of the geometry motion on the displacement flows, it seems necessary to further analyse the experimental images and proceed beyond qualitative comparisons of these images.

In terms of regime classification, so far, three main regimes can be distinguished for displacement flows in a moving pipe: stable, stable-diffusive and unstable-diffusive flow regimes. The latter is related to displacement flows which are unstable, mainly due to buoyancy. The stable flow regime is associated with a nearly-stable, non-diffusive finger of the displacing fluid into the displaced one. The stable-diffusive flow regime is associated with displacement flows where the overall flow is stable or does not seem unstable but the displacing front becomes mixed with the displaced fluid as time progresses, mainly due to the pipe movement. As the bottom row in Fig. 2.2 illustrates, in stable-diffusive flows, there exist multiple, diffusive fingers of the displacing fluid as opposed to a single, non-diffusive finger in stable flows (e.g. compare bottom and top rows in Fig. 2.2). Fig. 2.4 classifies these three flow regimes in the plane of Re/Ro and Re/Fr^2, which we have obtained after several attempts of various combinations of the dimensionless groups. While Re/Ro can be simplified as the ratio of Coriolis to viscous stresses, Re/Fr^2 shows the ratio of buoyancy to viscous stresses. Interestingly, these two dimensionless groups appear explicitly in equation (2.1) if the two sides are multiplied by Re. The transition boundaries are crudely marked on this figure using a horizontal dash line ($Re/Ro = 70$) and a vertical dashed line ($Re/Fr^2 = 35$). Independent of the fast or slow motion of the pipe, unstable-diffusive flows are observed when $Re/Fr^2 > 35$, where the flow is dominated by buoyancy. On the other hand, stable flows are observed at $Re/Fr^2 < 35$ & $Re/Ro < 70$, when the flow is mainly dominated by viscous forces. Finally, stable-diffusive flows are observed when $Re/Fr^2 < 35$ & $Re/Ro > 70$, where buoyancy stresses are weak compared to viscous stresses but the pipe motion affects the flow, leading to diffusive effects near the displacing front. Two points must be noted here. First, although we show that Coriolis stresses induced by the movement have significant effects on the flow, centrifugal stresses also induced by the movement (quantified through $1/Ro^2$) may be expected to affect the flow as well. However, in order to uncover these details more research must be conducted on our displacement flows. Second, the value of $Re/Ro = 70$, is a rough estimate for the transition boundary. In fact, based on our available experimental data we can be only certain that the transition is somewhere between $Re/Ro = 28$ and $Re/Ro = 116$, for which we have proposed the mean value, approximately. In other words $Re/Ro \approx O\left(10^2\right)$ marks the transition boundary.

It is worth mentioning that the important dimensionless groups for our regime classification, i.e. Re/Ro and Re/Fr^2, can be simplified as $\frac{\hat{\omega}_0\hat{D}^2}{\hat{\nu}}$ and $\frac{At\hat{g}\hat{D}^2}{\hat{\nu}\hat{V}_0}$, respectively. The former ratio shows the ratio between Coriolis and shear stresses, which can be as well written as the inverse of the Ekman number (Ek), which is a relevant dimensionless parameter in rotating flows. On the other hand, $\frac{At\hat{g}\hat{D}^2}{\hat{\nu}\hat{V}_0}$ is the ratio between the characteristic viscous velocity driven by buoyancy ($At\hat{g}\hat{D}^2/\hat{\nu}$) and the characteristic imposed velocity ($\hat{V}_0$).

Let us finish this section with an example of another important effect of the pipe motion on displacement flows. Our experiments for displacements in a stationary pipe reveal that the displacing front advances in the middle of the pipe so the frontal interface is more or less perpendicular to the pipe longitudinal axis. When the pipe is in motion, such depiction no

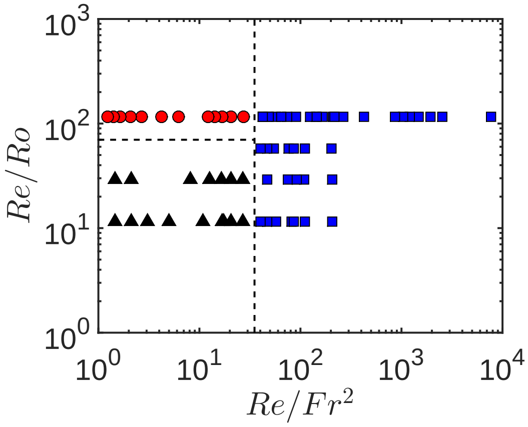

FIGURE 2.4 – Overall regime classification: stable flows (▲), stable-diffusive flows (●) and unstable-diffusive flows (■) for displacement flows in a moving pipe. The vertical dashed line shows $Re/Fr^2 = 35$ and the horizontal dashed line shows $Re/Ro = 70$.

longer holds. In this case, the pipe inclination slowly and continuously varies between $\beta = -15$ (°) and $\beta = 15$ (°). Thus, at least momentarily there are transverse buoyancy forces that may cause local segregation between the two fluids. The frontal region, in this case, has briefly the opportunity to slump so that the front interface is not anymore perpendicular to the pipe longitudinal axis. To show this feature clearly, Fig. 2.5 divulges a typical angle path generated by the hexapod as well as the corresponding displacement flow snapshots for a period of 30 seconds. The eye-guide lines superposed on the snapshots show the tendency of the frontal region to break the symmetry and slump locally. When the pipe is tilted, analogous to the Boycott effect, the heavy fluid is locally separated from the light fluid so that the sedimentation velocity increases (69) and the symmetry is broken for a short period of time. Fig. 2.5 shows another very interesting phenomenon, i.e. the break in the symmetry does not exactly follow the pipe angle generated a path with time; instead, it seems that the slumping effect has a delay with respect to the time when the pipe is at maximum inclination. We leave the in-depth study of this effect to future works.

2.4.2 Approximating 3D concentration profile

To understand our experimental displacement flows in details, one would need to have access to the spatial and temporal forms of pressure, velocity and concentration fields for the 3D pipe flow. This is of course not always possible due to technical/experimental measurement limitations as well as the difficulty of analysing a large amount of the associated data. Approximations to the concentration field are the most accessible and easy-to-treat forms of data that can be extracted by taking digital images and processing them. Table 2.2 shows a list of concentration profiles, providing useful information about the flow. In Cartesian coordinates, $C(x, y, z, t)$ is the real concentration profile, to which we do not have access through the 2D

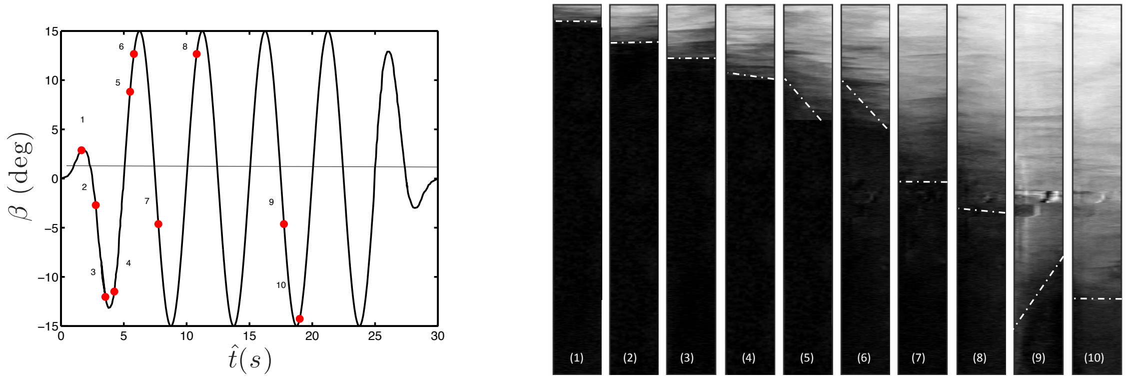

FIGURE 2.5 – The graph on the left is the path, in terms of the pipe angle, generated by the hexapod. The images are the sequence of experimental snapshots for displacement flows in a pipe in motion for the same experiments as shown in the graph on the left. The experimental parameters are $At = 10^{-2}$ and $\hat{V}_0 = 22$ (mm/s). From numbers 1 to 10, the experimental times are $\hat{t} = [1.5,\ 2.75,\ 3.5,\ 4.25,\ 5.5,\ 6.25,\ 8.75,\ 11.25,\ 17.75,\ 19]$ (s), respectively. The field of view in each snapshot is 8×805 (mm^2), located 24 (mm) below the gate valve. The dashed lines are to guide eye on the position and elongation of the displacement interface with respect to the pipe.

TABLE 2.2 – Different useful concentration profiles and their expressions in Cartesian coordinates.

Profile	**Function of**	**Expressions in Cartesian coordinates**
Real concentration	$C(x,y,z,t)$	-
Experimental concentration	$\bar{C}_x(y,z,t)$	$\frac{1}{2\sqrt{\left(\frac{1}{2}\right)^2-y^2}}\int_{-\sqrt{\left(\frac{1}{2}\right)^2-y^2}}^{+\sqrt{\left(\frac{1}{2}\right)^2-y^2}} C(x,y,z,t)dx$
Depth-averaged concentration	$\bar{\bar{C}}_{xy}(z,t)$	$\int_{-1/2}^{+1/2} \bar{C}_x\left(y,z,t\right)dy$
Length-averaged concentration	$\bar{\bar{\bar{C}}}_{xyz}\left(t\right)$	$\frac{1}{L}\int_0^L \bar{\bar{C}}_{xy}\left(z,t\right)dz$

images that our high-speed camera takes. $\bar{C}_x(y,z,t)$ is the experimental concentration profile, which is already averaged with respect to x when an image is taken. Using $\bar{C}_x(y,z,t)$, different concentration profiles can be constructed, the most useful forms of which are the approximated depth-average profile (used in the following sections) and the approximated length-averaged profile. Note that for a given time, the measured concentration fields consist of 2D matrices.

In this section, we aim to provide a simple method to construct a reasonable approximation of the concentration profile using the experimental concentration profile. This in return enables drawing comparisons between various concentration profiles in the 3D pipe and help extract more information about the effect of changing the flow parameters on displacement flows. To do so, we aim to establish a "pragmatic" analytical form of the concentration field in a cylindrical coordinate system using the experimental concentration profiles which are averaged profiles in a Cartesian coordinate system. Our effort involves some assumptions. Although there is certainly some asymmetry in the displacement flows when the pipe is in motion, we may assume that displacement flow asymmetry is not the dominant feature of the flow over a long period of time when the interface or the mixing zone is significantly elongated. This is mainly because the pipe moves in a symmetric way. Let us, therefore, assume that the concentration field is axisymmetric and neglect the dependence of the concentration on the angle in cylindrical coordinates. Therefore, we would like to find $C\left(r,z,t\right)$ that approximates $C(x,y,z,t)$ using the available experimental concentration profiles $\bar{C}_x(y,z,t)$. Furthermore, let us assume that a special polynomial form can approximate the estimated analytical concentration profiles as $C(x,y,z,t) \approx C\left(r,z,t\right) \approx \sum\limits_{i=0}^{K} a_i\left(z,t\right) r^i$ where $r = \sqrt{x^2+y^2}$ (relating the cylindrical radial distance to x and y in Cartesian coordinates), $a_i\left(z,t\right)$ are the unknown polynomial coefficients, and K is the degree of the polynomial. Replacing the proposed relation into the analytical expression of $\bar{C}_x(y,z,t)$ (given in Table 2.2) leads to

$$\bar{C}_x(y,z,t) \approx \frac{1}{2\sqrt{\left(\frac{1}{2}\right)^2 - y^2}} \int_{-\sqrt{\left(\frac{1}{2}\right)^2-y^2}}^{+\sqrt{\left(\frac{1}{2}\right)^2-y^2}} \sum_{i=0}^{K} a_i\left(z,t\right)\left(\sqrt{x^2+y^2}\right)^i dx \tag{2.4}$$

After the integration of the relation above, $\bar{C}_x(y,z,t)$ can be simplified in the following form:

$$\bar{C}_x(y,z,t) \approx \sum_{i=0}^{K} f_i(y) a_i\left(z,t\right), \tag{2.5}$$

where functions $f_i(y)$ can be calculated for a given K. An approximation to the LHS of equation (2.5) is available experimentally while the form of the RHS can be analytically calculated with $a_i\left(z,t\right)$ still being unknown. Thus, the equality of the RHS and the LHS can be used to estimate $a_i\left(z,t\right)$. Experimentally, for a given t, $\bar{C}_x(y,z,t)$ is a matrix of normalized concentrations with a usual dimension of 20×2018, corresponding to the number of image pixels in the transverse and longitudinal directions (for an image covering a field of view of $\sim 0.8 \times 80$ (cm^2)). Thus, the coefficients of a polynomial of up to degree 19 can be found using experimental images. However, we found that $K = 4$ was sufficient to approximate 3D concentration profiles and including the higher terms did not result in any significant effects. For example, for a wide range of parameters, our results show that 3D concentration profiles constructed using $K = 4$ and $K = 8$ were nearly identical. All the analytical calculations were performed using MAPLE and f_0, f_1, f_2, f_3 & f_4 are given in appendix B.

Now that the RHS side of relation (2.5) is calculated and the LHS is available experimentally, in order to find $a_i\left(z,t\right)$, for given t and z, we use a quasi-Newton algorithm to find the minimum of $\left\|\bar{C}_x\left(y,z,t\right) - \sum\limits_{i=0}^{4} f_i(y) a_i\left(z,t\right)\right\|$ in the pipe cross section. This allows the construction of

$$C\left(r,z,t\right) \approx \sum_{i=0}^{4} a_i\left(z,t\right) r^i, \tag{2.6}$$

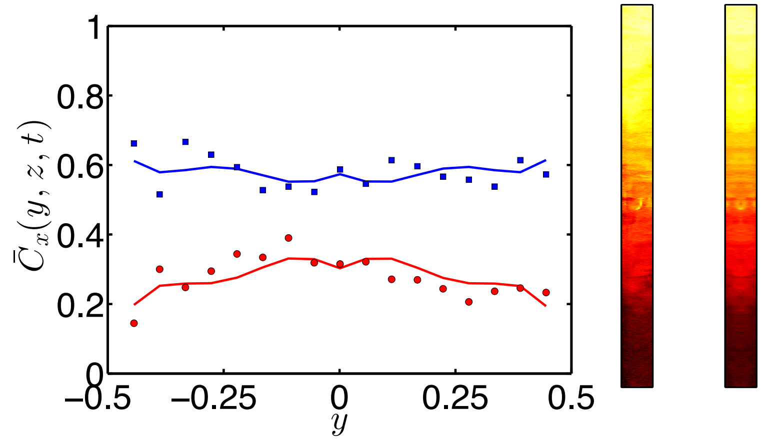

FIGURE 2.6 – The graph shows examples of the experimental concentration profiles in a moving pipe versus y for $t = 44$, at two z-locations: $z = 0.5$ (■) and $z = 0.74$ (●). The other experimental parameters are $At = 10^{-2}$ and $\hat{V}_0 = 22$ (mm/s). The lines are the results of $\sum_{i=0}^{4} f_i(y)a_i(z,t)$, where $a_i(z,t)$ have been found through the minimization approach explained in the text. The image in the middle shows the real experimental snapshot for a pipe dimensionless length of 84 at $t \approx 44$ and the image on the right is the computer reconstructed image using the method explained in the text.

where $a_i(z,t)$ are found for given z and t.

The graph in Fig. 2.6 shows an example where $a_i(z,t)$ have been found for two z-locations, through the minimization approach explained. This experiment was performed in a moving pipe. The comparison between equation (2.6) plotted as lines and the experimental data plotted as discrete points in the pipe transverse direction is reasonable (showing that the minimization approach works reasonably), although small differences are also observed mainly due to the asymmetry in experimental results. To test the capability of relation (2.6) to approximate the concentration field, two images are also given in Fig. 2.6. The image in the middle shows the experimental image when the displacement front reaches the end of the long pipe and the image on the right shows the reconstructed 2D image using the method explained. The contour plots are strikingly similar, confirming that the method explained is capable of reconstructing the leading order behaviours of the real concentration field. However, there exists a weak dependency of the concentration field on azimuthal coordinate (θ), which is not captured in the reconstructed concentration field and this is a drawback of our method. It should be mentioned that, of course, exchange or displacement flow experiments realized in a stationary pipe at a fixed tilt angle display significant segregation and azimuthal asymmetries, for which the approach presented is not appropriate to reconstruct 3D concentration profiles. However, for flows in a moving pipe that symmetrically oscillates at small inclination angles with respect to a virtual vertical line, after very long times and penetration distances azimuthal asymmetries

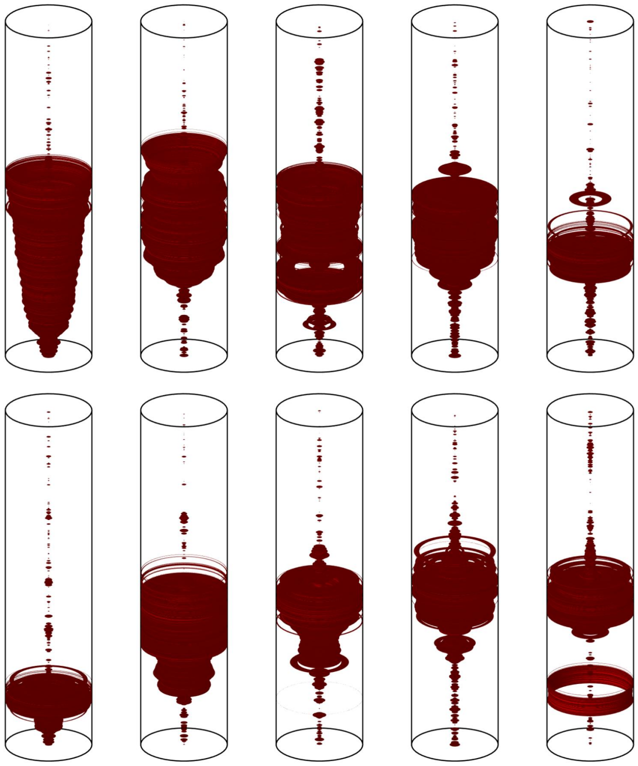

FIGURE 2.7 – Reconstructed 3D concentration iso-surfaces at $C(x, y, z, t) = 0.5$ for displacement flows in a stationary pipe (top row) and in moving pipe (bottom row). The value of $C = 0.5$ is chosen as a representative of the interface position between the two miscible fluids. The experimental parameters are $At = 10^{-4}, 10^{-3}, 3.5 \times 10^{-3}, 10^{-2}, 7 \times 10^{-2}$ form left to right and $\hat{V}_0 = 22 \pm 3$ (mm/s). The length of the pipe shown is 80 (cm) and the results are for when the displacement front reaches the end of pipe.

are not significant features of the flow. In fact, we may expect that the symmetrical motion of the geometry (with respect to a virtual vertical line) relaxes asymmetries within the pipe transverse direction, which justifies the use of the approach presented for the particular motion of our interest. Finally, for displacement flows in a stationary, strictly vertical pipe, the approach is also appropriate thanks to the inherent symmetry of the system with respect to the pipe center line.

Now let us apply the method just explained to reconstruct 3D images of the concentration field, as presented in Fig. 2.7. We can see that for a stationary pipe at the smallest At, the extent of the concentration iso-surface is a long finger that is extended between the displacing and displaced fluids. This represents a nearly stable flow. As the Atwood number increases the concentration iso-surface of $C = 0.5$ shrinks meaning that fluid mixing increases. In addition, the radial mixing also increases for larger At. When the pipe is at motion the concentration iso-surface changes. The change is more obvious for a low Atwood number flow: the fluids start to mix as the pipe moves. From the figure, it can be also concluded that the displacement is more efficient when the pipe is at motion. Fig. 2.7 also shows that while the concentration iso-surfaces are more concentrated in terms of their longitudinal extension, they have more variations and oscillations when the pipe is at motion. Many other observations can be also made, which we leave for brevity. We merely mention that the method presented in this section may pave the way to analyse, at low cost, interesting features of displacement flows for various flow parameters, including various geometrical movements.

2.4.3 Displacement front velocity

One of the most important features of displacement flows is the displacement front velocity ($\hat{V}_f$), which must be measured in a consistent way for displacement flows with & without mixing as well as with & without pipe motion. To achieve this, we estimate the velocity of the displacement front through the velocity of the depth-averaged concentration level at 0.1, which seems to be a good trade-off in terms of concentration signal-to-noise ratio, consistently found for all experiments in moving and stationary pipes. In order to explain this better, Fig. 2.8a shows an example of the evolution of the average concentration field with time and streamwise location. The front velocity of the penetrating heavy displacing fluid can be approximated by following the $\hat{z}$-location of a small $\bar{\bar{C}}_{xy}$ above the noise, e.g. $\bar{\bar{C}}_{xy} \approx 0.1$ to give $V_f \approx \frac{\hat{z}}{\hat{t}}\Big|_{\bar{\bar{C}}_{xy}=0.1}$. In fact $\bar{\bar{C}}_{xy} \approx 0.1$ provides an approximation to the real front pipe center-line velocity but it obviously underestimates it since $\bar{\bar{C}}_{xy}$ moves more slowly at 0.1 than at the center-line.

There is interesting information delivered by Fig. 2.8. Compared to the moving case, the depth-averaged concentration profiles at longer times have a sharper variation closer to the front in the stationary pipe. In other words, in the moving pipe case the mixing zone between the displacing and displaced fluids elongates further along the pipe. In fact, for a wide range of imposed flow velocities at $At = 10^{-2}$, we consistently observe this behaviour (results are not shown for brevity). The front velocity is accordingly also more oscillatory in a moving pipe (see Figs. 2.8c & d). In addition, it is seen that the front velocity for both displacement flow cases increases relatively quickly at short times and it reaches a mean final value, around which $\hat{V}_f$ oscillates irregularly with time.

To give a global vision of the front velocity variation for a wide range of density differences, Fig. 2.9 shows V_f versus time for 5 different At for a typical value of $\hat{V}_0$. Similar results were obtained for 5 different At and 6 different $\hat{V}_0$ (i.e., 23 ± 2 , 34 ± 1, 43 ± 1, 53 ± 2, 63 ± 2, 74 ± 1 (mm/s)). Both the front velocities and times have been made dimensionless. It can be seen that, first of all, by increasing At, V_f (i.e., the ratio of $\hat{V}_f$ to $\hat{V}_0$) slightly decreases in general, for both stationary and moving pipes. This effect is perhaps due to the establishment of stronger

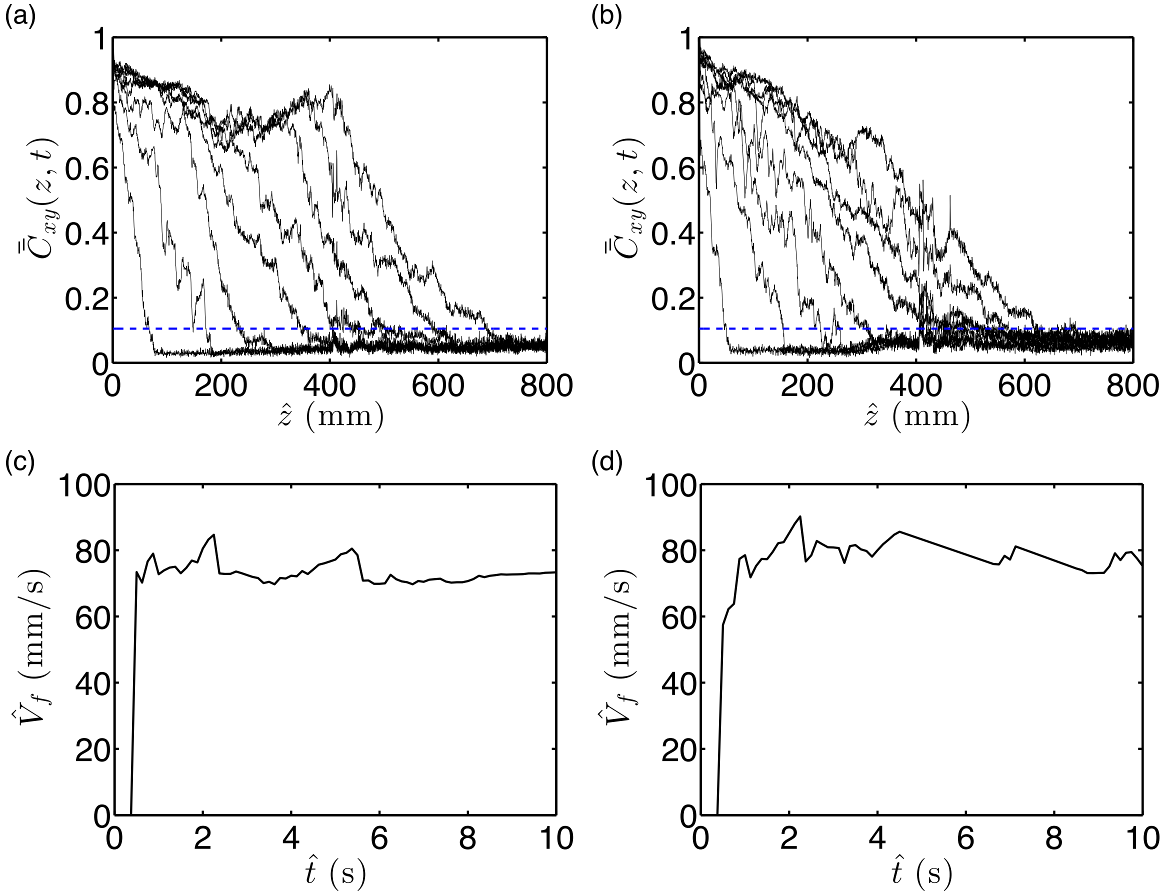

FIGURE 2.8 – Experimental results for $At = 10^{-2}$ and $\hat{V}_0 = 43 \pm 1$ (mm/s): (a) Stationary pipe flow results showing the evolution of the depth-averaged concentration field, $\bar{\bar{C}}_{xy}(z,t)$, with time for $\hat{t} = [1.25, 2.375, 3.625, 4.875, 6.125, 7.25, 8.5, 8.75]$ (s), and streamwise location, $\hat{z}$, measured from the gate valve. The horizontal dashed lines show $\bar{\bar{C}}_{xy}(z,t) = 0.1$, just above the noise level, which is used for measuring the displacing front velocity, $\hat{V}_f$, consistently for all experiments. (b) The same as subfigure *a* but for a moving pipe flow, with $\hat{t} = [1, 2.125, 3.125, 4.125, 5.25, 6.25,\ 7.25, 8.25]$ (s). (c) Stationary pipe flow results showing the evolution of the front velocity value ($\hat{V}_f$), with time for the same experiment as in subfigure *a*. (d) Moving pipe flow results showing the evolution of the front velocity value ($\hat{V}_f$), with time for the same experiment as in subfigure *b*.

mixing in flows with a higher Atwood number, despite stronger driving force (buoyancy) when At increases. Regarding the effect of geometry motion, one observation can be readily made: the difference between long time dimensionless front velocities in stationary and moving pipes is not huge. A more subtle observation is that at smaller At, V_f for displacement flows in a moving pipe usually lies below the one in a stationary pipe. This effect is usually reversed at higher At. More quantitatively, the order of the difference between the mean values of dimensionless front velocities averaged over all times for 6 different value $\hat{V}_0$ in moving and stationary pipes are -0.16, -0.17, 0, 0.02 & 0.25 respectively for $At = 10^{-4}$, 10^{-3}, 3.5×10^{-3},

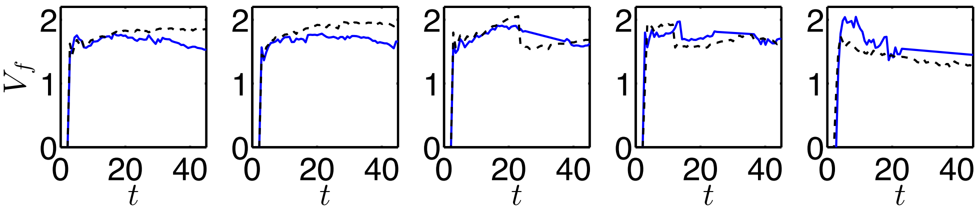

FIGURE 2.9 – Variation of the dimensionless front velocity, V_f, versus the dimensionless time, t, for a stationary pipe (black dashed line) and a moving pipe (blue line) for $At = 10^{-4}$, 10^{-3}, 3.5×10^{-3}, 10^{-2}, 7×10^{-2} (from left to right) and $\hat{V}_0 = 53 \pm 2$ (mm/s).

10^{-2} & 7×10^{-2}.

2.4.4 Macroscopic diffusion coefficient

This section focuses on the displacement flows for which the degree of transverse mixing is relatively high. For these flows, it is therefore expected that the diffusive spreading along the pipe to be an important feature of these flows. As discussed in the introduction section, these diffusive flows have been analysed for exchange flows in vertical (40; 41) and inclined pipes (42; 44; 46) as well as for displacement flows in inclined pipes (18). Our results in this section extend the previous works to the flows in a moving pipe, while also delivering a large amount of data for displacements in a stationary, strictly vertical pipe (as these are also missing in the literature). Debacq *et al.* (40; 41) relied on a similarity scaling for exchange flows in vertical pipes to collapse profiles of the depth-averaged concentration, measured at each time $\hat{t}$ and location $\hat{z}$, onto a master curve which was defined with reference to $\hat{z}/\sqrt{\hat{t}}$. An error function form was then fitted on the master curve to deliver the macroscopic diffusion coefficient of the mean concentration in the pipe. The same approach was used by Seon *et al.* (46) for exchange flows in inclined pipes. For displacement flows, a non-zero mean imposed flow velocity ($\hat{V}_0$) is added to the exchange flow configuration. When the flow is fully mixed transversely, Alba *et al.* (18) assumed that the mixture core travels with the speed $\hat{V}_0$ so that they proposed $(\hat{z} - \hat{V}_0\hat{t})/\sqrt{\hat{t}}$ as a similarity scaling to successfully collapse the depth-averaged concentrations at different times. Here, we adopt an analogous approach.

Fig. 2.10 depicts an example of the attempt to find a collapse of concentration profiles using the similarity scaling mentioned. It is observed that all the concentration evolution profiles are nearly-collapsed onto a single curve, which is shown by a curve fit of $\frac{1}{2}\text{erfc}\left(\frac{\hat{z}-\hat{V}_0\hat{t}}{2\sqrt{\hat{D}_M\hat{t}}}\right)$, inspired by the analytical solution of the linear diffusion equation. It is seen that the collapses of data for stationary and moving pipe flows are reasonable. It must be noted that there are assumptions in using the error-function form fit which is not exactly representatives of the flow reality. For example, it is assumed there is a sort of symmetry in the mixing zone meaning that the area ahead and behind the mixed core, assumed to move with speed of $\hat{V}_0$, is symmetric.

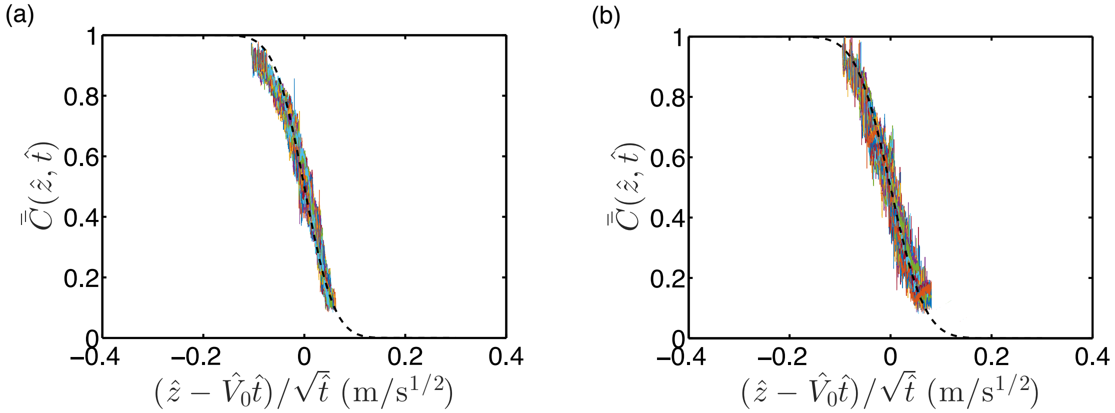

FIGURE 2.10 – Collapse of depth-averaged concentration profiles (at longer times of the flow) with $\left(\hat{z}-\hat{V}_0\hat{t}\right)/\sqrt{\hat{t}}$ for $\hat{V}_0 = 22$ (mm/s) & $At = 10^{-2}$ in (a) a stationary pipe and (b) a moving pipe. The dashed line shows the fitted function of $\frac{1}{2}\text{erfc}\left(\frac{\hat{z}-\hat{V}_0\hat{t}}{2\sqrt{\hat{D}_M\hat{t}}}\right)$, through which the obtained values of $\hat{D}_M$ are 1090 ± 372 (mm^2/s) and 1420 ± 337 (mm^2/s) for stationary and moving pipes.

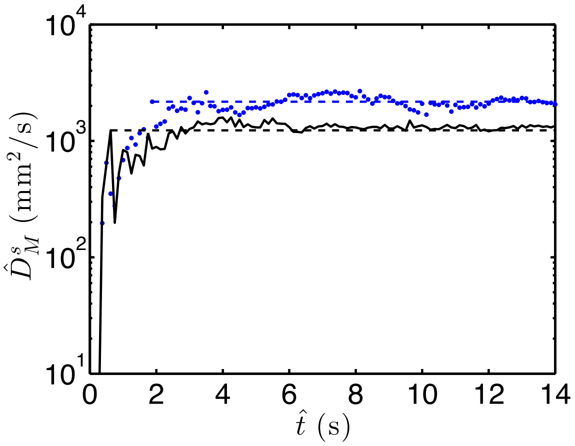

FIGURE 2.11 – Variation of the pseudo macroscopic diffusion coefficient, $\hat{D}^s_M$, versus time at $\hat{V}_0 = 33$ (mm/s) and $At = 7 \times 10^{-2}$ for a stationary pipe (line) and a moving pipe (dots). The horizontal dashed lines depict the long time nearly-steady values, i.e., $\hat{D}_M$.

Almost certainly the symmetry in our system is broken due to the mean imposed flow as well geometrical motion so that the quality of mixing is at least slightly different ahead and behind the mixed core. However, due to the complexity of the flow, this approach seems to be a reasonable attempt as a first step to extract essential leading order information about the flow at the expense of losing information about some physical phenomena.

As discussed, a macroscopic diffusion coefficient can be obtained by fitting the error function form on depth-averaged concentrations at long times over long lengths of the pipe. However, our analysis shows that it is equally possible to attempt to fit the error function form (on a depth-averaged concentration profile for a given time) even from the early stages of the displacement process. This delivers firstly a *pseudo* time-dependent macroscopic diffusion coefficient, as a coarse measurement of the extent of mixing zone at short times. Secondly, it provides understanding of the time scale when the pseudo macroscopic diffusion coefficient attains its nearly-steady value ($\hat{D}_M$), independent of time. To illustrate this, Fig. 2.11 shows the pseudo macroscopic diffusion coefficient, $\hat{D}_M^s$, versus time, for moving and stationary pipes. It can be seen that $\hat{D}_M^s$ is very small initially, implying that the mixed zone is very small. However, very quickly (over a few seconds), $\hat{D}_M^s$ increases rapidly and reaches a nearly-steady value (i.e., $\hat{D}_M$), marked by the dashed lines on this figure. Fig. 2.11 also shows that the initial increase in $\hat{D}_M^s$ are similar for moving and stationary cases but the final macroscopic diffusion coefficient is slightly larger when the pipe is at motion, for the same flow parameter set.

It should be noted that our 2-meter long experimental pipe may not be sufficiently long for the pseudo macroscopic diffusion coefficient to reach its completely steady value. In fact, although performing controlled displacement flow experiments in an extremely long moving pipe may not be technically possible, it should be noted that the values reported for $\hat{D}_M$ may be overestimated due to the shortness of the pipe.

Fig. 2.12 shows the variation of the limiting (nearly-steady) values of the macroscopic diffusion coefficient, $\hat{D}_M$, versus the mean imposed flow velocity for the two largest Atwood numbers of our work. First of all, it can be seen that $\hat{D}_M$ increases significantly with increasing the mean imposed velocity for moving and stationary pipe flows. In both cases, it is also seen that the values of $\hat{D}_M$ for displacements in a pipe moving like an inverted pendulum systematically lie above those of the stationary pipe flow. It also seems that the difference between $\hat{D}_M$ of stationary and moving pipe flows increases by increasing At. Finally, we have superposed the results of a correlation proposed by Alba *et al.* (18) to predict the macroscopic diffusion coefficient in a stationary inclined pipe, where we have replaced the pipe angle with $\beta = 0$. It can be seen that the correlation provides a lower limit for $\hat{D}_M$ in stationary and moving pipes.

Fig. 2.12 showed the increase in $\hat{D}_M$ by moving the geometry in an inverted pendulum-like motion. One may wonder whether or not this feature is independent of the geometry motion. In other words, as the geometry moves, energy is put into the system and one might wonder that this energy has to somehow extend the diffusion length (i.e., increase $\hat{D}_M$). To test this hypothesis, onto Fig. 2.12b, we have also superposed $\hat{D}_M$ found in a pipe slowly moving in vertical reciprocation, with the same frequency as the inverted pendulum oscillation. The vertical reciprocation was over 10 (cm), i.e., ~ 0.05 in terms of the aspect ratio. Fig. 2.12b shows that the values of $\hat{D}_M$ for a pipe in vertical reciprocation are even smaller than the ones for a stationary pipe. This observation provides a counterexample for the hypothesis: the geometrical motion does not always lead to an increase in $\hat{D}_M$. In fact the characteristics of

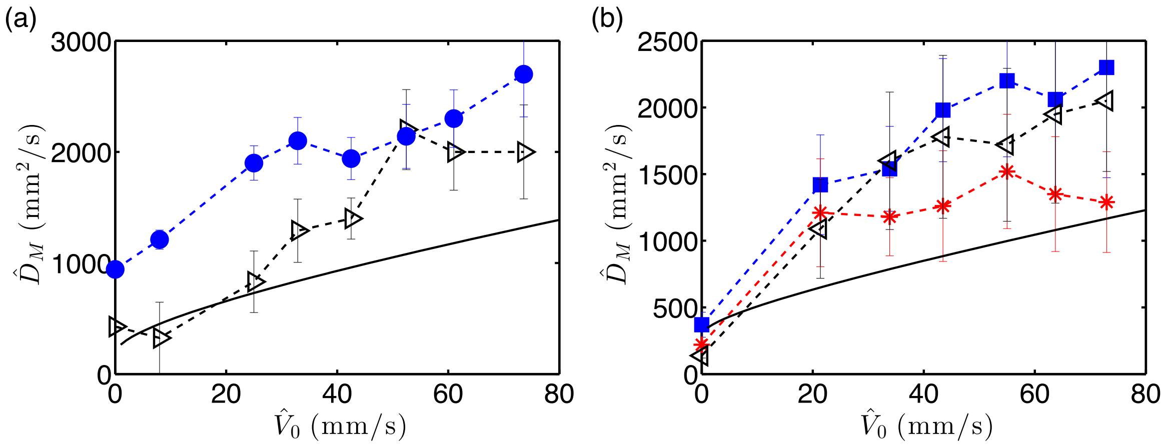

FIGURE 2.12 – Variation of the macroscopic diffusion coefficient, $\hat{D}_M$, versus the mean imposed flow velocity for (a) $At = 7 \times 10^{-2}$ and (b) $At = 10^{-2}$. The hollow symbols are for the stationary pipe and the filled symbols are for pipe moving like an inverted pendulum. There are also additional experimental data from displacements in a pipe moving in vertical reciprocation ($*$). The lines in both graphs show the correlation proposed by Alba *et al.* (18) to predict the macroscopic diffusion coefficient in an inclined pipe $\hat{D}_M = 5 \times 10^3 \left(At^{1/2}\hat{g}^{1/2}\hat{D}^{3/2}\right)(1 + 3.6\tan\beta)^2 \left(\hat{\nu}^{3/2}At^{-3/4}\hat{g}^{-3/4}\hat{D}^{-9/4}\right) +$ $\hat{D}\hat{V}_0 \left(0.6618 + \left(At.\hat{g}\hat{D}\right)^{1/4}\hat{V}_0^{-1/2}\left[0.9054 - 1.838\tan\beta\right]\right)$, in which β is the pipe inclination angle with respect to vertical, where we have used $\beta = 0$. The experimental error bars are estimates through the standard deviation of $\hat{D}_M$. Note that the macroscopic diffusion coefficient is a relevant parameter for higher Atwood number flows.

flow geometry motion play an important role to increase or decrease the macroscopic diffusion coefficient. This may be another motivation to continue our research to study buoyant displacement flows using other geometrical movements.

2.5 Conclusions

We experimentally studied miscible displacement flows in a long, vertical pipe moving slowly like an inverted pendulum. The experimental fluids were Newtonian and they had the same viscosity but small different densities. The experiments were performed at the high-Péclet-number limit so that the main parameters that governed the time-dependent flow were the Reynolds number (Re), the densimetric Froude number (Fr), and the Rossby number (Ro), for which our experiments covered a wide range.

The main findings are as follows. First, the most obvious change that the pipe movement causes on the displacement flows of our study is the appearance of the stable-diffusive regime, in which the fluids slightly mix not so much due to buoyancy but primarily due to the pipe movement. These flows appear at smaller Atwood numbers while the pipe motion dominates.

Accordingly, the regime map classification shows that these flows occur when $Re/Fr^2 < 35$ and $Re/Ro > 70$. In addition, when the pipe moves at relatively small frequencies, a stable flow regime that is non-diffusive is observed at $Re/Fr^2 < 35$ and $Re/Ro < 70$ (crudely). An unstable-diffusive flow regime is observed roughly when $Re/Fr^2 > 35$ for the range of frequencies tested. Second, we have studied the extent of the penetration of the displacing fluid (by studying the front velocity, $\hat{V}_f$) and the extent of the axial mixing (through quantify the macroscopic diffusion coefficient, $\hat{D}_M$). We have shown that both of these quickly increase with time to attain their final nearly-steady values. We have observed that at smaller density differences, $\hat{V}_f$ decreases when the pipe moves while the opposite effect is seen at larger density differences. Studying $\hat{D}_M$, which is relevant for large At flows, reveals that $\hat{D}_M$ is systematically larger for displacement flows in a moving pipe.

The observed behaviours for $\hat{V}_f$ and $\hat{D}_M$ may be explained qualitatively. For low At flows, the pipe motion creates certain "disorder" in the displacement flows compared to stationary pipe displacement flows, where the flow has separate phases and certain macroscopic finger-like structure. This leads to a general decrease in the front velocity of the moving pipe flows. On the other hand, for higher At flows, the geometry motion overall creates certain "order" in the flow (i.e., momentary and local), compared to the stationary case. This is perhaps due to momentary slumping effects that occur as a result of the pipe inclination, causing short-lived segregation between the fluid phases. This furnishes two effects in return. First, the displacing front is able to penetrate relatively faster when the pipe moves so that $\hat{V}_f$ slightly increases. Second, the reduced transverse mixing and the created order in the longitudinal direction lead to a relatively faster expansion of the diffusive region between the two fluids; thus, $\hat{D}_M$ increases when the pipe is in motion.

There exist also other contributions of the current work. First of all, we have developed a simple method to approximate a leading order form of real concentration profiles using 2D experimental images in which contraction profiles are already averaged. Our method may provide a low cost way to study the evolution of 3D concentration profiles in displacement flows. Second, we also have found that the pipe motion includes local and momentary segregation in terms of the frontal interface, which at the same time has a significant delay with respect to the pipe motion time.

The current work may also suggest a number of paths for future research. First, stable-diffusive flows exhibit interesting fingering features close to the displacing front, which can be further investigated, experimentally or numerically. The amount of the near-front dispersion and its relation to Re, Fr, and Ro can be quantified. Second, particle image velocimetry (PIV) or ultrasonic doppler velocimetry (UDV) techniques can be performed to shed further light on the details of the three flow regimes discovered in this work.

Chapitre 3

Removal of a yield stress fluid by a heavier Newtonian fluid in a vertical pipe

Résumé

Le présent travail a pour objectif d'étudier, de manières expérimentale, analytique et numerique, l'élimination d'un fluide de contrainte de plasticité légère déplacé par un fluide Newtonien légèrement plus lourd, à l'intérieur d'un long tuyau vertical. Les fluides d'intérêt sont miscibles et l'écoulement de déplacement est dirigé vers le bas. En général, l'écoulement est contrôlé par au moins qatre nombres sans dimension et leurs combinaisons, à savoir le nombre de Bingham, $0 \leq B_N \leq 18600$, le rapport de viscosité, $1 < m < 9723$, le nombre de Reynolds Newtonien, $13 \leq Re_N \leq 2480$ et le nombre densimétrique de Froude, $0.15 \leq Fr \leq \infty$. Dans les définitions de B_N, m et Re_N, la viscosité constante du fluide de déplacement est utilisé comme échelle de viscosité. Les expériences présentent une variété de modèles d'écoulement différents, pour lesquels plusieurs classifications de régimes peuvent être effectuées. Tout d'abord, des couches de paroi résiduelles entièrement statiques sont observées à $B_N \gtrsim 100$ et des couches résiduelles mobiles se trouvent en dessous de cette valeur de transition, ce qui peut être prédit par un modèle analytique simple (type de lubrification). Deuxièmement, pour les écoulement de déplacement avec $B_N < 100$, les déplacements peuvent être divisés en régimes d'écoulement quasi stables et instables, pour lesquels la transition a lieu à un nombre de flottabilité critique, $\chi = 2Re_N/Fr^2 \approx 120$. Troisièmement, pour les écoulements de fluides avec $B_N \gtrsim 100$, les modèles de couches résiduelles peuvent être classés en trois sous-régimes distincts, notamment les régimes ondulé, ondulé et lisse, en fonction de la valeur de $Re_N/\left(B_N + m\right)$ et Re_N/Fr. Quatrièmement, pour analyser les caractéristiques du front de déplacement secondaire, les expériences sont classées en déplacements centraux et périphériques, pour lesquels la transition peut être raisonnablement prédite par un modèle analytique approprié. Cependant, le modèle analytique ne permet pas d'estimer les vitesses de déplacement avant de longue durée. Enfin, des simulations numériques de la dynamique des fluides dans une géométrie de canal plus simple démontrent que certaines des caractéristiques complexes du flux de déplacement peuvent être prédites par calcul.

Abstract

The present work aims to investigate, experimentally, analytically and computationally, the removal of a light yield stress fluid displaced by a slightly heavier Newtonian fluid, in a long vertical pipe. The fluids of interest are miscible and the displacement flow is downward. In general, the flow is controlled by at least four dimensionless numbers, and their combinations, namely the Newtonian Bingham number, $0 \leq B_N \leq 18600$, the viscosity ratio, $1 < m < 9723$, the Newtonian Reynolds number, $13 \leq Re_N \leq 2480$, and the densimetric Froude number, $0.15 \leq Fr \leq \infty$. In the definitions of B_N, m and Re_N, the displacing fluid's constant viscosity is used as the viscosity scale. The experiments present a variety of different flow patterns, for which a number of regime classifications can be made. First, fully static residual wall layers are observed at $B_N \gtrsim 100$ and moving residual layers are found below this transition value, which can be predicted by a simple analytical (lubrication type) model. Second, for displacement flows with $B_N < 100$, the displacements can be divided into nearly-stable and unstable flow regimes, for which the transition occurs at a critical buoyancy number, $\chi = 2Re_N/Fr^2 \approx 120$. Third, for fluid flows with $B_N \gtrsim 100$, the residual layer patterns can be classified into three distinct sub-regimes, including corrugated, wavy and smooth regimes, as a function of $Re_N/(B_N + m)$ and Re_N/Fr. Fourth, to analyse secondary displacement front features, the experiments are phenomenologically classified into central and periphery displacements, for which the transition can be reasonably predicted by an appropriate analytical model. However, the long time displacing front velocities cannot be estimated by the analytical model. Finally, computational fluid dynamics simulations in a simpler channel geometry demonstrate that some of the complex displacement flow features may be predicted computationally.

3.1 Introduction

Displacement flows appear in a diverse range of physical and engineering phenomena, perhaps with the most prominent applications in oil and gas industries (1; 2; 97), food industries (4; 5), plastic manufacturing (7), and numerous other applications (8; 9; 10; 11). Laminar miscible flows with density ratios in circular vertical pipes are quite common in many processes. The displaced fluid in many applications exhibits yield stress behaviours, making it hard to remove out of the flow geometry. In the present work, we aim to fundamentally study the removal of a yield stress fluid from a long, vertical pipe, through displacing it by a slightly heavier Newtonian fluid.

Our motivation for this research comes from cementing processes of oil and gas wells, in which cement (heavier) is pumped into the oil well to remove in-situ gelled-like drilling mud (lighter). The displacement process initially involves a downward removal of drilling mud by cement along a casing (i.e. a circular pipe) and then an upward removal along the annular section of the well. This process plays a crucial role in mechanically supporting the well, protecting the casing against corrosive materials, preventing water penetration into the well, and perhaps most importantly, providing a zonal isolation. The failure to achieve these objectives significantly limits the ability of the well to reach its full production potential (2). The success in primary cement is strongly linked to the efficiency of the removal of the in-situ fluid, which has a yield stress, through a buoyant displacement process (12).

Understanding miscible displacement flows may begin with analysing their exchange flow counters, in which there is no imposed displacement flow velocity. Miscible buoyant exchange flows of Newtonian fluids in different geometries have been investigated in detail. For instance, Debacq *et al.* (40; 41) have experimentally studied miscible exchange flows in a vertical pipe, finding stable and unstable flow regimes versus the Atwood number (At), i.e. the ratio between the density difference and the sum of densities, and a parameter that can be described as the ratio between the Newtonian Reynolds number and the densimetric Froude number, i.e. Re_N/Fr (see Table 3.2 for the definitions of these dimensionless numbers). Seon *et al.* (43; 44; 45) and Hallez *et al.* (71; 72) respectively have studied similar buoyant exchange flows at different pipe inclinations, experimentally and computationally, and they have analysed the effects of Re_N/Fr on the flow stability. By imposing a pressure gradient (resulting in an imposed mean velocity), these works have been extended to displacement flows in a series of papers for near horizontal (15; 16; 17), inclined (18; 105), strictly vertical (121) and non-uniform (22) flow geometries. Various flow regimes, including stable, unstable and diffusive regimes, and several flow features, such as heavy and light fluid front velocities, have been extensively studied.

Yield stress fluid displacement flows are being increasingly studied in the literature, in Hele-Shaw cells (33; 57; 64; 127; 128; 129), capillary tubes (130; 131; 132), porous media (133; 134), 2D channels (21; 25; 67; 135; 79), and pipes (31; 32; 58; 70; 136). Transient displacements (26), start-up flows (66) and pulsating displacements (30) have been investigated. Many of the previous works in the literature of yield stress displacements have looked into the residual layers of the displaced fluid left on the flow geometry walls, as its formation is an intriguing flow feature with crucial practical consequences. The difficulty of removing these layers, especially from the interior sections of flow geometries, is currently receiving attention. Poslinski *et al.* (91) have experimentally investigated the displacement of a yield stress fluid by air in a tube, revealing that the thickness of the residual layers of yield stress displaced fluids is much larger than that of their Newtonian counterparts. Allouche *et al.* (25) have shown that the displaced fluid residual layers may remain completely static on the walls when the yield stress of the displaced fluid is larger than that of the displacing fluid. Dimakopoulos and Tsamopoulos (26) have studied the displacement flow of a yield stress fluid by a Newtonian fluid in straight and suddenly constricted tubes, finding that unyielded regions arise in front of the displacing fluid in straight tubes and unyielded regions appear near the recirculation corners for constricted ones. Gabard and Hulin *et al.* (136) have experimentally evaluated the effects of the presence of a yield stress on miscible displacement flows in a vertical tube. They have found that the transient residual film thickness for yield stress fluids is smaller than that for shear-thinning fluids. Cole *et al.* (59) have studied the removal of residual layers of a yield stress fluid from surfaces at two length scales: laboratory and pilot scales. Their work has revealed that the time required for the removal of the residual layers of a yield stress fluid from a pipe can be affected by the velocity and temperature of the displacing fluid, but not much by the pipe length.

Buoyant and iso-dense displacement flows of yield fluids have been studied for specific situations. For example, Taghavi *et al.* (31) and Alba *et al.* (32) have experimentally discovered centre-type and slump-type regimes in buoyant displacements in inclined pipes, depending on the value of Re_N/Fr and independent of the yield stress value (as long as it is large). They have found that in centre-type displacements, the displacing fluid moving in the pipe centre leaves behind a nearly uniform layer of the yield stress fluid on the walls and that the displacing fluid in slump-type displacements advances underneath the yield stress fluid. Moisés *et al.* (58) have experimentally analysed iso-dense displacements of a yield stress fluid by a Newtonian fluid in a horizontal pipe. They have identified three different flow regimes associated with the appearance of static residual wall layers, namely *smooth*, *wavy* and *corrugated* regimes, for which an effective Reynolds number governs the transition. More recently, Zare and Frigaard (21) have numerically analysed the effects of buoyancy on micro-annulus formation in a vertical 2D channel, by considering the displacement of a yield stress fluid by a Newtonian one. They have found that in the density-unstable situations, static residual wall layers can exist for yield stress values below the minimum for density-stable regimes.

The current chapter considers experimentally, analytically and computationally the flow of a light yield stress fluid displaced by a slightly heavier Newtonian fluid, in a long vertical pipe, for which the novelty arises mainly from considering the framework of gradually increasing the yield stress of the displaced fluid, the imposed mean velocity, as well as the density difference between the two fluids. Therefore, to analyse the effects of these parameters, a wide range of flow dimensionless groups are considered. Our work attempts to furnish an understanding about these complex displacement flows by providing flow regime maps, which are of significant value, and by studying various flow regimes using a combined methodology.

The outline of the chapter is as follows. In Section 3.2 the problem setting is explained. In Section 3.3 the experimental setup and procedures are described. Sections 3.4, 3.5 and 3.6 present the experimental, analytical and computational results. Finally, Section 3.7 concludes the paper with a brief summary of the main findings.

3.2 Problem setting

In this paper, we deal with a displacement flow configuration in which a light yield stress fluid is displaced by a heavier Newtonian fluid (at small density differences), along a vertical pipe (with length $\hat{L}$). The pipe diameter and the imposed mean velocity are $\hat{D}$ and $\hat{V}_0$, respectively. The imposed flow is laminar, the displacement is downward, and the fluids are miscible. The light fluid has a yield stress ($\hat{\tau}_y$). Also, the viscosity of the heavy fluid ($\hat{\mu}_H$) and the plastic viscosity of the light fluid ($\hat{\mu}_L$) are different. The pipe aspect ratio is large, satisfying $\hat{D}/\hat{L} \ll 1$. The initial interface is located far away from both ends of the pipe, transverse to the pipe axis. Fig. 3.1 illustrates a schematic view of our displacement system.

Considering the Cartesian coordinates $(\hat{x}, \hat{y}, \hat{z})$ or the cylindrical coordinates $(\hat{r}, \theta, \hat{z})$, a flow model can be formulated through the equations of motion coupled to a concentration-diffusion equation:

$$[1 - \phi At]\, Re_N[\mathbf{u}_t + (\mathbf{u}.\nabla)\mathbf{u}] = -\nabla p + \nabla.\tau - \frac{\phi\chi}{2}\mathbf{e}_g, \tag{3.1}$$

$$\nabla.\mathbf{u} = 0, \tag{3.2}$$

$$c_t + \mathbf{u}.\nabla c = \frac{1}{Pe}\nabla^2 c, \tag{3.3}$$

where $\mathbf{u} = (w, v, u)$ denotes the velocity, p the pressure and τ the stress. The function $\phi(c) = 1 - 2c$ changes between 1 and -1 for concentrations in the range of $c \in [0, 1]$, with $c = 0$ representing the pure displaced fluid and $c = 1$ the pure displacing fluid. We also have $\mathbf{e}_g = (0, 0, 1)$. The above equations are made dimensionless with $\hat{D}$ as length scale and $\hat{V}_0$ as velocity scale. The pressure and stresses are also scaled with $\hat{\mu}_H\hat{V}_0/\hat{D}$. The dimensionless groups appearing in the above equations, such as Re_N, At, χ, Pe, etc., are defined in Table 3.2 (also see Table 3.1 for the dimensional parameters).

Regarding the constitutive equations, for the Newtonian displacing fluid we simply have

$$\tau_{H,ij} = \dot{\gamma}_{ij}. \tag{3.4}$$

For viscoplastic fluids, it is common to consider a Herschel-Bulkley fluid model, which incorporates also the simpler Bingham, power-law and Newtonian models, described by three (dimensional) parameters: a fluid consistency ($\hat{\kappa}$), a yield stress ($\hat{\tau}_y$) and a power-law index (n):

$$\dot{\gamma}(\mathbf{u}) = 0 \Longleftrightarrow \tau_L(\mathbf{u}) \le B_N, \tag{3.5}$$

$$\tau_{L,ij}(\mathbf{u}) = \left[m\dot{\gamma}^{n-1}(\mathbf{u}) + \frac{B_N}{\dot{\gamma}(\mathbf{u})}\right]\dot{\gamma}_{ij}(\mathbf{u}) \Longleftrightarrow \tau_L(\mathbf{u}) > B_N, \tag{3.6}$$

where the strain rate tensor has components:

$$\dot{\gamma}_{ij}(\mathbf{u}) = \frac{\partial u_i}{\partial x_j} + \frac{\partial u_j}{\partial x_i}, \tag{3.7}$$

and the second invariants, $\dot{\gamma}(\mathbf{u})$ and $\tau_k(\mathbf{u})$, are defined by:

$$\dot{\gamma}(\mathbf{u}) = \left[\frac{1}{2}\sum_{i,j=1}^{3}[\dot{\gamma}_{ij}(\mathbf{u})]^2\right]^{1/2}, \qquad \tau_L(\mathbf{u}) = \left[\frac{1}{2}\sum_{i,j=1}^{3}[\tau_{k,ij}(\mathbf{u})]^2\right]^{1/2}. \tag{3.8}$$

So far, we observe that in general seven dimensionless parameters govern our flow. These are the Atwood number (At), the Newtonian Bingham number (B_N), a buoyancy number (χ):

$$\chi = \frac{2Re_N}{Fr^2},$$

the shear-thinning power-law index (n), the viscosity ratio (m), the Péclet number (Pe), and the Newtonian Reynolds number (Re_N). We consider small density differences and hence small Atwood numbers, implying that

$$[1 - \phi At]\, Re_N \approx Re_N.$$

However, note that the buoyancy force can be still significant on the right-hand-side of equation (2.1). We also assume that Pe is large, implying that diffusive effects are limited to an interfacial layer which is thin and sharp in the absence of instability, dispersion, and mixing. This results in ignoring the right-hand-side of equation (2.3). In order to simplify our analysis, we will not focus on the effects of n, but instead attempt to explain the main flow features concentrating on B_N, Fr, Re_N, m or their combinations.

It could be informative to present the ratio of the Newtonian Reynolds number and the densimetric Froude number as

$$\frac{Re_N}{Fr} \equiv \frac{\hat{\rho}\hat{V}_0\hat{D}/\hat{\mu}_H}{\hat{V}_0/\sqrt{At\hat{g}\hat{D}}} \equiv \frac{\sqrt{At\hat{g}\hat{D}}\hat{D}}{\hat{\nu}},$$

in which $\sqrt{At\hat{g}\hat{D}}$ can be considered as a characteristic inertial velocity found via a balance of inertial and buoyant stresses. It is interesting to note that, for small density differences, Re_N/Fr is equivalent to the square root of the Archimedes number, which represents the strength of buoyancy.

Table 3.2 summarizes the definitions and the ranges of the main dimensionless numbers throughout this work. Note that some of the definitions are non-traditional; therefore, it is worth mentioning how these dimensionless numbers can be simply converted to perhaps more “meaningful” dimensionless numbers in the context of displacement flows, which we denote using the superscript $*$. First, m is not the usual *effective* viscosity ratio (m^*); the latter is commonly defined as the ratio between the effective viscosity of the yield stress fluid ($\hat{\tau}_y\left[\hat{V}_0/\hat{D}\right]^{-1} + \hat{\kappa}\left[\hat{V}_0/\hat{D}\right]^{n-1}$) to that of the Newtonian fluid ($\hat{\mu}_H$). Following (132; 137) the conversion between m and m^* is simply:

$$m^* = \frac{\hat{\kappa}\left[\frac{\hat{V}_0}{\hat{D}}\right]^{n-1} + \hat{\tau}_y\left[\frac{\hat{V}_0}{\hat{D}}\right]^{-1}}{\hat{\mu}_H} = m + B_N$$

Second, B_N is a *Newtonian* Bingham number and it is defined based the Newtonian fluid's viscosity. Thus, it is not the common Bingham number (i.e. typically based on the yield stress fluid's plastic viscosity: $\hat{\mu}_L = \hat{\kappa}\left[\hat{V}_0/\hat{D}\right]^{n-1}$); however, in place of the common Bingham number, in the context of displacement flows, an "effective" Bingham number (B_N^*) can be suggested (137) by taking into account the effective viscosity of the yield stress fluid. Therefore, the conversion between the Newtonian Bingham number and the effective Bingham number can be written as

$$B_N^* = \frac{\hat{\tau}_y}{\hat{\tau}_y + \hat{\kappa}\left[\frac{\hat{V}_0}{\hat{D}}\right]^n} = \frac{B_N}{B_N + m}$$

Finally, in a similar manner as discussed above and using the effective viscosity of the displaced fluid, an effective Reynolds number can be defined as

$$Re_N^* = \frac{\hat{\rho}\hat{V}_0\hat{D}}{\hat{\tau}_y\left[\frac{\hat{V}_0}{\hat{D}}\right]^{-1} + \hat{\kappa}\left[\frac{\hat{V}_0}{\hat{D}}\right]^{n-1}} = \frac{Re_N}{B_N + m}.$$

3.3 Experimental setup and procedures

Our experiments are carried out in a vertical transparent pipe, with the length of 202 (cm) and the inner diameter of 0.96 (cm) (see Fig. 3.1). The setup consists of a gate valve, situated at 39 (cm) from the top end. At the beginning (as an initial condition), the two parts of the pipe (below and above the gate valve) are completely separated. A peristaltic pump is used to fill the lower part by a yield stress fluid (Carbopol solution (Carbomer 940)). A small amount of ink (Fountain Pen India black ink) is added to the yield stress fluid for visualization purposes. The upper part of the pipe is filled by a heavy Newtonian fluid (water-salt solution). A large elevated tank is employed to feed the upper part of the pipe, to generate a constant and smooth flow rate fed by gravity. The flow rate is adjusted by a needle valve and measured by a flow meter (Omega FTB 421, low flow plastic turbine), which are both located downstream of the pipe.

An experiment starts with an instant opening of the gate valve. Meanwhile, a high speed camera (Blaser acA2040 model) records the images of the displacement flow. The field of view that is covered by the camera is typically 8×800 (mm^2), located 24 (mm) below the gate

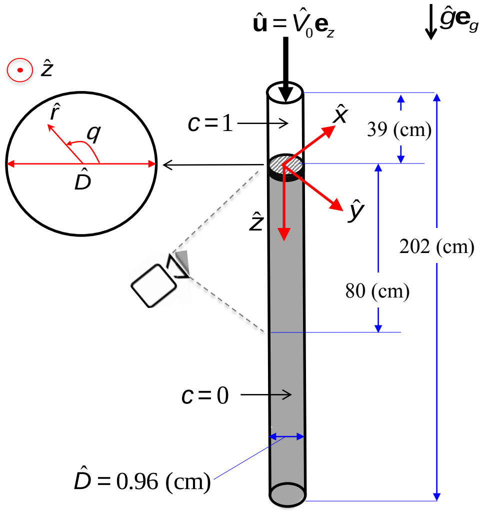

FIGURE 3.1 – Schematic views of the experimental setup.

valve. The recorded images are in the $\hat{z}\hat{y}$-plane. The pipe is back lit by Light-Emitting Diode (LED) strips employed to increase the quality of images. A diffuser layer is placed between the LED strips and the pipe to enhance light homogeneity. Light absorption calibrations are done in the usual fashion.

3.3.1 Fluid preparation and characterisation

Salts are widely used as a weighting agent in fluid mechanics experiments. In our experiments, sodium chloride (NaCl) plays the weighting agent role. In ambient temperature, NaCl is dissolved into water to provide our desirable heavy fluid (displacing fluid). A high precision density meter (Anton Paar DMA 35) is used to measure the density of fluids.

Carbopol is used as the main component to produce our yield stress fluids. Carbopol (a water-based, transparent gel) is widely used in a vast range of applications as a stabiliser, thickener, and suspending agent (138; 139). The rheology of Carbopol solutions is significantly controlled by two main parameters: pH and the Carbopol concentration. Initially, Carbopol is gradually mixed with water using a mixer with a constant rotational speed (350 (rpm)). The mixing time is around 30 minutes. In this stage, the solution is acidic (with a pH in the range of 3.7 to 4.7), with no yield stress. To have a yield stress solution, a neutralizing agent, which in our work is NaOH (dissolved in deionized water), is added to the mixture of Carbopol and water. The ratio of Carbopol to NaOH is 3.44, keeping the pH in the range of 6-8. A calibrated pH meter (Fisher Scientific accumet AB15 pH meter) is used to measure the pH of the Carbopol solutions. The density of the neutralized solutions is fairly close to the density of water.

To measure the rheological parameters of the Carbopol solutions, a Discovery Hybrid Rheometer (DHR) is used with a cone-and-plate geometry. The diameter of the cone-and-plate, the gap at the cone tip and the cone angle are 40 (mm), 54 (μm) and 2.04 (°), respectively. To eliminate wall slip, fine sandpapers are attached to the surfaces of the parallel plates (140). Assuming viscoplastic properties and neglecting elastic effects for our solutions, the behaviour of our Carbopol gel can be described by the Herschel-Bulkley model, as described earlier. Eleven different Carbopol solutions (with Carbopol concentration of 0, 0.01, 0.02, ... 0.09, 0.1 % (wt/wt)) are made and employed as the displaced fluid in our experiments. Fig. 3.2 shows the shear rate-shear stress diagram for these Carbopol solutions fitted by the Herschel-Bulkley model curves (dashed lines). Based on these results, the compositions and the rheological parameters (yield stress ($\hat{\tau}_y$), fluid consistency index ($\hat{\kappa}$) and power-law index (n)) of our Carbopol gels are given in Table 3.3.

It is worth noting that Fig. 3.2 reveals that for some Carbopol solutions the behaviour of the flow curve does not seem asymptotic in the limit of very small shear rates, a feature that is sometimes associated with wall slip effects when yield stress fluids are subjected to very low shear rates. To avoid wall slip during rheometry, sometimes hatched or sandblasted surfaces are employed (132). An alternative is to use sandpapers attached to the parallel plates' surfaces in the rheometer (140) as it is the case in our measurements. Therefore, in our case, it is unlikely that the deviation from the asymptotic behaviours is due to wall slip effects. In fact, it is perhaps more likely that the deviation is because of the characteristics of our Carbopol-based solutions, which are incompatible with the Herschel-Bulkley model in the limit of very small shear rates. It is known that the underlying assumption of an infinite viscosity in the Herschel-Bulkley model at the limit of zero shear rate results in poor curve fittings to data pertaining to some yield stress fluids, e.g. Carbopol-based solutions (141). To deal with this issue, several methods have been proposed in the literature, which are mainly based on modifying the yield stress fluid's constitutive equation (see, e.g. (132) and (141)). However, when the very small shear rate range is not of interest, it is also common to discard the deviation in the flow curve at this range, as carried out in our work.

3.3.2 Validations

Many comparisons were made with the available data in the literature for similar buoyant flows (18; 32; 41; 58), to make sure about the performance of the experimental apparatus as well as verify our experimental results. More specifically, the heavy fluid interpenetration velocity (front velocity) for several Newtonian exchange flows in a vertical pipe was successfully compared with the literature results (41). For iso-density displacement flows of yield stress fluids, our results were compared with those of Moisés *et al.* (58). For these flows, these

TABLE 3.1 – Range of the dimensional parameters used in our experiments.

Parameter	**Name**	**SI Unit**	**Range or value**
$\hat{C}_{\text{Carbopol}}$	Carbopol concentration	% (wt/wt)	$(0-10)\times10^{-2}$
$\hat{D}$	Pipe diameter	m	9.6×10^{-3}
$\hat{L}$	Total pipe length	m	2.02
$\hat{V}_0$	Imposed mean velocity	m/s	$1.5-230\times10^{-3}$
$\hat{\kappa}$	Fluid consistency index	Pa.s^n	$(1.3-3670)\times10^{-3}$
$\hat{\rho}_H$	Heavy fluid's density	kg/m^3	$(9.984-10.183)\times10^{2}$
$\hat{\rho}_L$	Light fluid's density	kg/m^3	9.982×10^{2}
$\hat{\rho}=\frac{\hat{\rho}_H+\hat{\rho}_L}{2}$	Mean fluid's density	kg/m^3	$(9.983-10.082)\times10^{2}$
$\hat{\tau}_y$	Yield stress	Pa	$0-5.6$

TABLE 3.2 – Range of the dimensionless parameters used in our experiments for non-zero values of $\hat{V}_0$. The molecular diffusivity, $\hat{D}_m$, of pure liquid water at an ambient temperature is 2.3×10^{-9} (m^2/s) (121). The relevant dimensional parameters are given in Table 3.1. Note that some of the dimensionless groups are non-traditional: B_N is defined using the Newtonian fluid's viscosity and it is not the usual Bingham number (i.e. typically based on the yield stress fluid's plastic viscosity); Re_N is also defined using the Newtonian fluid's viscosity; m shows the ratio of the yield stress fluid's plastic viscosity to the Newtonian fluid's viscosity.

Parameter	**Name**	**Definition**	**Range**
At	Atwood number	$\frac{\hat{\rho}_H-\hat{\rho}_L}{\hat{\rho}_H+\hat{\rho}_L}$	$(0-5)\times10^{-2}$
B_N	Newtonian Bingham number	$\frac{\hat{\tau}_y\hat{D}}{\hat{\mu}_H\hat{V}_0}$	$(0-18.6)\times10^{3}$
Fr	Densimetric Froude number	$\frac{\hat{V}_0}{\sqrt{At\hat{g}\hat{D}}}$	$(1.5-600)\times10^{-1}$
n	Power-law index	$-$	$(3-9.9)\times10^{-1}$
m	Viscosity ratio	$\frac{\hat{\mu}_L}{\hat{\mu}_H}=\frac{\hat{\kappa}\left[\hat{V}_0/\hat{D}\right]^{n-1}}{\hat{\mu}_H}$	$1-9723$
Pe	Péclet number	$\frac{\hat{V}_0\hat{D}}{\hat{D}_m}$	$(7.2-1104)\times10^{3}$
Re_N	Newtonian Reynolds number	$\frac{\hat{\rho}\hat{V}_0\hat{D}}{\hat{\mu}_H}$	$(1.3-248)\times10^{1}$
Re_N^*	Effective Reynolds number	$\frac{Re_N}{B_N+m}$	$0.0007-106$
χ	Buoyancy number	$\frac{2Re_N}{Fr^2}$	$1.193\times10^{-4}-3.348\times10^{3}$

TABLE 3.3 – Rheological measurements for Carbopol composition and determined parameters, using the Herschel-Bulkley model at 23± 0.05 (°C).

#	Carbopol % (wt/wt)	NaOH % (wt/wt)	$\hat{\kappa}$ (Pa.s^n)	n	$\hat{\tau}_y$ (Pa)
Nulla	0	0	0.001	1	0
I	0.01	0.0029	0.0013±0.0005	0.99±0.01	0
II	0.02	0.0058	0.0031±0.001	0.98±0.01	0
III	0.03	0.0087	0.0077±0.002	0.91±0.06	0.045±0.005
IV	0.04	0.0116	0.06 ±0.01	0.73±0.04	0.1±0.03
V	0.05	0.0145	0.077±0.02	0.72±0.08	0.34±0.05
VI	0.06	0.0174	1±0.10	0.47±0.05	0.37±0.08
VII	0.07	0.0203	1.34±0.20	0.45±0.04	1.4±0.22
VIII	0.08	0.0232	1.29±0.10	0.51±0.03	1.78±0.18
IX	0.09	0.0262	3.47±0.40	0.35±0.03	3.55±0.60
X	0.10	0.0290	3.67±0.50	0.43±0.04	5.05±0.55

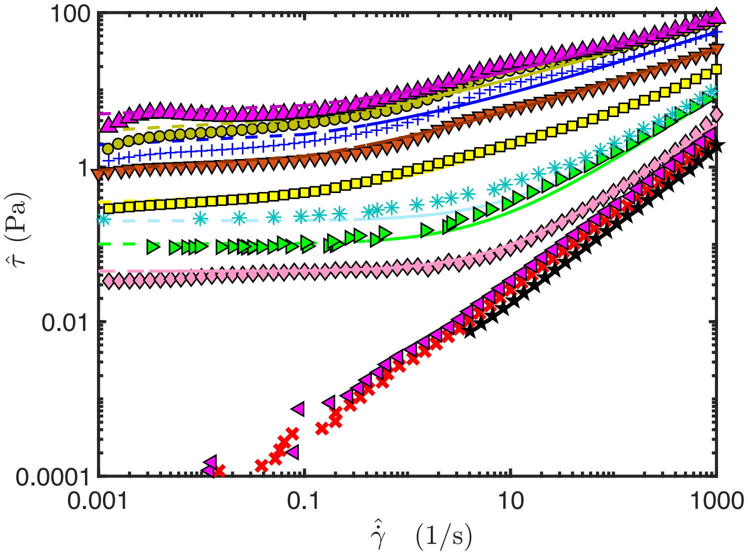

FIGURE 3.2 – Rheological curves (symbols) and their related Herschel-Bulkley model fits (dashed lines) for the different Carbopol solutions presented in Table 3.3, according to which the concentration of Carbopol gradually increases: *Nulla* (⋆), I (×), II (◀), III (♦), IV (▶), V (∗), VI (■), VII (▼), VIII (+), IX(●), and X (▲).

authors found three different flow regimes based on the appearance of static residual wall layers (with different levels of residual layers), called smooth, wavy and corrugated regimes; they quantified the transitions between these regimes using a Reynolds number defined as $\frac{8\hat{\rho}\hat{V}_0^2}{\hat{\tau}_y+\hat{\kappa}\hat{\dot{\gamma}}_c^n}$, where $\hat{\dot{\gamma}}_c = 8\hat{V}_0(3n+1)/4n\hat{D}$. This Reynolds number in (58) is similar to Re_N^* in our work (in fact for $n = 1$, they are identical). For their configuration (i.e. an iso-dense displacement flow in a horizontal pipe), they identified two critical transitions: The smooth-wavy transition occurring at $\frac{8\hat{\rho}\hat{V}_0^2}{\hat{\tau}_y+\hat{\kappa}\hat{\dot{\gamma}}_c^n} \approx 1$ and the wavy-corrugated transition occurring at $\frac{8\hat{\rho}\hat{V}_0^2}{\hat{\tau}_y+\hat{\kappa}\hat{\dot{\gamma}}_c^n} \approx 0.2$. For our vertical iso-dense configuration ($At = 0$), we have found these transitions to occur roughly at $Re_N^* \approx 0.894$ and $Re_N^* \approx 0.062$, respectively, which order-wise agree with the findings of (58).

3.4 Experimental results

This section is divided into three parts. First, our experimental results and various flow regimes are qualitatively described. Next, a complete regime classification is provided. Finally, the displacing fluid front velocities are analysed.

3.4.1 Qualitative description of different flow regimes and patterns

Let us first qualitatively describe the main features of the displacement flows observed in our experiments. One of the original aspects of the current work is the consideration of a wide range of yield stresses ($0 \leq B_N \leq 18600$), imposed mean velocities ($13 \leq Re_N \leq 2480$), and density differences ($0.15 \leq Fr \leq \infty$). For Newtonian fluids (i.e. at zero yield stress), Amiri *et al.* (121) have studied buoyant displacement flows in a vertical pipe for a wide range of imposed mean velocities and density differences. It is therefore insightful to analyse how qualitative displacement behaviours in (121) are progressively affected by gradually increasing the Carbopol concentration, which in return results in increasing the yield stresses and the viscosity of the displaced fluid. In a dimensionless form, these effects can be captured by increasing Re_N^*, as depicted in Fig. 3.3. This figure shows experimental snapshots in which the displacement flow at long times is considered. The experimental snapshots show calibrated concentration values between 0 and 1 (the displaced fluid rheology is labeled according to Table 3.3). In each row, from left to right, the concentration of Carbopol in the displaced fluid increases. The top and bottom rows show experimental snapshots with the same parameters, albeit with different Fr (i.e. a small and a slightly larger density difference are considered in the top and bottom rows, respectively). For the displacements with the smaller density difference (top row), i.e. larger Fr, when the Carbopol concentration is zero, we observe a nearly Poiseuille-like flow. By increasing the Carbopol concentration, we see that the flow undergoes significant changes, with the flow morphology showing a strong dependence on the displaced fluid's yield stress. When the yield stress is small (up to case #IV), by increasing the Carbopol concentration certain interfacial instabilities appear, which are nevertheless weak and unable to mix the two fluid instabilities. These are nearly-stable flows. In addition, as the displacing front moves downward, there appear to be residual wall layers of the displaced fluid behind the front, but these layers move downward as time proceeds (not shown) and therefore they are not static. When the yield stress is large (cases #V to #X), there exist static residual wall layers of the dark displaced fluid, with exotic patterns. Our experiments (not shown) reveal these layers remain unchanged along the pipe, for a reasonably long time after the displacing front has moved out the flow geometry. As the yield stress increases, the "waviness" of the interface and the amplitude of the static wall residual layer increase. For the displacements at a slightly larger density difference (bottom row), i.e. smaller Fr, the flow patterns change. First of all, at small yield stresses (up to case #IV), the flow is quite unstable and there is a strong mixing between two fluids due to the buoyancy force. The residual layers of the displacement are not static, and they will eventually move downward (not shown for brevity). On the other hand, at large yield stresses (cases #V to #X), the flow transitions to a regime for which smooth static residual layers of the Carbopol gel are observed. Similar to the larger Fr flows, these layers remain unchanged with respect to the time and position. However, in contrast to the larger Fr flows, these static layers show very low amplitude variations (e.g. compare cases #VIII-X in the top and bottom rows). The results of Fig. 3.3 reveal that the displacement flow patterns are highly sensitive to the variations in the yield stress and density difference when they gradually increase from small values.

We have so far observed that the flow morphology and patterns, as well as wall residual layers highly, depend on the experimental flow conditions. In general, there exist two main flow regimes in our yield stress fluid displacements: One flow regime with moving residual layers and one flow regime with nearly static residual wall layers. While the former is associated with the continuous and rapid decrease in the residual layers of the displaced fluid over time, the latter implies that the residual layers are stationary over a long period.

In addition to the main classification with respect to moving and static residual layers, there are also sub-regimes within each of these main regimes. Our experiments show that in terms of the flow dynamics, moving residual layer flows can present nearly-stable and unstable flows, as depicted in Fig. 3.4. In the nearly-stable sub-regime, there are either no interfacial instabilities or these instabilities are quite weak so that they are unable to induce mixing between two fluids (see also the corresponding spatiotemporal diagram in Fig. 3.4). The unstable flows, contrarily, exhibit strong mixing between the fluids (see also the corresponding spatiotemporal diagram in Fig. 3.4).

Stationary residual layer flows can present sub-regimes with smooth, wavy and corrugated residual layers, as studied in detail for iso-density displacements of yield stress fluid flows in (58). Our experiments show that smooth, wavy and corrugated residual regimes can also appear in weakly buoyant displacement flows. For clarity, let us briefly explain these regimes using Fig. 3.5, wherein the relevant image sequences and the corresponding spatiotemporal

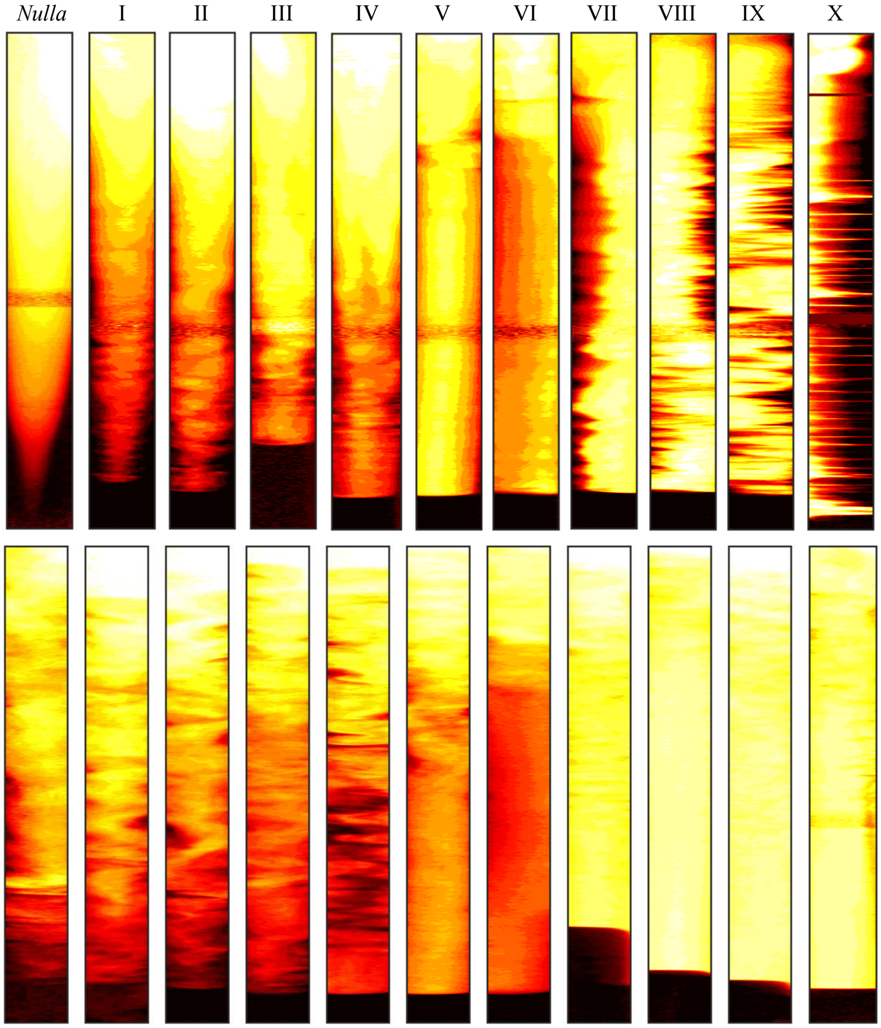

Figure 3.3 – Experimental snapshot images showing a Newtonian fluid (salt water) displacing a yield stress fluid (Carbopol solution at different concentrations). In the top and bottom rows, $Fr = 1.95$ and $Fr = 0.66$, respectively. $Re_N \approx 115$ for all cases. From left to right, $Re_N^* = [115, 88.61, 37.16, 2.71, 0.84, 0.33, 0.097, 0.053, \; 0.044, 0.019, 0.015]$. From left to right, the Carbopol concentration gradually increases according to Table 3.3 as marked on the top of each image. The field of view in each snapshot is 8×800 (mm^2) located 24 (mm) below the gate valve.

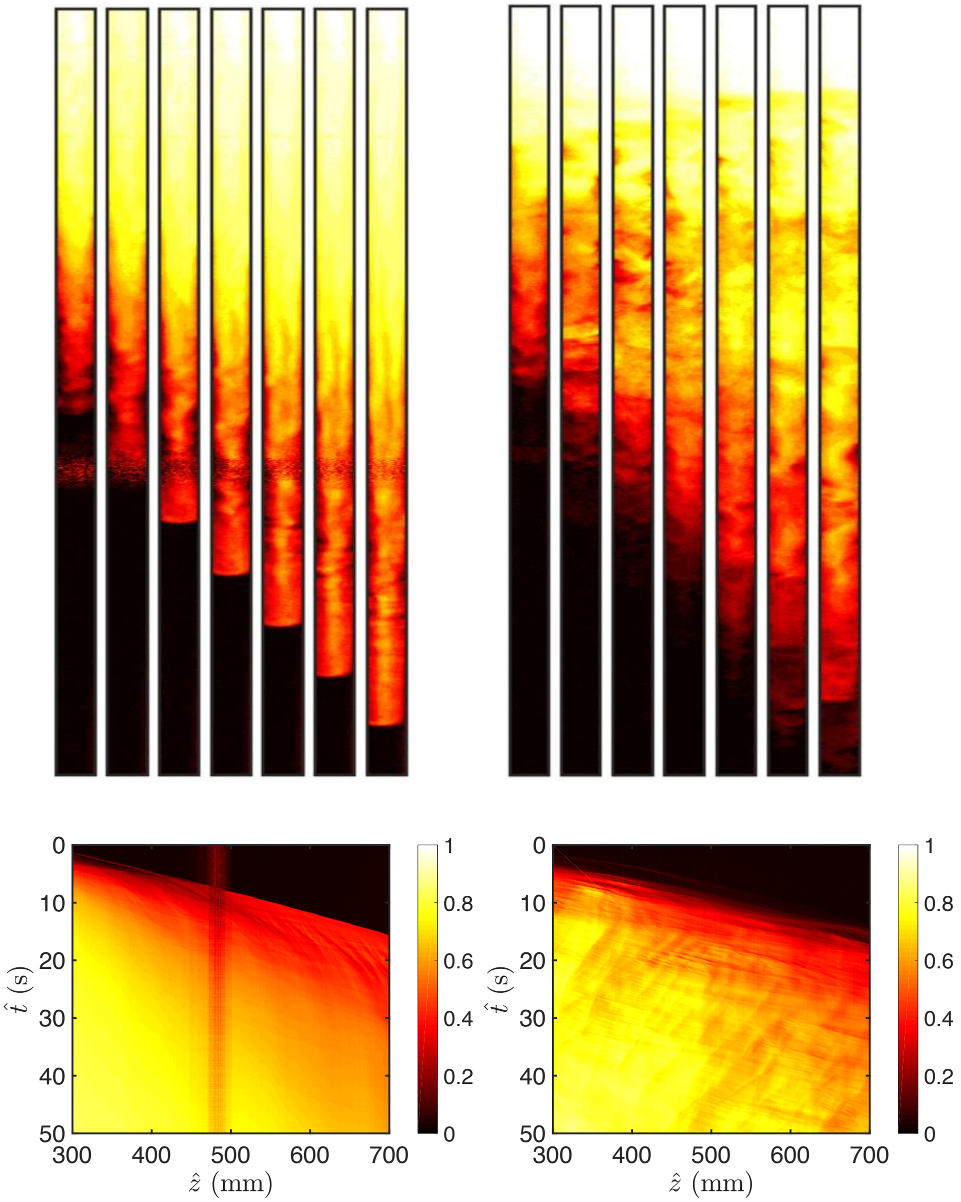

FIGURE 3.4 – The top row shows two panels each containing a sequence of experimental images, showing from left to right nearly-stable and unstable displacements. The flow parameters in each panel are (left) $Fr = 2.47$, $Re_N^* = 1.25$; (right), $Fr = 0.77$, $Re_N^* = 70.73$. $Re_N = 140 \pm 6$ in both cases. The field of view in each snapshot is 8×800 (mm^2) located 24 (mm) below the gate valve. The bottom row plots the contours of depth averaged concentration profile diagrams (corresponding to the panels in the top row).

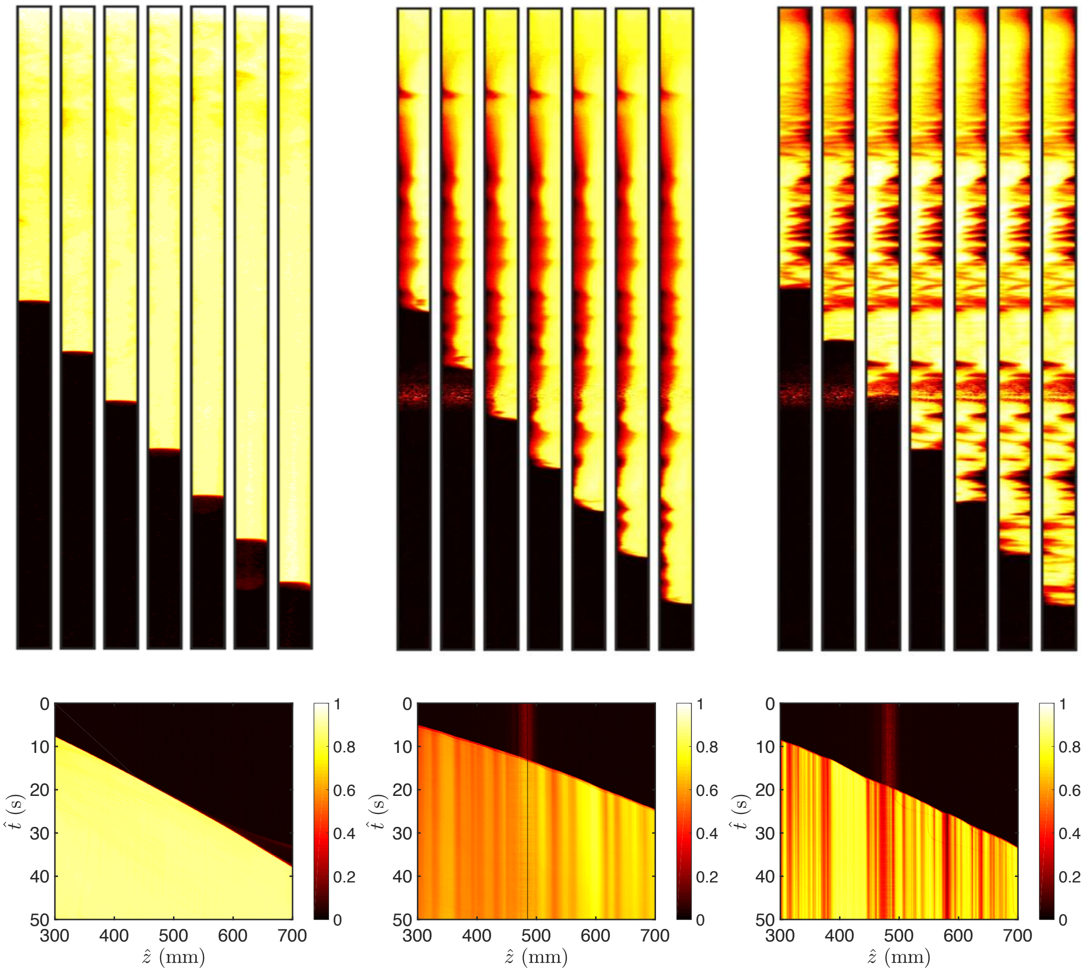

FIGURE 3.5 – The top row shows three panels each containing a sequence of experimental images, showing from left to right smooth, wavy and corrugated static residual layers. The flow parameters in each panel are (left) $Fr = 0.57$, $Re_N^* = 0.034$; (middle) $Fr = 1.82$, $Re_N^* = 0.040$; (right) $Fr = 1.73$, $Re_N^* = 0.008$. $Re_N = 103 \pm 5$ in all cases. The field of view in each snapshot is 8×800 (mm^2) located 24 (mm) below the gate valve. The bottom row plots the contours of depth averaged concentration profile diagrams (corresponding to the panels in the top row).

diagrams of the depth averaged concentration profiles are presented. For all these flows, the average concentration along the pipe remains almost constant with respect to the time and position. In addition, the interface between the displaced and displacing fluids is sharp. In the smooth case, the residual layers of the displaced fluid on the pipe wall are relatively uniform and they present very low amplitude variations. The boundary between two fluids in the spatiotemporal diagram seems to be also smooth (and appears to be nearly linear). In the wavy and corrugated sub-regimes, however, there are visible vertical streaks in the spatiotemporal diagrams, indicating the non-uniformity of the residual layers. The former is identified by medium amplitude variations in the residual layers and more or less uniformity (or linearity) of the boundary between two fluids in the spatiotemporal diagram. The latter is characterised by large amplitude variations in the residual layer and non-uniformity (and non-linearity) of the boundary between two fluids in the spatiotemporal diagram (see (58) for more details).

There are also secondary flow features in our displacements, one of which is the observation of *central* and *periphery* displacement forms (Fig. 3.6), which may typically occur near the front position. Most of our experiments exhibit central displacement flows in which the displacing fluid front prefers to flow into the displaced one towards the pipe centre (see Fig. 3.6a). Therefore, the displacing fluid (as an inner layer) flows within the displaced one (as an outer layer). However, there are also several experiments showing that when the density difference between the fluids increases (i.e. creating stronger buoyancy forces), a periphery displacement may occur, in which the displacing fluid front at least locally advances around the displaced fluid, producing an outer Newtonian layer and an inner yield stress fluid layer (see Fig. 3.6b). The periphery displacing fluid front pushes forward around the displaced fluid and appears to advance downward faster than the bulk of the flow. The flow pattern is local and the displacement can still leave behind a wall residual layer that is typically uniform and thin. Therefore, it may be reasonable to classify these periphery displacement flows as a branch of the smooth residual layer sub-regime.

3.4.2 Regime classifications

In order to better understand various flow regimes and patterns observed in our experiments, we have analysed in detail a large number of displacements (roughly 200 experiments) and we have attempted to describe them versus the dimensionless groups that govern the flow. Fig. 3.7 classifies our main flow regimes discussed so far. One of the main observations is the appearance of static and moving residual layers. Perhaps intuitively, our experiments show that by increasing the yield stress, displacement flows represent residual layers that are fully static. Therefore, to quantify this aspect, we have analysed in detail the variation of the concentration field for each experiment and we have succeeded to classify static and moving residual layers in the plane of B_N and χ, as depicted in Fig. 3.7a. This figure shows that the occurrence of

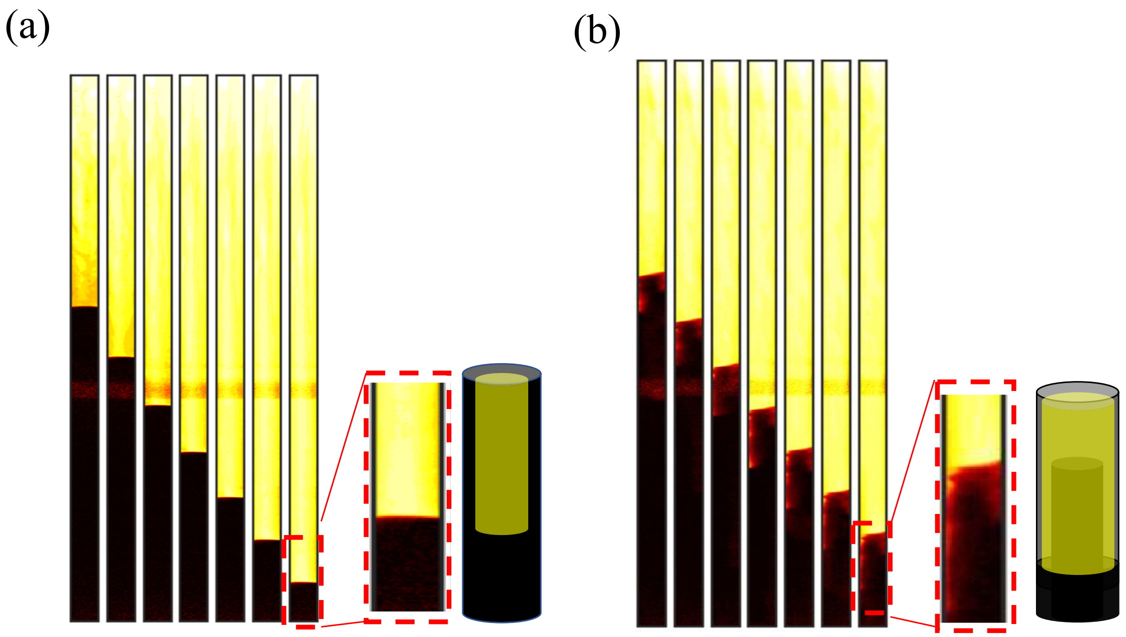

Figure 3.6 – Sequence of experimental images, illustrating (a) a central displacement and (b) a periphery displacement. A close up view and a schematic of the displacement front is included in each subfigure. The field of view in each snapshot is 8×800 (mm^2) located 24 (mm) below the gate valve. The flow parameters are (a) $Re_N = 662$, $Fr = 3.8$, $Re_N^* = 0.33$; (b) $Re_N = 509$, $Fr = 1.72$, $Re_N^* = 0.81$.

static and residual layers highly depends on B_N and it is almost independent of χ (at least for smaller values of χ), which highlights the importance of the ratio of the yield to viscous stress in the removal of the displaced layer. Our experiments reveal that the transition roughly occurs at $B_N \approx 100$, which is in agreement with the prediction of the analytical lubrication model (marked by the dashed line in Fig. 3.7a) that will be explained later in the text. For $B_N < 100$ the viscous stress is dominant and the residual layer regimes are moving (so they are removable), whereas for $B_N \gtrsim 100$, the yield stress is dominant and thus static residual layers are observed.

Within the class of moving residual layers, two sub-regimes termed nearly-stable and unstable displacements are observed, which we succeed to classify in the plane of Re_N^* and χ in Fig. 3.7b. The results show that the transition between these sub-regimes is mainly governed by χ, which represents the ratio of buoyant to viscous stresses, occurring at $\chi_c \approx 120$, more or

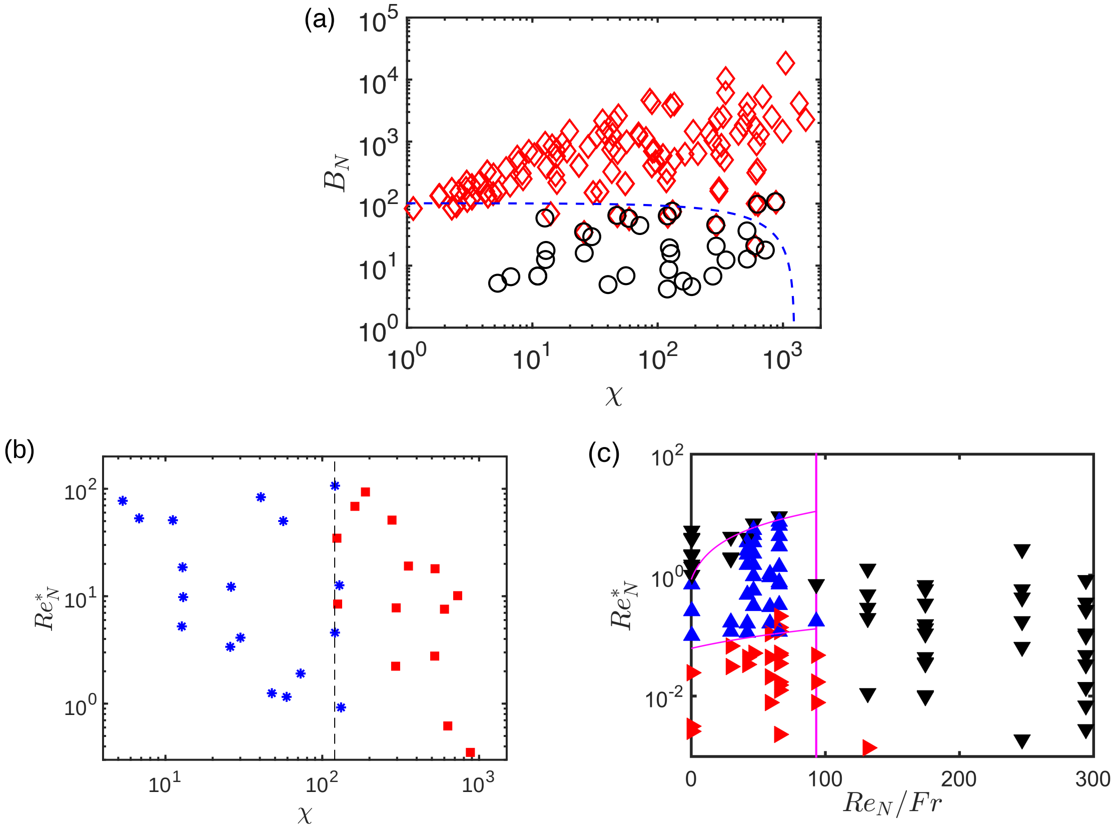

FIGURE 3.7 – Regime classification. (a) Main regimes in the plane of B_N versus χ for all experiments: moving and stationary residual layers are marked by (◇) and (○), respectively. Dashed line shows the transition predicted by the lubrication model ($B_N = 101.325 - 0.0819\chi$). (b) Sub-regimes within moving residual layer flows in the plane of Re_N^* versus χ: nearly-stable flows ($\ast$) and unstable flows (■). Vertical dashed line represents the transition at $\chi \approx 120$. (c) Sub-regimes within stationary residual layer flows in the plane of Re_N^* versus Re_N/Fr: smooth (▼), the wavy (▲), and the corrugated (►) residual layers. Dashed lines represent the wavy-smooth and corrugated-way transitions at small Re_N/Fr. As Re_N/Fr increases, the vertical dashed line marks a secondary transition to smooth residual layers $Re_N/Fr \approx 93$.

less independent of Re^*_N and of various combinations of the other dimensionless groups (not shown for brevity). Our χ_c can be compared with the findings of Zare *et al.* (21) who studied buoyant miscible displacement flows of a Bingham fluid by a Newtonian fluid along a vertical 2D plane-channel. They found that the transition between stable and unstable flow regimes is mainly a function of χ, and varies in the range of 40 and 220, which is in qualitative agreement with our results.

Within the class of static residual layers in our buoyant displacements (i.e. $B_N \gtrsim 100$), various interesting flow features are observed in terms of the phenomenological behaviours of these layers. As mentioned, Moisés *et al.* (58) studied these flows at the limit of zero density difference in a horizontal pipe and classified smooth, wavy and corrugated residual layers versus a Reynolds number similar to our Re^*_N, which includes the yield stress effects of the displaced fluid. Therefore, a reasonable regime map to analyse the effects of gradually increasing the density difference on static residual layers naturally involves Re^*_N versus another relevant dimensionless parameter to represent the significance of buoyancy. This parameter turns out to be Re_N/Fr, which depends on the density difference, and it is independent of the imposed flow velocity. Fig. 3.7c plots the experimental datapoints of smooth, wavy and corrugated static residual layers in the plane of Re^*_N and Re_N/Fr, wherein various transitions can be recognized. Let us first concentrate on the effects of increasing Re_N/Fr on the transition between the sub-regimes while Re_N/Fr is small. For Re_N/Fr=0, we already found that the critical values of $Re^*_N \approx 0.062$ and ≈ 0.849 identify the corrugated-wavy and wavy-smooth transitions, respectively. When Re_N/Fr gradually increases from zero, we may expect that these transition values are simply the leading order terms in an expansion of Re^*_N with respect to small Re_N/Fr and assume

$$Re^*_N = g\left(Re_N/Fr\right) \approx g\left(0\right) + g'\left(0\right) Re_N/Fr + ..., \tag{3.9}$$

where g indicates that the critical Re^*_N is a function of Re_N/Fr. Using this coarse approach, we are able to experimentally find that the corrugated-wavy transition follows

$$Re^*_N \approx 0.062 + 0.0007 Re_N/Fr + ...,$$

and that the wavy-smooth transition follows

$$Re^*_N \approx 0.849 + 0.1127 Re_N/Fr + ...,$$

which are valid for small Re_N/Fr, as also seen in Fig. 3.7c. Note that these are leading order approximations to the corrugated-wavy and wavy-smooth transitions in buoyant displacements. However, as Re_N/Fr increases, the assumptions for the expansion above break down and, expectedly, the transition between the residual layer regimes cannot be predicted by the relations provided. In fact, Fig. 3.7c shows that when $Re_N/Fr \gtrsim O(10^2)$, implying that buoyancy forces become significant, the residual layers are all smooth, independent of the value of Re^*_N. This transition can be roughly represented by $Re_N/Fr \approx 93$.

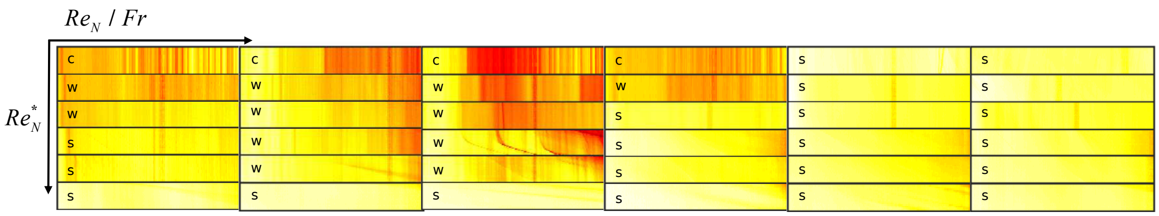

FIGURE 3.8 – Panorama of spatiotemporal diagrams at long times for various Re/Fr and Re_N^*. Each small image shows a spatiotemporal diagram over 800 (mm) of the pipe length (horizontal axis) over the last 3 seconds of each experiment (vertical axis). On each image, corrugated, wavy and smooth residual layers are marked by c, w and s. From left to right, $Re_N/Fr = [0, 46.5, 65.8, 93.1, 174.3, 294.6]$. From top to bottom, $Re_N^* = [0.04, 0.25, 0.80, 2.47, 3.53, 5.58]$.

An explanation for the behaviours observed is that when Re_N/Fr is small (weak buoyancy), changes in the ratio of inertial to effective viscous forces captured through Re_N^* (which include the yield stress) are important in characterising the form of the static residual layers, i.e. corrugated, way and smooth. However, when Re_N/Fr is large, the buoyancy forces are strong and, thus, dominate the flow. Therefore, the existence of the static layers becomes independent of the yield stress and inertial effects. These findings emphasize that the static residual layers have a complex trend versus the flow parameters. To better understand the flow behaviours in Fig. 3.7c and visualize how the variations in Re_N^* and Re_N/Fr modify the flow regimes, Fig. 3.8 illustrates a panorama of spatiotemporal diagrams at long times for various increasing the values of the Re_N/Fr and Re_N^*. As evident, increasing Re_N/Fr and Re_N^* are both in favour of transitioning to smooth static residual layers.

To more quantitatively demonstrate the effects of the flow parameters on the waviness of the static residual layers, we have used a sum of sines (SoS) model to find the fluctuation amplitudes in the depth averaged concentration profiles ($\bar{\bar{C}}_{xy}(z)$) along the pipe at long times (when the front reaches the pipe end). The SoS model is a popular method to estimate a given function using a sum of sinusoidal harmonics, to extract the relevant amplitudes and frequencies. In order to extract the local fluctuations in $\bar{\bar{C}}_{xy}(z)$, let us rely on the following double SoS application:

$$\bar{\bar{C}}_{xy}(z) \approx \sum_{i=1}^{n_1} \mathcal{A}_{1,i} \sin(\mathcal{B}_{1,i} z + \mathcal{C}_{1,i}) \equiv C_{1,\text{fit}}, \tag{3.10}$$

$$\bar{\bar{C}}_{xy}(z) - C_{1,\text{fit}} \approx \sum_{i=1}^{n_2} \mathcal{A}_{2,i} \sin(\mathcal{B}_{2,i} z + \mathcal{C}_{2,i}) \equiv C_{2,\text{fit}}, \tag{3.11}$$

where $\mathcal{A}_{j,i}$ is the amplitude, $\mathcal{B}_{j,i}$ the frequency, $\mathcal{C}_{j,i}$ the phase constant for each sine wave term, n_j the number of terms in the series, and $j = 1, 2$. In our case, for simplicity, we take $n_j = 2$. $C_{1,\text{fit}}$ and $C_{2,\text{fit}}$ represent the fitted curves in the first and second application of the SoS method, respectively. The former could be a qualitative representative for the overall shape

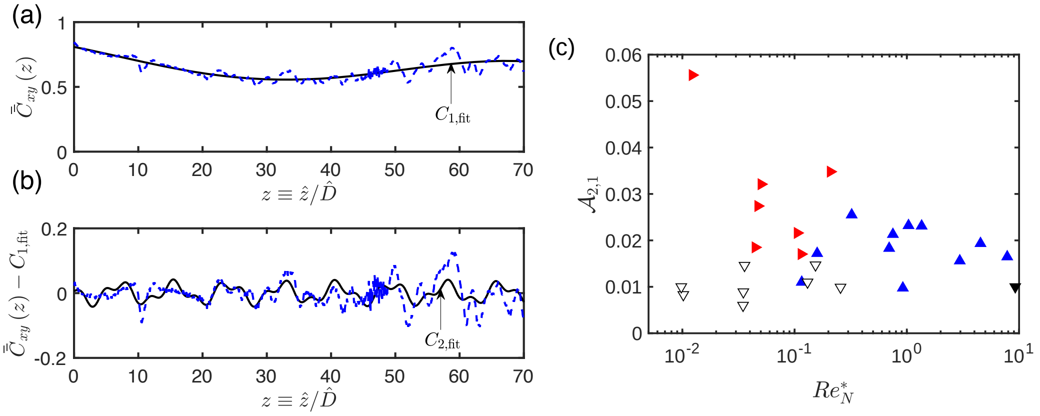

FIGURE 3.9 – (a) An example of the depth averaged concentration profile, $\bar{\bar{C}}_{xy}(z)$ (blue dashed line), and the fitted curve through the sum of sines model, $C_{1,\mathrm{fit}}$ (dark solid line), at $Re_N/Fr = 58.9$ and $Re_N^* = 0.04$. (b) $\bar{\bar{C}}_{xy}(z) - C_{1,\mathrm{fit}}$ (blue dashed line), both from subfigure a, and the fitted curve through re-applying the sum of sines model to find $C_{2,\mathrm{fit}}$ (solid line). (c) $\mathcal{A}_{2,1}$ versus Re_N^* at $Re_N/Fr = 58.9$ (filled symbols) and $Re_N/Fr = 174.3$ (hollow symbol): smooth (▼, ▽), wavy (▲), and corrugated (►) residual layers. (For interpretation of the references to colour in this figure legend, the reader is referred to the web version of this article.)

of the mean residual layer values and the latter could represent the relative fluctuations. The leading order amplitude fluctuations in $\bar{\bar{C}}_{xy}(z)$ can be found through analysing $\mathcal{A}_{2,1}$.

Fig. 3.9a shows the variation of the depth averaged concentration profile along the pipe (blue dashed line) and the fitted curve through equation (3.11) (black solid line). The fitted curve reasonably presents the overall shape of the depth average concentration profile. To ensure that this fit is appropriate, we have also verified statical parameters such as the sum of squared errors and the adjusted R-square, finding them to be close to zero and one, respectively. Fig. 3.9b shows the results of applying equation (3.11) (using the results obtained from Fig. 3.9a), demonstrating that $C_{2,\mathrm{fit}}$ reasonably approximates the fluctuations in the depth averaged concentration.

Fig. 3.9c plots the variation of $\mathcal{A}_{2,1}$ versus Re_N^*, for two fixed values of $Re_N/Fr = 58.9$ and $Re_N/Fr = 174.3$. As can be seen, when Re_N/Fr is smaller than the critical values of 93, increasing Re_N^* results in significantly decreasing $\mathcal{A}_{2,1}$ and transitioning between the corrugated, wavy and smooth static residual layers (this implies that at large values of the yield stress, the residual layers are more non-uniform and thus the concentration fluctuation is larger). However, when Re_N/Fr is larger than the critical value of ~ 93 (found earlier), $\mathcal{A}_{2,1}$ remains small and does not much vary with increasing Re_N^*: the static residual layers become smooth when $Re_N/Fr \gtrsim 93$.

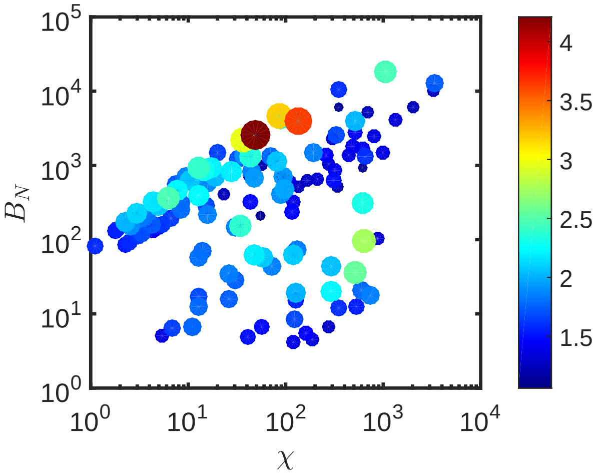

FIGURE 3.10 – V_f in the plane of B_N and χ. The values of V_f are marked by the symbol size and colours.

3.4.3 Front velocity

One of the crucial flow features frequently studied in displacement flows is the front velocity of the advancing displacing fluid into the displaced one, since in particular, this velocity can provide a measure of the overall displacement efficiency. If the front velocity is small, we may expect that the displacement is efficient. To consistently measure the front velocity at long times ($V_f = \hat{V}_f/\hat{V}_0$), we rely on the experimental approach discussed in Amiri *et al.* (55). Fig. 3.10 presents the variation of V_f in the plane of B_N and χ for a large number of experiments. This figure reveals that the front velocities (and therefore the displacement flow efficiency) are strongly affected by changes in B_N; in particular, in most cases, increasing B_N results in increasing the displacing fluid penetration velocity. Also, the datapoints with moderate values of χ seem to have the largest V_f. Nevertheless, these trends do not apply to all the datapoints.

In our experiments, we are generally dealing with fluid flows for which the imposed flow Reynolds number is not too high (i.e. the imposed flow is in the laminar regime). Therefore, in order to predict the front velocity, as a first step, it may be natural to develop a lubrication type model and evaluate if this model could be used to predict the front velocity at long times, as well as several other important flow features. This will be the focus in the next section.

3.5 Analytical model

In this section, we will provide an analytical lubrication model to evaluate whether it can provide predictions about some of the flow behaviour. In our experiments, we have observed the appearance of two interfacial flow patterns that are phenomenologically different (and

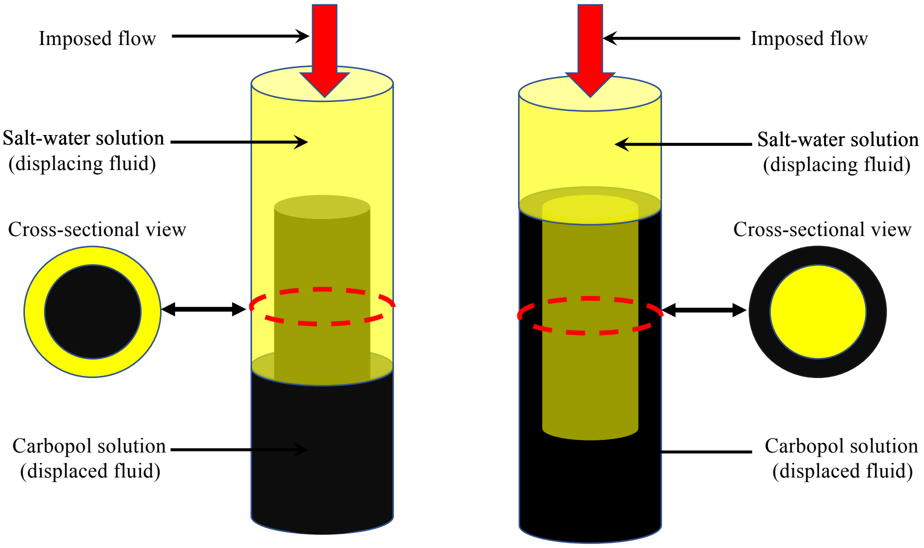

FIGURE 3.11 – Schematic views of the idealized displacements considered in the analytical model: periphery (left) and central (right).

therefore require different models), i.e. a central displacement and a periphery displacement. Although these fluid flow cases are quite complex and perhaps involve several fluid layers, for simplicity we define and analyse two highly idealized displacement cases, according to the illustrations in Fig. 3.11. The right schematic image shows a central displacement, meaning that the displacing fluid tends to move into the displaced fluid along the pipe centre line, and the left schematic image depicts a periphery displacement, with the displacing fluid moving closer to the pipe wall, leaving the displaced fluid in the channel centre. Note that although these are highly simplified, idealized configurations for modelling purposes, they are still useful to gain fundamental understanding about the flow dynamics.

Starting from the governing equations explained in § 3.2, to develop our simplified model, let us rely on a cylindrical coordinate system of (r, θ, z) and $\mathbf{u} = (w, v, u)$. Assuming an axisymmetric flow condition, we can reduce the problem to $(v(r, z), u(r, z))$ for which the leading order equations for the heavy and light fluids are

$$0 = f + \frac{1}{r}\frac{\partial}{\partial r}\left(r\tau_{H,rz}\right), \tag{3.12}$$

$$0 = f - \chi + \frac{1}{r}\frac{\partial}{\partial r}\left(r\tau_{L,rz}\right), \tag{3.13}$$

respectively, where $f = -\frac{\partial p}{\partial z} - \frac{\chi}{2}$ and the incompressibility condition for each layer

$$\frac{1}{r}\frac{\partial\left(rv\right)}{\partial r} + \frac{\partial u}{\partial z} = 0. \tag{3.14}$$

Note that $\frac{\partial p}{\partial r} = 0$ in the leading order equations.

For simplicity, we consider a Bingham version of the Herschel-Bulkley model (so $n = 1$), for which the simplified constitutive equation at the leading order for the light fluid can be written as

$$\frac{\partial u}{\partial r} = 0 \quad \Leftrightarrow \quad |\tau_{L,rz}| \leq B_N, \tag{3.15}$$

$$\tau_{L,rz} = \left[m + \frac{B_N}{\left|\frac{\partial u}{\partial r}\right|}\right]\frac{\partial u}{\partial r} \quad \Leftrightarrow \quad |\tau_{L,rz}| > B_N, \tag{3.16}$$

while the heavy fluid simply obeys the Newton's viscosity law:

$$\tau_{H,rz} = \frac{\partial u}{\partial r}. \tag{3.17}$$

Regarding the boundary conditions, at the pipe wall we have $\mathbf{u} = 0$ and at the interface we consider that both velocities and shear stresses are continuous. At the pipe centre we also apply the symmetric condition. Since the flow rate is constant, we also have an additional flow constraint

$$\frac{1}{4} = \int_0^{1/2} 2rudr, \tag{3.18}$$

which has to be satisfied by the solution. It can be shown that the interface evolves following

$$\frac{\partial \alpha}{\partial t} + \frac{\partial q}{\partial z} = 0, \tag{3.19}$$

where $\alpha = r_i^2$ (with $r_i \in [0, 1/2]$) is the area fraction occupied by the inner layer fluid and q is the flux function defined as

$$q = \int_0^{r_i} 2rudr, \tag{3.20}$$

where r_i is the radial position of the interface.

3.5.1 Central displacement

In the central displacement, the displacing fingers move into the displaced fluid towards the pipe centreline. In a theoretical ground, in terms of the velocity profiles and the appearance of plugs within the yield-stress fluid, there are in particular six different cases that may appear, as will be discussed below. Before we proceed to explain these cases in detail, let us first denote the wall and interfacial shear stresses as τ_w and τ_i, respectively, and define the following useful radii:

$$\begin{cases} r_1 = \frac{\sqrt{B_N^2 + {r_i}^2 \chi (\chi - f)} - B_N}{\chi - f}, \\ r_2 = \frac{\sqrt{B_N^2 + {r_i}^2 \chi \, (\chi - f)} + B_N}{|\chi - f|}, \end{cases} \tag{3.21}$$

which will simplify the presentation of the results for each case in the following subsections. These are simply the solutions of a quadratic equation that is related to the radii of the yield surfaces. For clarification, simply consider a multilayer region in a displacement case with moderate dimensionless parameter ranges where it is assumed to have a plug region within the displaced layer. This implies that there are two radii (e.g. r_1 and r_2) corresponding to two yield surfaces, with the difference between the radii ($r_2 - r_1$) being the thickness of the unyielded plug region. In this situation, knowing that at the boundary of the unyielded region the dimensionless stress is equal to B_N, we can solve the equations and obtain these two radii. Depending on the sign of the interfacial stress, equation 3.21 presents these two radii in a general form. Of course, there are also other possible cases, for example when there are no yield surfaces, as discussed below.

Case 1: $-\tau_w > B_N$ **&** $-\tau_i > B_N$

For case 1, f is simply calculated as

$$f = \frac{48\,{r_i}^4 \chi - 128\,{r_i}^3 B_N - 24\,\chi\,{r_i}^2 + 16\,B_N + 3\,\chi + 96\,m}{3\,(16\,{r_i}^4 m - 16\,{r_i}^4 + 1)}. \tag{3.22}$$

Also, the flux function becomes

$$q = \frac{(4\,\chi + (2\,m - 4)\,f)\,{r_i}^4 - 8\,{r_i}^4 \chi \,\ln{(2r_i)} + 16\,{r_i}^3 B_N + (-8\,B_N + f - \chi)\,{r_i}^2}{16m}, \tag{3.23}$$

and the velocity profiles are

$$\begin{cases} u_H = \frac{(4\,\chi + (4\,m - 4)\,f){r_i}^2 - 8\,\chi\,{r_i}^2 \ln(2r_i) + 16\,r_i\,B_N - 4\,fmr^2 - 8\,B_N + f - \chi}{16m}, & 0 \le r \le r_i \\ u_L = \frac{\left(4\,r^2 - 1\right)\chi - 8\,\chi\,{r_i}^2 \ln(2r) - 4\,fr^2 + 16\,B_N\,r - 8\,B_N + f}{16m}, & r_i < r \le 1 \end{cases} \tag{3.24}$$

where subscripts H and L refer to the heavy and light layers, here and elsewhere. Figs. 3.12a and 3.13a show an example of the variation of the shear stress and the velocity profile, versus r, respectively, for case 1.

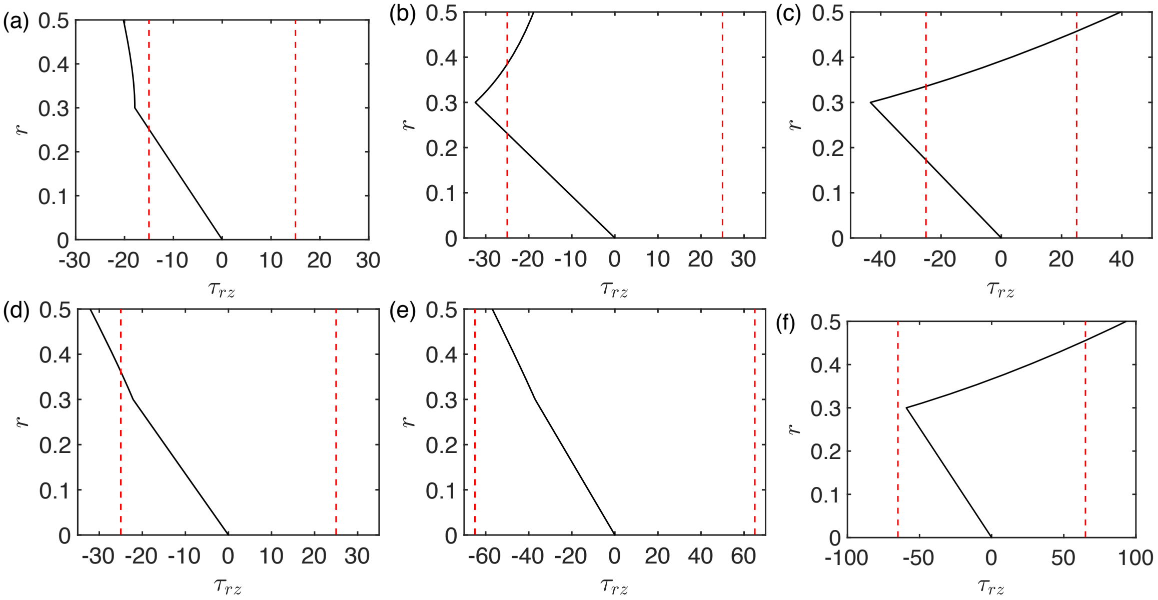

FIGURE 3.12 – Variation of the shear stress versus radius for central displacements with $m = 1$ and $r_i = 0.3$: (a) Case 1: $\chi = 60$ & $B_N = 15$; (b) Case 2: $\chi = 220$ & $B_N = 25$; (c) Case 3: $\chi = 700$ & $B_N = 25$; (d) Case 4: $\chi = 30$ & $B_N = 25$; (e) Case 5: $\chi = 30$ & $B_N = 65$; (f) Case 6: $\chi = 1200$ & $B_N = 65$. The dashed lines mark $\pm B_N$ for each case.

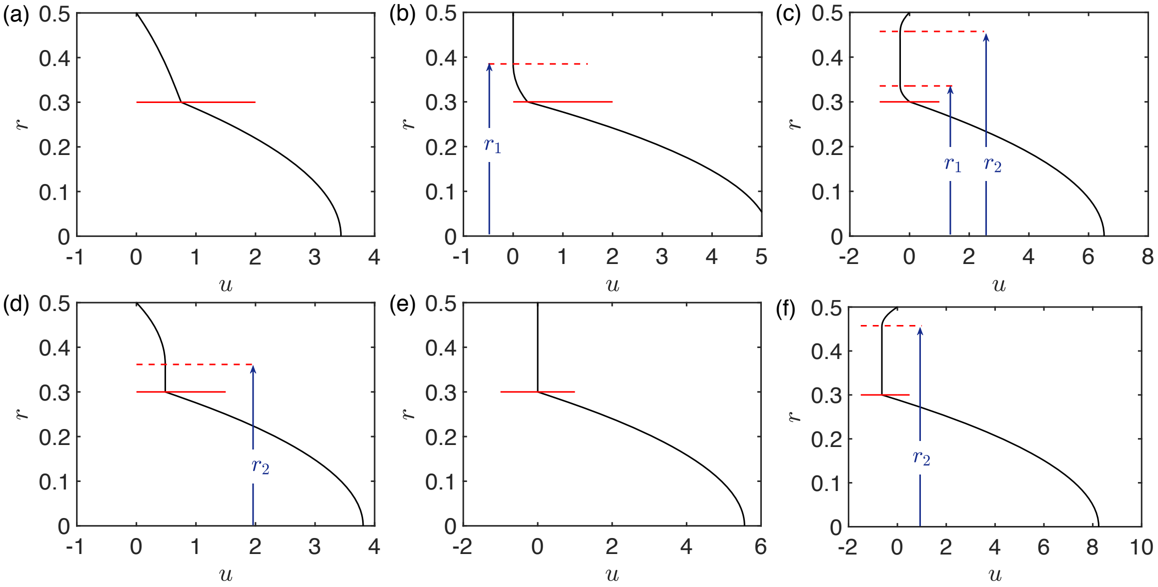

FIGURE 3.13 – Model results: Variation of the velocity profiles versus radius for the corresponding cases in Fig. 3.12. The interface position is marked by the thick horizontal lines. r_1 and r_2 are marked by arrows and dashed lines.

Case 2: $|\tau_w| \leq B_N$ **&** $-\tau_i > B_N$

For case 2, f can be obtained using the following equation:

$$\frac{1}{4} = \frac{3\left((m-1)\,f - \chi\right) {r_i}^4 + 8\,{r_i}^3 B_N + 6\,{r_i}^2 \chi\, {r_1}^2 + 3\left(f - \chi\right) {r_1}^4 - 8\,{r_1}^3 B_N}{24m}, \tag{3.25}$$

in which r_1 must be replaced by the relation given in (3.21). The flux function is

$$q = \frac{4\,{r_i}^4 \chi \, \ln\left(\frac{r_1}{r_i}\right) + \left(2\,\chi + (m-2)\,f\right) {r_i}^4 + 8\,{r_i}^3 B_N + \left(2\,f\,{r_1}^2 - 2\,\chi\,{r_1}^2 - 8\,B_N\,r_1\right) {r_i}^2}{8m}, \tag{3.26}$$

and the velocity profiles are

$$\begin{cases} u_H = \frac{2\,\chi\,{r_i}^2 \ln\left(\frac{r_1}{r_i}\right) + (\chi + (m-1) f) {r_i}^2 + 4\,B_N\,r_i - \chi\,{r_1}^2 + \left({r_1}^2 - m r^2\right) f - 4\,B_N\,r_1}{4m}, & 0 \leq r \leq r_i \\ u_L = \frac{2\,\chi\,{r_i}^2 \ln\left(\frac{r_1}{r}\right) + \chi\,r^2 - \chi\,{r_1}^2 - f\,r^2 + f\,{r_1}^2 + 4\,B_N\,r - 4\,B_N\,r_1}{4m}, & r_i < r < r_1 \\ u_L = 0. & r_1 \leq r \leq 1 \end{cases} \tag{3.27}$$

A flow, in this case, involves a static residual wall layer with the thickness of $1 - r_1$ since $u_L = 0$ for $r_1 \leq r \leq 1$. Figs. 3.12b and 3.13b show an example of the variation of the shear stress and the velocity profile, versus r, respectively, for case 2.

Case 3: $\tau_w > B_N$ **&** $-\tau_i > B_N$

For case 3, f can be obtained using the following equation:

$$\begin{aligned} \frac{1}{4} \;=\;& \frac{\left(48\,{r_2}^4 - 48\,{r_i}^4 + \left(96\,{r_1}^2 - 96\,{r_2}^2 + 24\right) {r_i}^2 - 48\,{r_1}^4 - 3\right) \chi}{384\,m} \\ +\;& \frac{48\,f\,(m-1)\,{r_i}^4 + 128\,{r_i}^3 B_N + \left(48\,{r_1}^4 - 48\,{r_2}^4 + 3\right) f - 128\,B_N\left({r_2}^3 + {r_1}^3 - \frac{1}{8}\right)}{384\,m}, \end{aligned} \tag{3.28}$$

where r_1 and r_2 must be replaced by the relations given in (3.21). The flux function is

$$\begin{aligned} q \;=\;& \frac{8\,{r_i}^4 \chi \, \ln\left(\frac{r_1}{2 r_2 r_i}\right) + \left(4\,\chi + 2\,(m-2)\,f\right) {r_i}^4 + 16\,{r_i}^3 B_N}{16m} \\ +\;& \frac{\left(\left(4\,{r_2}^2 - 4\,{r_1}^2 - 1\right) \chi + \left(4\,{r_1}^2 - 4\,{r_2}^2 + 1\right) f - 16\,B_N\left(r_2 + r_1 - \frac{1}{2}\right)\right) {r_i}^2}{16m}, \end{aligned} \tag{3.29}$$

and the velocity profiles are

$$\begin{cases} u_H = \frac{8\,\chi\,{r_i}^2 \ln\left(\frac{r_1}{2 r_2 r_i}\right) + \left(4\,{r_2}^2 + 4\,{r_i}^2 - 4\,{r_1}^2 - 1\right)(\chi - f) + 4mf\left({r_i}^2 - r^2\right) + 16\,B_N\,r_i - 16\,B_N\left(r_2 + r_1 - \frac{1}{2}\right)}{16m}, & 0 \leq r \leq r_i \\ u_L = \frac{8\,\chi\,{r_i}^2 \ln\left(\frac{r_1}{2 r_2 r_i}\right) + \left(4\,r^2 + 4\,{r_2}^2 - 4\,{r_1}^2 - 1\right)\chi + (16\,r - 16\,r_2 - 16\,r_1 + 8) B_N - 4\left(r^2 + {r_2}^2 - {r_1}^2 - \frac{1}{4}\right) f}{16m}, & r_i < r < r_1 \\ u_L = \frac{\left(4\,{r_2}^2 - 1\right)\chi - 8\,\chi\,{r_i}^2 \ln(2 r_2) - 4 f {r_2}^2 - 16\,B_N\,r_2 + 8\,B_N + f}{16m}, & r_1 \leq r \leq r_2 \\ u_L = \frac{\left(4\,r^2 - 1\right)\chi - 8\,\chi\,{r_i}^2 \ln(2r) - 4\,f r^2 - 16\,B_N\,r + 8\,B_N + f}{16m}. & r_2 < r \leq 1 \end{cases} \tag{3.30}$$

Figs. 3.12c and 3.13c show an example of the variation of the shear stress and the velocity profile, versus r, respectively, for case 3.

Case 4: $-\tau_w > B_N$ **&** $-\tau_i \le B_N$

For case 4, f can be obtained using the following equation:

$$\frac{1}{4} = \frac{\left(48\, {r_2}^4 + 24\, {r_i}^2 - 96\, {r_i}^2 {r_2}^2 - 3\right)\chi + 48\, f\, {r_i}^4 m - 48\, f\, {r_2}^4 + 128\, B_N\, {r_2}^3 - 16\, B_N + 3\, f}{384\, m}, \tag{3.31}$$

where r_2 must be replaced by the relation given in (3.21). The flux function becomes

$$q = \frac{{r_i}^2\left(2\, f\, {r_i}^2 m + 4\, \chi\, {r_2}^2 - 4\, f\, {r_2}^2 + 16\, B_N\, r_2 - 8\, B_N - \chi + f\right) - 8\, {r_i}^4 \chi\, \ln\left(2 r_2\right)}{16m}, \tag{3.32}$$

and the velocity profiles are

$$\begin{cases} u_H = \frac{4\, f\, {r_i}^2 m - 8\, \chi\, {r_i}^2 \ln(2r_2) - 4\, f\, m\, r^2 + 4\, \chi\, {r_2}^2 - 4\, f\, {r_2}^2 + 16\, B_N\, r_2 - 8\, B_N - \chi + f}{16m}, & 0 \le r \le r_i \\ u_L = \frac{\left(4\, {r_2}^2 - 1\right)\chi - 8\, \chi\, {r_i}^2 \ln(2r_2) - 4\, f\, {r_2}^2 + 16\, B_N\, r_2 - 8\, B_N + f}{16m}, & r_i < r \le r_2 \\ u_L = \frac{\left(4\, r^2 - 1\right)\chi - 8\, \chi\, {r_i}^2 \ln(2r) - 4\, f\, r^2 + 16\, B_N\, r - 8\, B_N + f}{16m}. & r_2 < r \le 1 \end{cases} \tag{3.33}$$

Figs. 3.12d and 3.13d show an example of the variation of the shear stress and the velocity profile, versus r, respectively, for case 4.

Case 5: $|\tau_w| \le B_N$ **&** $-\tau_i \le B_N$

For case 5, the light layer is fully static and therefore f, q and velocity profiles are as follows:

$$f = \frac{2}{{r_i}^4}, \tag{3.34}$$

$$q = \frac{1}{4}, \tag{3.35}$$

$$\begin{cases} u_H = \frac{{r_i}^2 - r^2}{2{r_i}^4}, & 0 \le r \le r_i \\ u_L = 0. & r_i < r \le 1 \end{cases} \tag{3.36}$$

Figs. 3.12e and 3.13e show an example of the variation of the shear stress and the velocity profile, versus r, respectively, for case 5.

Case 6: $\tau_w > B_N$ **&** $-\tau_i \le B_N$

For case 6, f can be obtained using the following equation:

$$\frac{1}{4} = \frac{\left(48\, {r_2}^4 - 96\, {r_i}^2 {r_2}^2 + 24\, {r_i}^2 - 3\right)\chi + 48\, f\, {r_i}^4 m - 48\, f\, {r_2}^4 - 128\, B_N\, {r_2}^3 + 16\, B_N + 3\, f}{384\, m}, \tag{3.37}$$

where r_2 must be replaced by the relation given in (3.21). The flux function becomes

$$q = \frac{{r_i}^2\left(2\, f\, {r_i}^2 m + 4\, \chi\, {r_2}^2 - 4\, f {r_2}^2 - 16\, B_N r_2 + 8\, B_N - \chi + f\right) - 8\, {r_i}^4 \chi\, \ln\left(2 r_2\right)}{16m}, \tag{3.38}$$

and the velocity profiles are

$$\begin{cases} u_H = \frac{4\,f\,{r_i}^2 m - 8\,\chi\,{r_i}^2 \ln(2r_2) - 4\,f\,m\,r^2 + 4\,\chi\,{r_2}^2 - 4\,f\,{r_2}^2 - 16\,B_N\,r_2 + 8\,B_N - \chi + f}{16m}, & 0 \leq r \leq r_i \\ u_L = \frac{\left(4\,{r_2}^2 - 1\right)\chi - 8\,\chi\,{r_i}^2 \ln(2r_2) - 4\,f\,{r_2}^2 - 16\,B_N\,r_2 + 8\,B_N + f}{16m}, & r_i < r \leq r_2 \\ u_L = \frac{\left(4\,r^2 - 1\right)\chi - 8\,\chi\,{r_i}^2 \ln(2r) - 4\,f\,r^2 - 16\,B_N\,r + 8\,B_N + f}{16m}. & r_2 < r \leq 1 \end{cases} \tag{3.39}$$

Figs. 3.12f and 3.13f show an example of the variation of the shear stress and the velocity profile, versus r, respectively, for case 6.

Finding the modified pressure gradient

For specified fluid properties and a given interface radius (r_i), the modified pressure gradient (f), is an unknown that can be found. However, since the wall and interfacial stresses also depend on f, it is not *a priori* known which displacement case and therefore which relation (e.g. among equations (3.22), (3.25), (3.28), (3.31), (3.34) and (3.37)) must be considered to find f. Therefore, to find f we have constructed a robust numerical procedure that considers all the cases and finds f through an iterative approach that combines bisection, secant, and inverse quadratic interpolation methods. After finding f, which simultaneously involves finding the appropriate displacement case (among the six cases), the flux function and the velocity profiles can be subsequently calculated using the corresponding equations.

Comparison between V_f from the model and experiments

It is natural to compare the front velocities of the central core interfacial flow, obtained from the experiments and the model. For the former, the front velocities ($V_{f,exp} = \hat{V}_{f,exp}/\hat{V}_{0,exp}$) are obtained by processing the experimental images to deliver experimental front velocities at long times for a given parameter set. For the former, the model front velocity is equivalent to the speed of an advancing interfacial shock at the front given by:

$$V_{f,model} = \frac{1}{2r_i} \frac{\partial q}{\partial r_i}\bigg|_{r_i = r_f}, \tag{3.40}$$

where r_f is the radial position of the interface at the front, which can be computed through the use of the conventional *equal areas rule*:

$$\frac{r_i}{2} \frac{\partial q}{\partial r_i}\bigg|_{r_i = r_f} = q\left(r_f\right). \tag{3.41}$$

Fig. 3.14 compares $V_{f,exp}$ and $V_{f,model}$ for increasing values of B_N. The comparison is only reasonable for small values of $B_N < 100$ (moving residual layer flows) and as B_N significantly increases the model results further deviate from the experimental ones. In order to better understand such deviation, let us look at the solution of the interface evolution equation (3.19), corresponding to the experiments illustrated in Fig. 3.3 (top row), as depicted in Fig. 3.15. The interface evolution equation is solved using a numerical shock capturing method explained

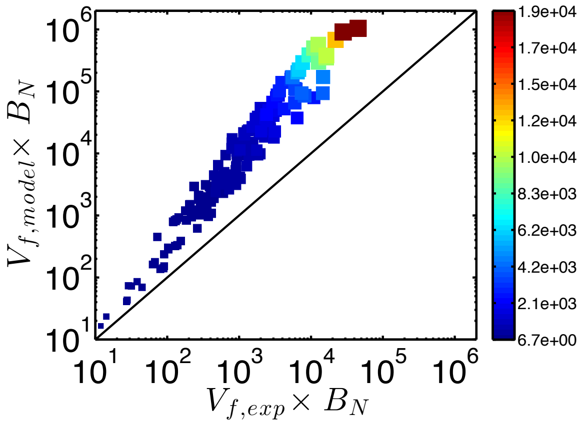

FIGURE 3.14 – Comparison between the front velocities obtained from the model and experiments. The size and colour of the square symbols represent the values of B_N. The line shows $V_{f,model} = V_{f,exp}$.

in detail in (17). As can be seen, when the yield stress is small (i.e. small B_N), the interface shape resembles that in the experiments. However, as the yield stress or B_N increases, the displacing finger becomes progressively narrower, implying that the interface front speed must increase significantly (due to the flow rate constraint). On the other hand, in our experiments of Fig. 3.3 (top row), it seems that at larger B_N the displacing fluid breaks into the Carbopol gel through frontal inertial effects which cannot be ignored. Therefore, the lubrication model is not able to provide a reasonable comparison with the experiments at large B_N.

Static residual layers at long times

Far away from the displacement front (which may include inertial effects), the flow may be expected to be in the laminar regime. In this case, the lubrication model developed can be used to shed light on the interface behaviours. In particular, using the model it is of interest to quantify whether the residual layers observed in the experiments at long times are fully static or partially static.

For central displacement and among the six distinct cases (in terms of the velocity profiles), case 2 and case 5 involve static residual wall layers (see the velocity profiles in Fig. 3.13). In the other cases, although there may be plug layers within the light layer (e.g. in cases 3, 4 and 6), the yield stress fluid layer moves forward or backward, as a whole. Therefore, these cases would not present any fully or partially static residual layers. For case 2, as we move away from the upper wall towards the pipe centre, the velocity profile within the yield stress fluid has a fully static residual layer attached to the upper wall and a slowly moving layer that reaches the interface. This implies that case 2 represents a partially static residual wall layer. For case 5, however, the residual layer is fully static throughout the yield stress layer.

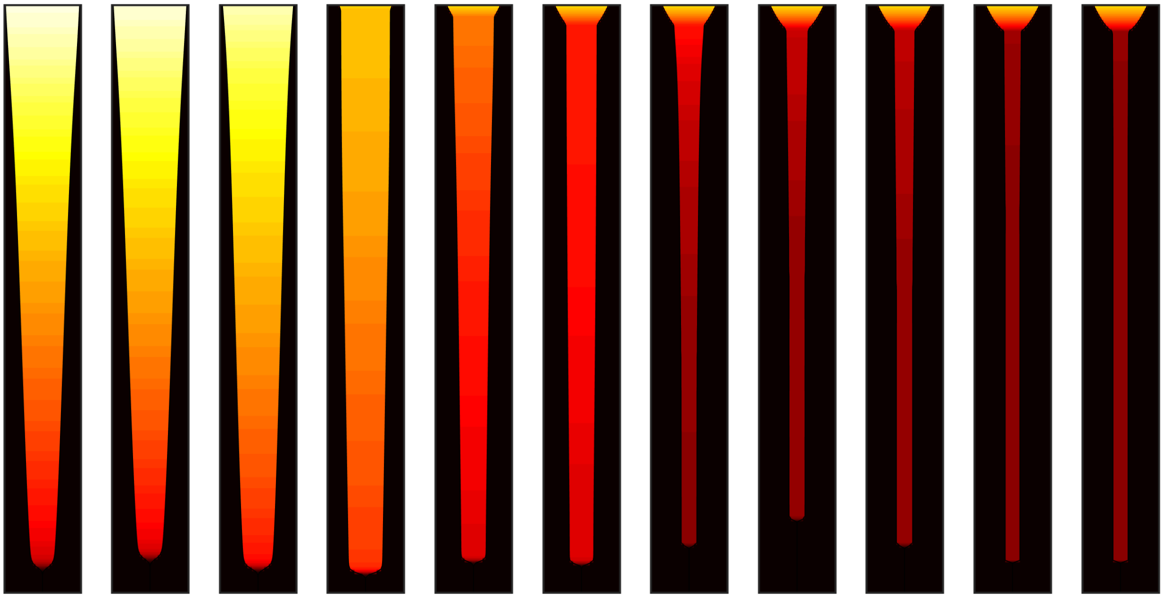

FIGURE 3.15 – Model results showing displacements obtained analytically (for $L = 10$), corresponding to the experiments with increasing the Carbopol concentrations in the top row of Fig. 3.3. The contour colours are the same those in the experimental figure.

Let us first focus on the situation in which the fluid is static throughout the displaced layer (case 5). In the spirit of case 5, depending on the values of the buoyancy number (χ), different scenarios may occur. For example, if χ is small, the shear stress is expected to remain negative and decrease throughout the light layer, implying that the largest magnitude of the shear stress is found at the pipe wall. In this case, a maximal static residual layer thickness can be calculated by satisfying $-\tau_w = B_N$. Therefore, if the layer starts to yield in this scenario, this must first occur at the pipe wall ($-\tau_w > B_N$). For moderate values of χ, the shear stress, which is always negative at the interface, will start to increase across the outer layer and it can even become positive; therefore, the largest magnitude of the shear stress will be found at the interface while the shear stress magnitude remains below the yield stress throughout the layer. Provided that the light layer starts to yield in this scenario, this must first occur at the interface ($-\tau_i > B_N$). Finally, as χ increases to large values, if the light layer yields, again this must first occur at the pipe wall albeit with a positive wall shear stress ($\tau_w > B_N$). Analysing these three scenarios for case 5 results in finding two critical buoyancy numbers:

$$\chi_{c,\text{yielded at wall}} = \frac{2}{{r_i}^4}, \tag{3.42}$$

$$\chi_{c,\text{yielded at interface}} = \frac{10}{{r_i}^4\,(1 - 4\,{r_i}^2)}. \tag{3.43}$$

Fig. 3.16a shows the variation of the critical curves of χ, explained above, versus r_i. Our experimental results are also superimposed on this plot. Based on the prediction of the model, if yielding occurs for the experimental datapoints lying below the thin line (equation (3.42)) or above the thick line (3.43), this must occur at the pipe wall: The yield stress fluid would be either washed (small χ) or move upward (large χ). On the other hand, provided that a residual wall layer is observed for these experimental datapoints, the layer is fully static and it is not partially moving. However, for the experimental datapoints that are within the two lines (i.e. thin and thick lines), if a residual wall layer is observed, it is not *a priori* known if the layer is fully static or partially moving near the interface. It would be also difficult experimentally to detect a partially moving residual throughout the interface over our long pipe. However, since a partially moving residual layer corresponds to case 2, a maximal partially static residual layer thickness can be calculated by satisfying $\tau_w = B_N$ to find the modified pressure gradient as

$$f = \chi - 4\,\chi\,{r_i}^2 - 4\,B_N. \tag{3.44}$$

Therefore, for a given flow parameter set (experimental input parameters), the values of r_i and subsequently r_1 corresponding to the maximal partially static residual wall layer thickness can be numerically calculated, as depicted in Fig. 3.16b. This figure plots theoretical curves of χ versus r_i (lines) and r_1 (dashed lines) for increasing values of B_N. A value of $m = 1$ is chosen for simplicity and illustrative purposes. The same experimental datapoints of Fig. 3.16a are also superimposed on this plot in the plane of χ and r_i. By increasing B_N, the theoretical results deviate from where the experimental results are concentrated (i.e. on average $r_i \approx 0.41$) and move towards smaller values of radii, an observation for which the interpretation is straightforward: Our experimental results at a very long time with observable residual layer do not correspond to case 2, for which the residual wall layers are only partially static, but instead, they correspond to case 5, for which the residual wall layers are fully static.

Before proceeding with our analysis to quantify residual layer behaviours at long times, it is worth clarifying two aspects in relation to Fig. 3.16. First of all, one may wonder why χ and B_N seem to be correlated in terms of the variations of the datapoints, i.e. very small/large values of χ generally (not always) correspond to very small/large values of B_N. The explanation is simple. χ and B_N are both inversely proportional to $\hat{V}_0$, which is a parameter that has one of the widest variation ranges in our experiments (i.e. over 2 orders of magnitude). Therefore, as $\hat{V}_0$ varies in a wide range, χ and B_N may generally seem to vary in the same direction but it must be noted that they are not functions of each other. Secondly, and importantly, one may wonder why the experimental results in Fig. 3.16 are concentrated in the high r_i range. The answer to this question needs highlighting the role of inertial effects, which are completely absent in our lubrication type model. As stated earlier, away from the displacing front, the flow is in the laminar regime but inertial effects are still present near the frontal region of the displacing fluid, and they play a role in initially yielding and breaking into the displaced fluid (also noted by (78)). On the one hand, it can be shown that inertial stresses at the front could be in the same order of the yield stress of the displaced fluid. On the other hand, as the densities do not much vary, these inertial stresses are mainly a function of the frontal velocity, which vary over a small range (see Fig. 3.10). Therefore, knowing that inertial stresses are large and responsible for the initial yielding of the displaced fluid, it may be expected that r_i should be also large and it should not vary over a significantly wide range. Fig. 3.16 shows that the experimental results are concentrated around $r_i \approx 0.41$, which may confirm this hypothesis. Nevertheless, it must be emphasized that, although inertial stresses can not be perhaps ignored at the front, they vanish away from the front where viscous stresses completely take over (see (78) for near front velocity measurements). This implies that, although inertial stresses contribute in determining the interfacial position, these are in fact the viscous stresses that govern the dynamics of the displacement flow behind the front and, in particular, determine whether the residual layers are static or moving.

Let us return to our analysis. Knowing that our static residual layer flows are within the class of case 5 and that our flows do not typically present the upward motion of the fluid layer near walls (due to relatively small χ), we can calculate the wall shear stress at the verge of yielding as

$$-\tau_w = B_N = \frac{f}{4} - \frac{\chi}{4}\left(1 - \ 4{r_i}^2\right). \tag{3.45}$$

The first term in the above equation appears due to the modified pressure gradient in the Newtonian layer and the second term is due to the buoyancy in the yield stress layer. Putting $f = \frac{2}{r_i^4}$ and $r_i \approx 0.41$ into equation (3.45) results in

$$B_N = 17.69 - 0.0819\chi,$$

as a measure of the transition between static and moving residual layer flows. However, this relation underestimates the critical transition observed in our experiments (i.e. $B_N \approx 100$). The reason for this discrepancy may be due to that fact that the transition between static and moving residual layers are expected to be affected by the *surface roughness* at the interface between our fluid layers (see Alba and Frigaard (78)), implying that the interfacial shear stress must be corrected based on a relation using the Darcy-Weisbach equation to eventually find (after simplification):

$$f = \frac{\lambda Re_N}{64 r_i^5}, \tag{3.46}$$

where λ is the friction factor due to a large surface roughness in the laminar regime which can be approximated by (142)

$$\lambda = \frac{10210\epsilon^2 - 529.66\epsilon + 64}{Re_h},$$

which is valid for $0.03 < \epsilon < 0.33$. In this relation ϵ is the relative roughness value and Re_h is the hydraulic Reynolds number, which can be written versus the Newtonian Reynolds number as

$$Re_h = \frac{Re_N}{2r_i}.$$

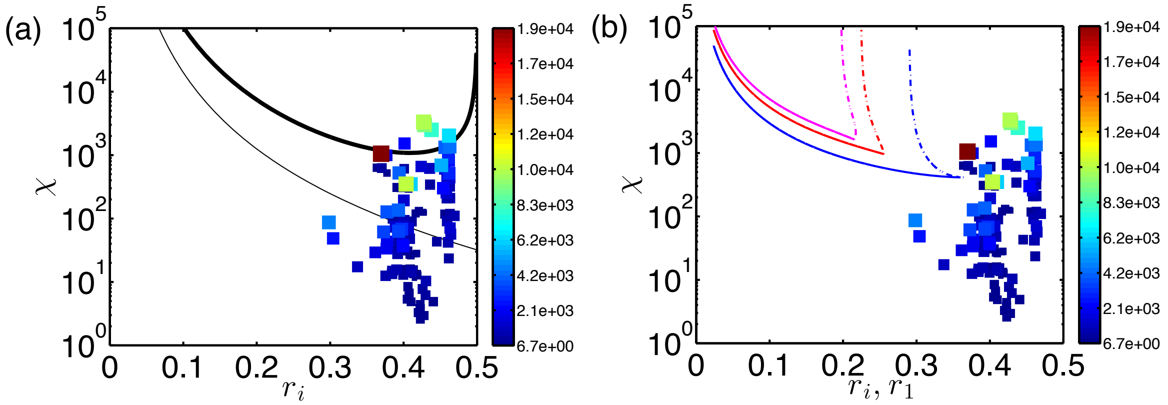

FIGURE 3.16 – (a) Variation of critical curves of χ versus r_i for case 5, according to equation (3.42) (thin solid line) and equation (3.43) (thick solid line). (b) Variation χ versus r_i (solid line) and r_1 (dash-dot line) for case 2 with $m = 1$, for various Newtonian Bingham numbers: $B_N = 20$ (blue), $B_N = 60$ (red) and $B_N = 100$ (pink). Experimental datapoints are superimposed on both subfigures as rectangles, for which the size and colour represent the values of B_N. (For interpretation of the references to colour in this figure legend, the reader is referred to the web version of this article.)

We can see that by putting $\epsilon = 0$, the modified pressure gradient (relation (3.46)) reverts back to $f = \frac{2}{r_i^4}$. We have analysed the surface roughness in our experiments following the method proposed by Alba and Frigaard (78), finding that $0.03 \leq \epsilon \leq 0.2$ in our experiments. Considering the maximum value of $\epsilon \approx 0.2$ we find

$$B_N = 101.325 - 0.0819\chi, \tag{3.47}$$

which is superimposed as the dashed line in Fig. 3.7a, showing that the transition between static and moving residual wall layers can be reasonably predicted by the analytical model.

3.5.2 Periphery displacements

Let us now look into periphery displacements, by developing a heuristic approach based on the lubrication model. We assume that in the periphery displacement the displacing fluid prefers to occupy the outer layer, and the displaced yield stress fluid tends to place itself close to the pipe centre (at least locally). We employ the same model equations as before but with the layer positions switched (i.e. the light yield stress fluid layer in the inner domain and the heavy Newtonian layer in outer domain). We will see, in theory, these flow model assumptions result in 3 distinct displacement cases (in terms of the velocity profiles), which we call case A, case B, and case C, as derived below. Before we proceed, let us first define the following plug radius

$$r_y = \frac{2\,B_N}{|f - \chi|}, \tag{3.48}$$

which will simplify the presentation of the results for each case in the following subsections.

Case A: $f \geq \chi$ **&** $-\tau_i > B_N$

For case A, f can be found through

$$\begin{aligned} \frac{1}{4} &= \frac{((96\,\chi - 48\,f)\,m + 48\,f - 48\,\chi)\,{r_i}^4 - 128\,B_N\,{r_i}^3}{384\,m} \\ &+ \frac{48\,\chi\,{r_y}^4 - 24\,{r_i}^2\chi\,m - 48\,f\,{r_y}^4 + 128\,B_N\,{r_y}^3 + 3\,f\,m}{384\,m}, \end{aligned} \tag{3.49}$$

and the flux function becomes

$$\begin{aligned} q &= \frac{24\,{r_i}^4\chi\,\ln(2r_i)\,m + 6\,(f - 2\,f\,m - \,\chi)\,{r_i}^4}{48\,m} \\ &+ \frac{6\,\chi\,{r_y}^4 - 16\,B_N\,{r_i}^3 + 3\,{r_i}^2 f\,m - 6\,f\,{r_y}^4 + 16\,B_N\,{r_y}^3}{48\,m}. \end{aligned} \tag{3.50}$$

The velocity profiles are

$$\begin{cases} u_L = \frac{(f-\chi)\left({r_i}^2-{r_y}^2\right)}{4m} - \frac{B_N(r_i-r_y)}{m} + \frac{f}{16} + \frac{{r_i}^2\chi}{2}\,\ln(2r_i) - \frac{{r_i}^2 f}{4}, & 0 \leq r \leq r_y \\ u_L = \frac{(f-\chi)\left({r_i}^2-r^2\right)}{4m} - \frac{B_N(r_i-r)}{m} + \frac{f}{16} + \frac{{r_i}^2\chi}{2}\,\ln(2r_i) - \frac{{r_i}^2 f}{4}, & r_y < r \leq r_i \\ u_H = \frac{f}{16} + \frac{ri^2\chi}{2}\,\ln(2r) - \frac{r^2 f}{4}. & r_i < r \leq 1 \end{cases} \tag{3.51}$$

Figs. 3.17a and b show an example of the variation of the shear stress and the velocity profile, versus r, respectively, for case A.

Case B: $f < \chi$ **&** $\tau_i > B_N$

For case B, f can be found through

$$\begin{aligned} \frac{1}{4} &= \frac{((96\,\chi - 48\,f)\,m + 48\,f - 48\,\chi)\,{r_i}^4 + 128\,B_N\,{r_i}^3}{384\,m} \\ &+ \frac{48\,\chi\,{r_y}^4 - 24\,{r_i}^2\chi\,m - 48\,f\,{r_y}^4 - 128\,B_N\,{r_y}^3 + 3\,f\,m}{384\,m}. \end{aligned} \tag{3.52}$$

Also, the flux function is

$$q = \frac{24\,ri^4\chi\,\ln(2r_i)\,m + 6\,(\,f - 2\,fm - \,\chi)\,{r_i}^4 + 16\,B_N\left({r_i}^3 - \,{r_y}^3\right) + 3\,{r_i}^2 f\,m + 6{r_y}^4\,(\chi\, - f)}{48m}. \tag{3.53}$$

The velocity profiles are

$$\begin{cases} u_L = \frac{(f-\chi)\left({r_i}^2-{r_y}^2\right)}{4m} + \frac{B_N(r_i-r_y)}{m} + \frac{f}{16} + \frac{{r_i}^2\chi}{2}\,\ln(2r_i) - \frac{{r_i}^2 f}{4}, & 0 \leq r \leq r_y \\ u_L = \frac{(f-\chi)\left({r_i}^2-r^2\right)}{4m} + \frac{B_N(r_i-r)}{m} + \frac{f}{16} + \frac{{r_i}^2\chi}{2}\,\ln(2r_i) - \frac{{r_i}^2 f}{4}, & r_y < r \leq r_i \\ u_H = \frac{f}{16} + \frac{ri^2\chi}{2}\,\ln(2r) - \frac{r^2 f}{4}. & r_i < r \leq 1 \end{cases} \tag{3.54}$$

Figs. 3.17c and d show an example of the variation of the shear stress and the velocity profile, versus r, respectively, for case B.

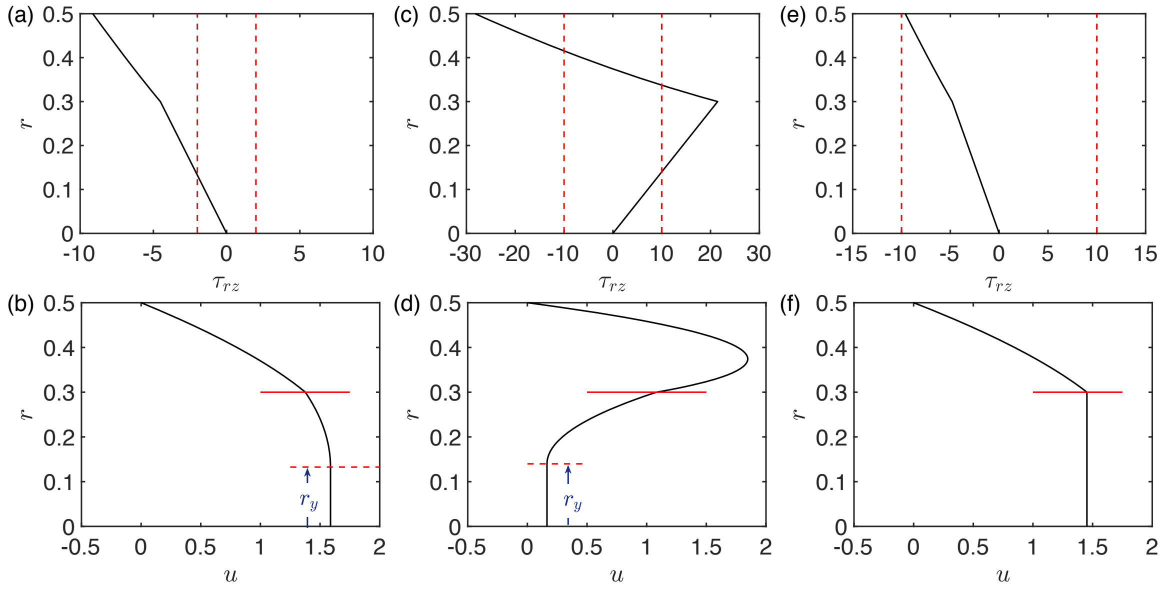

FIGURE 3.17 – Model results: variation of the shear stress (top row) and velocity profiles (bottom row) versus radius for periphery displacements with $m = 1$ and $r_i = 0.3$: (a) Case A: $\chi = 10$ & $B_N = 2$; (c) Case B: $\chi = 400$ & $B_N = 10$; (e) Case C: $\chi = 10$ & $B_N = 10$. In the top row, the dashed lines mark $\pm B_N$ for each case. In the bottom row, r_i is marked by the thick horizontal lines and r_y is marked by arrows and horizontal dashed lines.

Case C: $|\tau_i| \leq B_N$

Finally for case C, f is simply

$$f = \frac{4\,{r_i}^4\chi - {r_i}^2\chi - 4}{8\,(16\,{r_i}^4 - 1)}, \tag{3.55}$$

while the flux function is

$$q = \frac{{r_i}^2}{4}\left(2\,{r_i}^2\chi\,\ln(2r_i) + \frac{f}{4} - {r_i}^2 f\right) \tag{3.56}$$

and the velocity profiles are

$$\left\{\begin{array}{ll} u_L = \frac{f}{16} + \frac{ri^2\chi}{2}\,\ln(2r_i) - \frac{{r_i}^2 f}{4}, & 0 \leq r \leq r_i \\ u_H = \frac{f}{16} + \frac{ri^2\chi}{2}\,\ln(2r) - \frac{r^2 f}{4}. & r_i < r \leq 1 \end{array}\right. \tag{3.57}$$

Figs. 3.17e and f show an example of the variation of the shear stress and the velocity profile, versus r, respectively, for case B.

Physical relevance of the model in our displacement flow context

Although the different cases for periphery displacements (i.e. cases A, B, and C) are possible in theory, they are not all relevant to our experimental conditions. In fact, as we start our displacements with an initially flat interface, for the displacing fluid to flow around the displaced

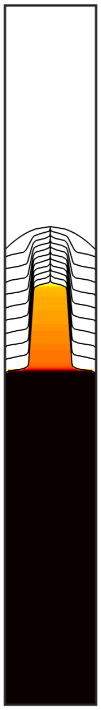

Figure 3.18 – Model results for a physically relevant periphery displacement flow: interface evolution obtained using the model corresponding to an experiment with $n = 0.45$, $\chi = 341$, $B_N = 253$, $m = 1504$: displacement in a pipe with the dimensionless diameter of 1 and the dimensionless length of $L = 3$, for $t = 0$, 0.05, ... 0.45, 0.5.

fluid, it may be intuitive that the displacement must be in the regime of case B (with a velocity profile that is faster in the outer region). On the other hand, looking at the velocity profiles in cases A and C shows that, with an initially flat interface, these profiles will not likely evolve to become a physically relevant periphery displacement. Our solution of the interface evolution equation for cases A and B also confirms this conclusion (the results are not shown for brevity). In order to visualize how a periphery displacement may evolve in a realistic situation, Fig. 3.18 illustrates a simulation result to be compared with a corresponding experiment. As can be seen, a nearly flat interface (i.e. in fact slightly concave for numerical solution reasons) develops to remove the yield stress fluid through the outer layer.

Within the periphery model developed so far, on increasing χ, the flow transitions between regimes A, C and finally into B. Therefore, we expect to find the regime of case B at relatively larger values of χ. In order to analyse how the flow transitions into the regime of case B, we may look into the variation of $\partial q/\partial r_i$ (which is proportional to the interface speed), as

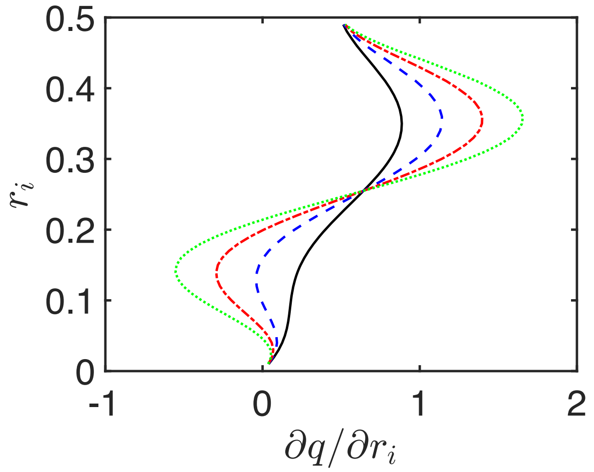

FIGURE 3.19 – Variation of $\partial q/\partial r_i$ for $B_N = 100$ and $m = 1$ with $\chi = 200$ (line), 400 (dashed line), 600 (dash-dot line) and 800 (dotted line).

depicted for example in Fig. 3.19 for a given parameter set. As can be seen, by increasing χ values, $\partial q/\partial r_i$ (which initially has positive values only) gradually curves further and starts to have negative values. Based on this observation, we can define a critical buoyancy number, $\chi_{c,\text{periphery}}$, as the minimum value of χ for which $\partial q/\partial r_i = 0$ for an interface in the range of $(0, 1/2)$, or more formally the value of χ for which the following holds:

$$\exists!\, r_i \in \left(0, \frac{1}{2}\right) : \frac{\partial q}{\partial r_i} = 0. \tag{3.58}$$

Fig. 3.20a plots the contour line of $\partial q/\partial r_i = 0$ in the plane of χ and r_i, for two parameter sets. The minimum values of χ (i.e. $\chi_{c,\text{periphery}}$) are marked by red circles and dotted lines. Increasing B_N results in increasing $\chi_{c,\text{periphery}}$. Fig. 3.20b shows the variation of $\chi_{c,\text{periphery}}$ versus m for different B_N: by increasing B_N, $\chi_{c,\text{periphery}}$ gradually increases but at very large B_N it reaches a constant value of ~ 367, independent of both B_N and m. For $\chi \geq \chi_{c,\text{periphery}}$, the flow may be expected to present a physically acceptable periphery displacement.

It is now insightful to compare the model results in terms of the existence of periphery displacements (i.e. entering the regime of case B as a physically acceptable solution) with our experimental results. This can be done through using the critical buoyancy number of $\chi_{c,\text{periphery}} = \left.\frac{2R_N}{Fr^2}\right|_c = 367$, as a rough estimate. Fig. 3.21 plots our experimental datapoints in the plane of Re_N/Fr and Fr. The line represents $Re_N/Fr^2 = 367/2 = 183.5$, from the model. It seems that the model prediction is more or less acceptable in terms of separating the central and periphery displacement flows.

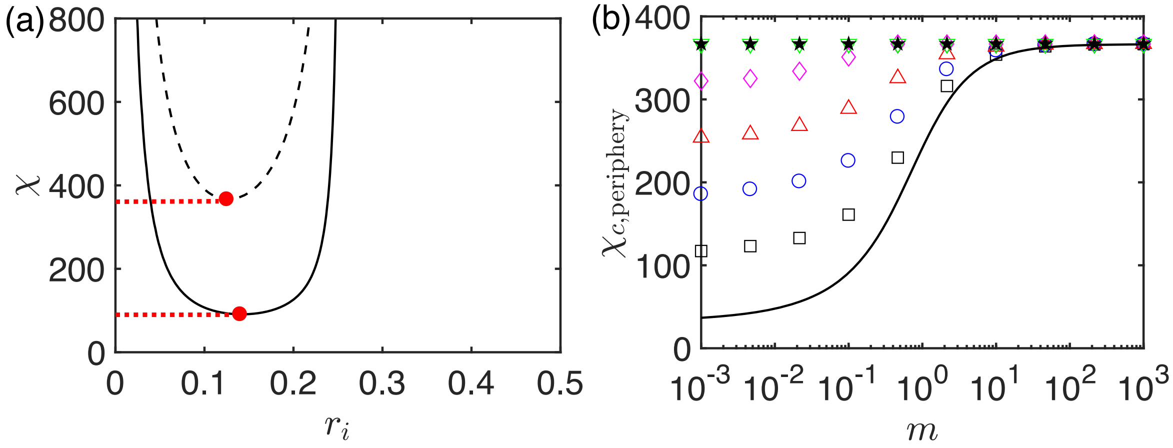

FIGURE 3.20 – (a) Variation of the contour of $\partial q/\partial r_i = 0$ in the plane of χ and r_i for two cases: $B_N = 0$ & $m = 0.1$ (solid line) and $B_N = 20$ & $m = 10$ (dashed line). The minimum values of χ are marked by the red circles and horizontal dotted lines, corresponding to $\chi_{c,\mathrm{periphery}} \approx 91$ and ≈ 367. (b) Variation of the critical (i.e. the minimum) values of the buoyancy number, $\chi_{c,\mathrm{periphery}}$, versus the viscosity ratio, m, for $B_N = 0$ (solid line), $B_N = 5$ (□), $B_N = 10$ (○), $B_N = 15$ (△), $B_N = 20$ (◇), $B_N = 50$ (▽), $B_N = 1000$ (★). (For interpretation of the references to color in this figure legend, the reader is referred to the web version of this article.)

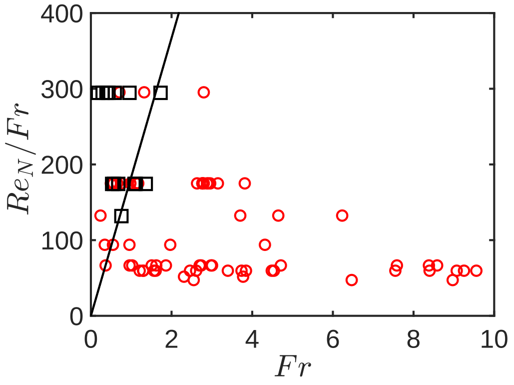

FIGURE 3.21 – Regime classification in the plane of Re_N/Fr and Fr: central (○) and periphery (□) displacements. The oblique line represents $Re_N/Fr^2 = 183.5$

3.6 Computational fluid dynamics (CFD) simulations

In order to complete our experimental and analytical methods in providing an understanding about our complex flows, here we present our findings from CFD simulations for a specific range of the flow parameters similar to an experimental set. Our computational study is performed in a vertical 2D channel (i.e. the $\hat{z}\hat{y}$-plane in Fig. 3.1). Therefore, the dimensionless groups for simulations are based on the channel thickness instead of the pipe diameter. We rely on the governing equations presented in detail in § 3.2, at the limit of $Pe \to \infty$ (implying that the numerical diffusion dominates). No slip boundary conditions are satisfied at the walls. The aspect ratio of the channel (length to width) is 100, comparable to our experiments. The heavy fluid enters the domain with a fully developed velocity profile (plane Poiseuille profile) at the inlet ($x = -L/5$) and the outflow boundary conditions are applied at the outlet ($x = 4L/5$). The equations of motion are discretized using a mixed finite element-finite volume method, employing the classical augmented Lagrangian method (143). The computational algorithm is implemented in C++ and solved using an open source platform, called PELICANS. More details on the computational approach and employing the PELICANS platform for CFD simulations of yield stress flows can be found in (30; 86; 144). In our simulations, 63,000 mesh cells (1500×42) are used, while the meshes (regular rectangular) in the y-direction are refined slightly towards the channel walls. The initial interface between two fluids is separated by an imaginary gate valve located at $x = 0$, to mimic the experiments. For brevity, we refer to (67) for more details about the mesh density and benchmarking of the computational code.

Fig. 3.22 depicts CFD simulation results (concentration colourmaps and velocities) with similar flow parameters as in the experimental set illustrated at the bottom row of Fig. 3.3 (for simplicity of the comparison between the experimental and simulation results, the experimental images of the bottom row of Fig. 3.3 are replotted in Fig. 3.22d). Fig. 3.22a shows the transparent heavy fluid displacing the dark light fluid downward, for which the CFD results appear to be in reasonable agreement with experimental ones in terms of the overall flow behaviours. Similar to our experiments, at small yield stress values, unstable displacements with strong mixing between the two fluids are visualized. As the yield stress increases, the mixing decreases. At intermediate yield stress values, non-uniform, asymmetric static residual wall layers of the yield stress fluid are formed. This is a particularly fascinating observation since we find that our CFD simulations in a simple 2D channel are still able to predict these exotic static residual layer features. Finally, at even larger yield stress values, the flow is fully stable and static residual layers are smooth, in good agreement with the experimental observations. Fig. 3.22b shows the corresponding speed contours ($\sqrt{v^2 + u^2}$) for the concentration colourmaps presented in Fig. 3.22a, where u and v are the stream-wise and depth-wise velocity components, respectively. As seen, at small yield stresses, the velocity field is far from both a Poiseuille-like flow and a plug-type flow, while the high speed regions are towards the channel centre with oscillations due to mixing. These oscillations decrease by increasing the

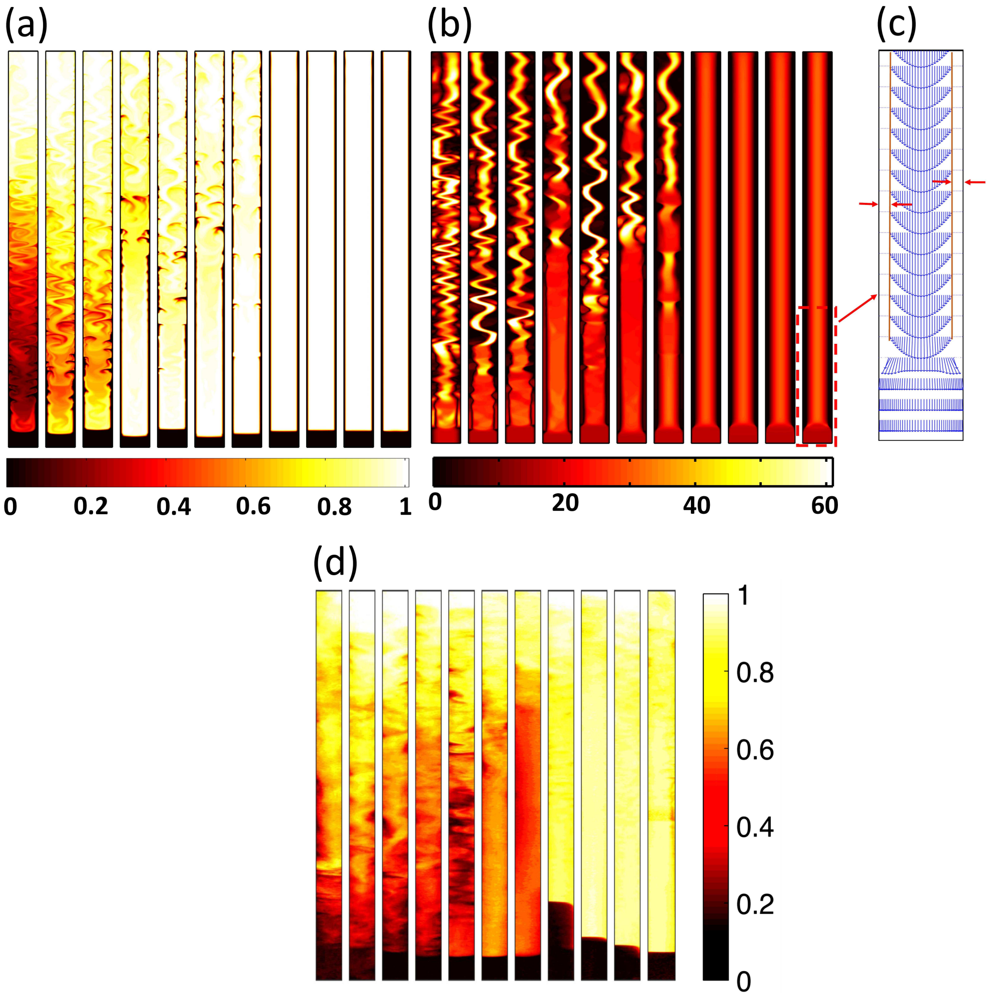

Figure 3.22 – CFD results approximately corresponding to the experimental results in the bottom row of Fig. 3.3. (a) Concentration colourmaps. (b) Speed contours: $\sqrt{v^2 + u^2}$. In (a) & (b), from left to right the Newtonian Bingham number increases from $B_N = 0$ to $B_N = 5200$. The domain size in the CFD results shown is 1×80, starting from the imaginary gate valve position at $z = 0$. (c) Velocity vectors. (d) The same experimental snapshot images depicted in the bottom row of Fig. 3.3. The image is zoomed-in on the indicated boxes of subfigure (a) & (b). The red arrows mark the thickness of static residual layers which appear at these conditions. (For interpretation of the references to colour in this figure legend, the reader is referred to the web version of this article.)

yield stress value and the flow profile resemble a typical plug flow of a Bingham fluid. At these conditions, the speed contours are zero within the yield stress fluid adjacent to the channel walls, showing residual layers that are completely static. Fig. 3.22c plots the velocity vector field for the simulation at the largest yield stress value, confirming the existence of completely static displaced fluid residual layers adjacent to the channel walls, wherein the velocity is completely zero. Moreover, it can be seen that there exist frontal inertial effects (which were ignored in the analytical model), which are responsible for breaking into the yield stress fluid, and the flow behind the front is nearly laminar. Finally, the static layer thickness from CFD simulations is interestingly in an acceptable agreement with their corresponding experimental results.

3.7 Conclusions

We investigated fluid displacement flows in a long vertical pipe, experimentally, analytically and computationally. The displaced fluid was a yield stress fluid while the displacing fluid was a Newtonian fluid. The fluids were miscible (at the limit of large Pe) and had a different density (at the limit of the Boussinesq approximation). The main dimensionless numbers that controlled the flow were the Newtonian Bingham number (B_N), the Newtonian Reynolds number (Re_N), the Froude number (Fr), the viscosity ratio (m), or the combination of these parameters which appeared as an effective Reynolds number ($Re_N^* = \frac{Re_N}{m+B_N}$), a buoyancy number ($\chi = 2Re_N/Fr^2$) or the ratio between the Newtonian Reynolds number and the Froude number (Re_N/Fr).

It is found that the yield stress and buoyancy forces strongly affect the displacement flow behaviours. By increasing B_N, the main flow regime changes from a moving to a stationary residual wall layer regime, with the critical transition occurring at $B_N \approx 100$. For moving residual layers ($B_N < 100$), nearly-stable and unstable flow sub-regimes are observed, for which the critical transition occurs at $\chi \approx 120$, above which buoyancy starts to dominate the flow. For static residual layer flows ($B_N \gtrsim 100$), smooth, wavy and corrugated residual layers are observed, for which the critical transitions can be described in the plane of Re_N^* and Re_N/Fr.

A semi-analytical lubrication model was developed and succeeded in predicting some of the flow behaviours. Most importantly, the front velocity of the heavy fluid into the light fluid cannot be predicted by the lubrication model. On the other hand, the transition between stationary and moving residual layers can be well predicted by the model wherein the interface surface roughness is included. A secondary flow feature, i.e. the appearance of central and periphery displacement (near the front) can be well predicted by the lubrication model.

Finally, CFD computations in a simpler 2D geometry reveal that some of the key flow patterns, including non-uniform as well as smooth static residual layers, may be predicted using high quality CFD simulations in simpler geometries. Therefore, this suggests that CFD computations may be used in future to provide further understanding about our complex fluid flows.

General conclusions and future perspectives

The main goal of this Ph.D. thesis is to understand displacement flows of Newtonian and non-Newtonian fluids in stationary or moving confined pipes. In this chapter the main contributions and scientific conclusions of this thesis are summarized and potential directions for future research are identified.

We categorize the main findings of this thesis into two groups:
- Buoyant miscible displacement flows of iso-viscous Newtonian fluids in the stationary vertical pipe or periodically moving pipe.
- Buoyant miscible displacement flows of the yield stress fluid in the stationary vertical pipe.

One part of the results reported in this work is based on the iso-viscous Newtonian fluid displacements. The density unstable configuration is studied in this research. For both stationary and moving geometries the approach is experimental.

It was observed that for the displacement flow in the stationary geometry at the small Atwood number and $\hat{V}_0 = 0$, some instabilities occur between the finger of the displacing fluid and the surrounding displaced fluid. However, these helical instabilities are not strong to be able to mix the fluids. The helical instabilities are faded after a few pipe diameters. The flow at long times displays a stable counter-current flow. By adding the mean imposed flow velocity to the system, the flow behaviour significantly changes. First, there is a transition from counter-current to stable flow. Second, the initial interfacial waves and inertial tip decrease by increasing the mean imposed flow velocity. At higher Atwood numbers, e.g. $At = 10^{-3}$, we clearly observed the stabilizing effect of the mean imposed flow. The overall mixing seems to decrease as the mean imposed flow velocity increases. At a critical mean imposed flow velocity, we observed that the flow is completely stabilized. It is obvious that at the larger Atwood number, the buoyancy force is stronger and consequently the critical mean imposed flow velocity increases to stabilize the flow.

In addition, it was found that for the displacement flow in the stationary geometry the problem analysis can be reduced to two dimensionless numbers, i.e. Re_t and Fr for a wide range of experiments. Two main flow regimes were identified as stable and unstable displacement flows. The transition between these two regimes is quantified by $Re_t|_{Critical}$ as a function of Fr. For the stable displacement flows $Re_t|_{Critical} < 79 + Fr + 2Fr^2$; otherwise, the regime is unstable. It shows that increasing $\hat{V}_0$ stabilizes the displacement flow for certain ranges of the dimensionless groups.

Moreover, we observed that when the flow is stable, the displacement flow regime is divided into sustained-back-flows and no-sustained-back-flows. In the latter, the buoyancy is not strong to induce a sustained movement of the displaced fluid above the gate valve. In the former, due to a higher ratio of buoyancy to viscous stresses, the displaced fluid continuously moves upward above the gate valve. The transition between these two regimes occurs at the critical buoyancy number $\chi_s \approx 230$, well predicted by the lubrication model. For the stable flow regime, the lubrication model delivered the front velocity at longer times V_f^{Lub}, when the viscous force dominates the inertial force in balancing buoyancy. Using V_f^{Lub} and a velocity scale formulation for the initial inertial acceleration, a predictive model for $V_f(t)$ provides a reasonable agreement with the experimental data.

Another important contribution of this thesis is addressing the issue of the displacement flow in the moving pipe. Many observations are made. First of all, in the moving and stationary geometries when $\hat{V}_0 > 0$, the displacing fluid finger seems to progress in the displaced fluid. While in the stationary case, the interface between two fluids is clean and sharp, in the moving case, the interface, especially at the front tip, is not sharp. We named this regime as stable-diffusive regime. Second, at $\hat{V}_0 = 0$, for the moving pipe the displacing fluid does not significantly penetrate into the displaced fluid, while in the stationary pipe the helical waves appear at the interface between fluids and they eventually disappear.

Another interesting phenomenon is that in the stationary pipe, the heavy fluid advances in the middle of the pipe. Consequently, the front interface is perpendicular to the pipe longitudinal axis. But for the moving case, the pipe inclination varies over the range of $-15\ (^\circ) < \beta < 15\ (^\circ)$. Therefore, a local segregation between two fluids is observed perhaps due to transverse buoyancy forces. So, the front interface is not always perpendicular to the pipe longitudinal axis. This phenomenon owes to the Boycott effect that causes the displacing fluid to be locally separated from the displaced fluid so that the sedimentation velocity increases.

Moreover, we found that pipe movement caused the appearance of the stable-diffusive regime, in which the fluids slightly mix not due to the buoyancy but primarily due to the pipe movement. Therefore, this phenomenon is considered at small At while the pipe motion dominates. The flow regime map indicates that these flows are observed at $Re/Fr^2 < 35$ and $Re/Ro > 70$. A stable flow regime is observed at $Re/Fr^2 < 35$ and $Re/Ro < 70$. We observed an unstable-diffusive flow regime at $Re/Fr^2 > 35$ for all ranges of frequencies tested. In addition, we have found that $\hat{V}_f$ and $\hat{D}_M$ quickly increase with time to attain their final nearly-steady values.

Comparing with the stationary pipe, when the pipe moves periodically and the fluids have smaller density differences, $\hat{V}_f$ decreases while the opposite effect is observed at larger density differences. Investigating $\hat{D}_M$ at large At shows that $\hat{D}_M$ is larger for displacement flows in the moving pipe.

Finally, we experimentally studied the yield stress displacement flow in the stationary pipe. First of all, we observed two main flow regimes: the moving residual layer regime and the stationary residual layer regime. The transition between these regimes is a function of B_N number. The flow regime map shows that the critical Newtonian Bingham number is $B_N = 100$. Each regime is divided into different sub-regimes. However, B_N is not solely able to classify all sub-regimes and there are other important forces that can affect displacement flow behaviours e.g. Newtonian Reynolds number and the densimetric Froude number. Using the combination of these dimensionless numbers, we found that in the moving residual layer, the unstable and nearly- stable sub-regimes exist, for which the critical transition occurs at $\chi \approx 120$, where the buoyancy is the dominant force. For static residual layer flows, we observed smooth, wavy and corrugated residual layers, for which the critical transitions can be explained in the plane of Re_N^* and Re_N/Fr. In addition, we could predict some of the flow patterns analytically e.g. the transition between stationary and moving residual layers. However, the model fails to predict some other patterns e.g. the front velocity. Moreover, computational fluid dynamics simulations in a 2D geometry can reproduce some of the key flow patterns.

Limitations of the present thesis

In the current thesis, many features of displacement flows have been investigated. However, due to limitations, we have not been able to have a comprehensive study in many respects. Although a number of advances have been made in our study, we must also acknowledge some limitations of our experimental and computational investigations. The experimental limitations are the cost, the time of each experiment, fluid properties, the length and the diameter of the pipe. Some of these limitations are explained below:

• First, in the present thesis, we use a single pipe diameter 9.6 (mm). The main dimensionless numbers in our research are Re_N, Fr, and B_N. The combination of these dimensionless numbers enables us to classify different regimes. By changing the mean imposed flow velocity, all of these numbers change linearly. Therefore, an independent assessment of these parameters is vague. If we could vary the pipe diameter, the Fr increases by decreasing $\hat{D}$ ($Fr \approx 1/\sqrt{\hat{D}}$) whereas Re_N and B_N decrease by decreasing $\hat{D}$. Thus, it is an easier assessment of the individual effects of the main dimensionless numbers. Therefore, a better understanding of the physical mechanisms of various flow regimes requires running experiments at different pipe diameters.

• Second, in this research, the short time behaviour of flows has not been investigated. In other words, the behaviour of flows right after opening the gate valve has not been studied when the pressure gradient is imposed to the system. Strong inertial effects and accelerations in different directions are two characteristics of this stage which led to a partial local mixing at early times. It is obvious that the partial local mixing affects the local density contrast and it may impact the dynamics of flows. To quantify how the dynamics of flows at this stage affects the long time behaviours, understanding of the short time behaviour of flows is important.

• The third limitation is related to the working fluids. Preparation of water-based solutions may coincide with dissolving air into the solutions. The degassing processes of water-based solutions have not been performed in our experiments. Degassing of the solutions with a vacuum pump in a sealed tank helps to reduce associated effects of bubbles in solutions. The existence of bubbles in the fluids affects the viscosity of fluids and the rheological properties. Consequently, it can change the displacement flow behaviours and related results.

• Another limitation is that when the degree of transverse mixing is relatively high, we know that the diffusive spreading along the pipe is important. To better observe these flows we need to increase the length of the pipe (our current pipe length is 2.02 (m)). This helps us to better analyse the long time mixing behaviour and measure the macroscopic diffusion coefficient with higher accuracy.

• Finally, in terms of computational investigation in Chapter 3, our study was performed in a 2D vertical plane channel in which the dimensionless groups for simulations are defined based on the channel width instead of the pipe diameter. To better understanding the flow behaviour, the simulations can be performed in a 3D vertical pipe. However, the drastic computational cost of simulations with high mesh densities limited us to conduct such simulations in a 3D frame.

Future work recommendations

The main motivation of studying the displacement flow in the present study comes from the primary cementing process. The main objective is predicting the displacement efficiency of one fluid by another one with different properties when the fluids flow downward. To date, although many aspects of displacement flows have been well understood, there are still many issues to be understood and to be analysed. Therefore, the current thesis may suggest a number of paths for future research.

• Newtonian density stable/unstable displacement flows in the presence of different pipe motions: First of all, due to the simple form of the interface, the density stable displacement flow has the least challenging behaviour to analyse. In addition, compared to the unstable displacement flow, the majority of data published in the literature concerns the unstable displacement flow. Therefore, it would be interesting to investigate the stable displacement flow in any direction, especially by adding the effect of different geometry motions. Second, in the case of the unstable displacement flow, there is also a large gap in the literature when the geometry is moving. In a more particular case, the stable-diffusive regime indicates very interesting fingering features when the geometry slowly oscillates like an inverted pendulum, which can be further studied experimentally or numerically. In addition, there are many geometry motions (e.g. rotation, reciprocation) that can be of great importance for industrial applications and can be applied and investigated in depth.

- Shear-thinning, yield stress, elastic and viscoelastic effects on stable/unstable displacement flows in stationary and moving geometries: A large part of fluids pumped into the oil and gas wells during the primary cementing process have yield stress, shear-thinning, elastic and viscoelastic behaviours. Although we investigated the yield stress effects of displacement flows in a vertical stationary pipe, there is still a need for experimental, analytical and numerical investigations of the shear-thinning, the yield stress, elastic and viscoelastic effects on the displacement flow, especially in moving geometries.

- Laser Induced Florescence (LIF), Particle Image Velocimetry (PIV), and Ultrasound Doppler Velocimetry (UDV) techniques: In this thesis, to increase the quality of the images, the back-lit technique was applied. Bulk properties of displacement flows were described using an image processing method. A wide range of detailed data showed that the physics of flows could be measured using this type of experiments. To investigate more precisely the concentration field with a higher resolution, we advise using the LIF technique. In addition, the velocity field data and the local velocity can also be studied with a high resolution using the PIV and UDV techniques.

Bibliography

[1] S. H. Bittleston, J. Ferguson, and I. A. Frigaard. Mud removal and cement placement during primary cementing of an oil well–laminar non-Newtonian displacements in an eccentric annular Hele-Shaw cell. *Journal of Engineering Mathematics*, 43 (2-4), 229–253, 2002.

[2] E. B. Nelson and D. Guillot. *Well Cementing, 2nd Edition.* Schlumberger Educational Services, 2006.

[3] H. K. Foroushan, E. Ozbayoglu, P. J. Gomes, S. Miska, M. Yu, et al. Mud-cement displacement in eccentric annuli: Analytical solution, instability analysis, and computational fluid dynamics simulations. In *IADC/SPE Drilling Conference and Exhibition.* Society of Petroleum Engineers, 2018.

[4] P. J. Fryer, G. K. Christian, and W. Liu. How hygiene happens: physics and chemistry of cleaning. *International Journal of Dairy Technology*, 59 (2), 76–84, 2006.

[5] J. Wiklunda, M. Stadinga, and Ch. Tragardh. Monitoring liquid displacement of model and industrial fluids in pipes by in-line ultrasonic rheometry. *Journal of Food Engineering*, 99, 330–337, 2010.

[6] D. E. Elrick, K. T. Erh, and H. K. Krupp. Applications of miscible displacement techniques to soils. *Water Resources Research*, 2, 717–727, 1966.

[7] M. A. Parvez, N. S. Ong, Y. C. Lam, and S. B. Tor. Gas-assisted injection molding: the effects of process variables and gas channel geometry. *Journal of Materials Processing Technology*, 121 (1), 27–35, 2002.

[8] P. M. Schweizer and S. F. Kistler. *Liquid Film Coating: Scientific Principles and Their Technological Implications.* Springer Science & Business Media, 2012.

[9] P. D. Howell, S. L. Waters, and J. B. Grotberg. The propagation of a liquid bolus along a liquid-lined flexible tube. *Journal of Fluid Mechanics*, 406, 309–335, 2000.

[10] N. G. Cogan and J. P. Keener. Channel formation in gels. *SIAM Journal on Applied Mathematics*, 65 (6), 1839–1854, 2005.

[11] K. E. Holloway, P. Habdas, N. Semsarillar, K. Burfitt, and J. R. de Bruyn. Spreading and fingering in spin coating. *Physical Review E*, 75 (4), 046308, 2007.

[12] I. A. Frigaard, K. G Paso, and P. R. de Souza Mendes. Bingham model in the oil and gas industry. *Rheologica Acta*, 56 (3), 259–282, 2017.

[13] R. C. Haut, R. J. Crook, et al. Primary cementing: The mud displacement process. In *SPE Annual Technical Conference and Exhibition*. Society of Petroleum Engineers, 1979.

[14] C. Holt, N. LAhotiI, and V. Foritier. New cementing method uses pipe movement to maximize displacement. *Drilling Contractor*, 69 (2), 2013.

[15] S. M. Taghavi, T. Seon, D. M. Martinez, and I. A. Frigaard. Buoyancy-dominated displacement flows in near-horizontal channels: the viscous limit. *Journal of Fluid Mechanics*, 639, 1–35, 2009.

[16] S. M. Taghavi, K. Alba, T. Seon, K. Wielage-Burchard, D. M. Martinez, and I. A. Frigaard. Miscible displacement flows in near-horizontal ducts at low Atwood number. *Journal of Fluid Mechanics*, 696, 175–214, 2012.

[17] S. M. Taghavi, R. Mollaabbasi, and Y. St-Hilaire. Buoyant miscible displacement flows in rectangular channels. *Journal of Fluid Mechanics*, 826, 676–713, 2017.

[18] K. Alba, S. M. Taghavi, and I. A. Frigaard. Miscible density-unstable displacement flows in inclined tube. *Physics of Fluids*, 25, 067101, 2013.

[19] K. Alba, S. M. Taghavi, and I. A. Frigaard. Miscible heavy-light displacement flows in an inclined two-dimensional channel: a numerical approach. *Physics of Fluids*, 26 (12), 122104, 2014.

[20] A. Etrati and I. A. Frigaard. A two-layer model for buoyant inertial displacement flows in inclined pipes. *Physics of Fluids*, 30 (2), 022107, 2018.

[21] M. Zare and I. A. Frigaard. Buoyancy effects on micro-annulus formation: density unstable Newtonian–Bingham fluid displacements in vertical channels. *Journal of Non-Newtonian Fluid Mechanics*, 260, 145–162, 2018.

[22] R. Mollaabbasi and S. M. Taghavi. Buoyant displacement flows in slightly non-uniform channels. *Journal of Fluid Mechanics*, 795, 876–913, 2016.

[23] E. Walling, R. Mollaabbasi and S. M. Taghavi. Buoyant miscible displacement flows in a nonuniform Hele-Shaw cell. *Physical Review Fluids*, 3, 034003, 2018.

[24] M. B. Amar and E. C. Poire. Pushing a non-Newtonian fluid in a Hele-Shaw cell: from fingers to needles. *Physics of Fluids*, 11 (7), 1757–1767, 1999.

[25] M. Allouche, I. A. Frigaard, and G. Sona. Static wall layers in the displacement of two viscoplastic fluids in a plane channel. *Journal of Fluid Mechanics*, 424, 243–277, 2000.

[26] Y. Dimakopoulos and J. Tsamopoulos. Transient displacement of a viscoplastic material by air in straight and suddenly constricted tubes. *Journal of Non-Newtonian Fluid Mechanics*, 112 (1), 43–75, 2003.

[27] I. A. Frigaard and D. P. Ryan. Flow of a viscoplastic fluid in a channel of slowly varying width. *Journal of Non-Newtonian Fluid Mechanics*, 123 (1), 67–83, 2004.

[28] Y. Dimakopoulos and J. Tsamopoulos. Transient displacement of Newtonian and viscoplastic liquids by air in complex tubes. *Journal of Non-Newtonian Fluid Mechanics*, 142 (1–3), 162–182, 2007.

[29] P. R. de Souza Mendes, M. F. Naccache, P. R. Varges, and F. H. Marchesini. Flow of viscoplastic liquids through axisymmetric expansions–contractions. *Journal of Non-Newtonian Fluid Mechanics*, 142 (1), 207–217, 2007.

[30] K. Wielage-Burchard and I. A. Frigaard. Static wall layers in plane channel displacement flows. *Journal of Non-Newtonian Fluid Mechanics*, 166, 245–261, 2011.

[31] S. M. Taghavi, K. Alba, M. M. Gonzalez, and I. A. Frigaard. Incomplete fluid-fluid displacement of yield stress fluids in near-horizontal pipes: experiments and theory. *Journal of Non-Newtonian Fluid Mechanics*, 167, 59–74, 2012.

[32] K. Alba, S. M. Taghavi, J. R. de Bruyn, and I. A. Frigaard. Incomplete fluid-fluid displacement of yield-stress fluids. Part 2: highly inclined pipes. *Journal of Non-Newtonian Fluid Mechanics*, 201, 80–93, 2013.

[33] A. Eslami and S. M. Taghavi. Viscous fingering regimes in elasto-viscoplastic fluids. *Journal of Non-Newtonian Fluid Mechanics*, 243, 79–94, 2017.

[34] U.S. Briefing. International energy outlook 2013. *US Energy Information Administration, Washington, DC*, 2013.

[35] U. F. Akpan and G. E. Akpan. The contribution of energy consumption to climate change: a feasible policy direction. *International Journal of Energy Economics and Policy*, 2, 21–33, 2011.

[36] D. Collyer. Canadian oil and gas industry outlook, opportunities & challenges. *APEGA Luncheon, Calgary, Canada*, 2012.

[37] S. M. Taghavi. From displacement to mixing in a slightly inclined duct. *Ph.D. Thesis*, University of British Columbia, 2011.

[38] I. A. Frigaard, K. G. Paso, and P. de Souza Mendes. Binghams model in the oil and gas industry. *Rheologica Acta*, 56 (3), 259–282, 2017.

[39] V. Veedu, M. Hadmack, J. Pollock, P. P. Wise, and D. A, Yo. Final scientific/technical report for "Nanite" for better well-bore integrity and zonal isolation. *Technical Report, Oceanit Laboratories, Inc., Honolulu, HI (United States)*, 2017.

[40] M. Debacq, V. Fanguet, J.P. Hulin, D. Salin, and B. Perrin. Self similar concentration profiles in buoyant mixing of miscible fluids in a vertical tube. *Physics of Fluids*, 13, 3097–3100, 2001.

[41] M. Debacq, J. P. Hulin, D. Salin, B. Perrin, and E. J. Hinch. Buoyant mixing of miscible fluids of varying viscosities in vertical tube. *Physics of Fluids*, 15, 3846–3855, 2003.

[42] T. Seon, J. P. Hulin, D. Salin, B. Perrin, and E. J. Hinch. Buoyant mixing of miscible fluids in tilted tubes. *Physics of Fluids*, 16, L103–L106, 2004.

[43] T. Seon, J. P. Hulin, D. Salin, B. Perrin, and E. J. Hinch. Buoyancy driven miscible front dynamics in tilted tubes. *Physics of Fluids*, 17, 031702, 2005.

[44] T. Seon, J. P. Hulin, D. Salin, B. Perrin, and E. J. Hinch. Laser-induced fluorescence measurements of buoyancy driven mixing in tilted tubes. *Physics of Fluids*, 18, 041701, 2006.

[45] T. Seon, J. Znaien, D. Salin, J. P. Hulin, E. J. Hinch, and B. Perrin. Transient buoyancy-driven front dynamics in nearly horizontal tubes. *Physics of Fluids*, 19, 123603, 2007.

[46] T. Seon, J. Znaien, D. Salin, J. P. Hulin, E. J. Hinch, and B. Perrin. Front dynamics and macroscopic diffusion in buoyant mixing in a tilted tube. *Physics of Fluids*, 19, 125105, 2007.

[47] J. Znaien, F. Moisy, and J. P. Hulin. Flow structure and momentum transport for buoyancy driven mixing flows in long tubes at different tilt angles. *Physics of Fluids*, 23, 035105, 2011.

[48] A. Hasnain, E. Segura, K. Alba. Buoyant displacement flow of immiscible fluids in inclined pipes. *Journal of Fluid Mechanics*, 824, 661–687, 2017.

[49] A. Hasnain, K. Alba. Buoyant displacement flow of immiscible fluids in inclined ducts: a theoretical approach. *Physics of Fluids*, 29, 052102, 2017.

[50] M. P. Escudier, I. W. Gouldson, P. J. Oliveira, and F. T. Pinho. Effects of inner cylinder rotation on laminar flow of a Newtonian fluid through an eccentric annulus. *International Journal of Heat and Fluid Flow*, 21 (1), 92–103, 2000.

[51] M. P. Escudier, P. J. Oliveira, and F. T. Pinho. Fully developed laminar flow of purely viscous non-Newtonian liquids through annuli, including the effects of eccentricity and inner-cylinder rotation. *International Journal of Heat and Fluid Flow*, 23 (1), 52–73, 2002.

[52] M. Carrasco-Teja and I. A. Frigaard. Displacement flows in horizontal, narrow, eccentric annuli with a moving inner cylinder. *Physics of Fluids*, 21 (7), 073102, 2009.

[53] M. Carrasco-Teja and I.A. Frigaard. Non-Newtonian fluid displacements in horizontal narrow eccentric annuli: effects of slow motion of the inner cylinder. *Journal of Fluid Mechanics*, 653, 137–173, 2010.

[54] G. P. Assima, A. Motamed-Dashliborun, and F. Larachi. Emulation of gas-liquid flow in packed beds for offshore floating applications using a swell simulation hexapod. *AIChE Journal*, 61, 2354–2367, 2015.

[55] A. Amiri, F. Larachi, and S. M. Taghavi. Displacement flows in periodically moving pipe: understanding multiphase flows hosted in oscillating geometry. *Chemical Engineering Science*, 170, 437–450, 2017.

[56] S. Lyu and S. M. Taghavi. Stratified flows in axially rotating pipes. *Physical Review Fluids*, 3 (7), 074003, 2018.

[57] A. Eslami and S.M. Taghavi. Viscous fingering of yield stress fluids: the effects of wettability. *Journal of Non-Newtonian Fluid Mechanics*, 264, 25–47, 2019.

[58] G. V. L. Moisés, M. F. Naccache, K. Alba, and I. A. Frigaard. Isodense displacement flow of viscoplastic fluids along a pipe. *Journal of Non-Newtonian Fluid Mechanics*, 236, 91–103, 2016.

[59] P. A. Cole, K. Asteriadou, P. T. Robbins, E. G. Owen, G. A. Montague, and P. J. Fryer. Comparison of cleaning of toothpaste from surfaces and pilot scale pipework. *Food and Bioproducts Processing*, 88 (4), 392–400, 2010.

[60] A. Renteria, A. Maleki, I. A. Frigaard, B. Lund, A. Taghipour, and J. D. Ytrehus. Displacement efficiency for primary cementing of washout sections in highly deviated wells. *SPE Asia Pacific Oil and Gas Conference and Exhibition, Society of Petroleum Engineers*, 2018.

[61] S. A. Ale Etrati Khosroshahi and I. A. Frigaard. Buoyant miscible displacement flow of shear-thinning fluids: experiments and simulations. *APS Meeting Abstracts*, 2017.

[62] J. V. Fontana, E. O. Dias, and J. A. Miranda. Controlling and minimizing fingering instabilities in non-Newtonian fluids. *Physical Review E*, 89 (1), 013016, 2014.

[63] R. Brandão, J. V. Fontana, and J. A. Miranda. Interfacial pattern formation in confined power-law fluids. *Physical Review E*, 90 (1), 013013, 2014.

[64] A. Lindner, P. Coussot, and D.l. Bonn. Viscous fingering in a yield stress fluid. *Physical Review Letters*, 85 (2), 314, 2000.

[65] H. Pascal. Rheological behaviour effect of non-Newtonian fluids on dynamic of moving interface in porous media. *International Journal of Engineering Science*, 22 (3), 227–241, 1984.

[66] G. V. L. Moisés, L. S. Alencar, M. F. Naccache, and I. A. Frigaard. The influence of thixotropy in start-up flow of yield stress fluids in a pipe. *Journal of Petroleum Science and Engineering*, 171, 794–807, 2018.

[67] A. Eslami, I. A. Frigaard, and S. M. Taghavi. Viscoplastic fluid displacement flows in horizontal channels: numerical simulations. *Journal of Non-Newtonian Fluid Mechanics*, 249, 79-96, 2017.

[68] A. Eslami, R. Mollaabbasi, and S. M. Taghavi. Effects of a channel inclination on displacements of viscoplastic fluids. *Proceeding of CSME International Congress*, 2018.

[69] A. Acrivos and E. Herbolzheimer. Enhanced sedimentation in settling tanks with inclined walls. *Journal of Fluid Mechanics*, 92 (3), 435–457, 1979.

[70] P. R. Varges, B. S. Fonseca, C. M. Costa, M. F. Naccache, P. R. de Souza Mendes, and H. A. Pinho. Exchange flows between yield stress materials and Newtonian oils. *Journal of Non-Newtonian Fluid Mechanics*, 261, 123–135, 2018.

[71] Y. Hallez and J. Magnaudet. Effects of channel geometry on buoyancy-driven mixing. *Physics of Fluids*, 20 (5), 053306, 2008.

[72] Y. Hallez and J. Magnaudet. A numerical investigation of horizontal viscous gravity currents. *Journal of Fluid Mechanics*, 630, 71–91, 2009.

[73] G. I. Taylor. Deposition of a viscous fluid on the wall of a tube. *Journal of Fluid Mechanics*, 10, 161–165, 1961.

[74] H. L. Goldsmith and S. G. Mason. The flow of suspensions through tubes. II. Single large bubbles. *Journal of Colloid Science*, 18, 237–261, 1963.

[75] S. R. Hodges, O. E. Jensen, and J. M. Rallison. The motion of a viscous drop through a cylindrical tube. *Journal of Fluid Mechanics*, 501, 279–301, 2004.

[76] E. Lac and J. D. Sherwood. Motion of a drop along the centreline of a capillary in a pressure-driven flow. *Journal of Fluid Mechanics*, 604, 27–54, 2009.

[77] E. J. Soares and R. L. Thompson. Flow regimes for the immiscible liquid–liquid displacement in capillary tubes with complete wetting of the displaced liquid. *Journal of Fluid Mechanics*, 641, 63–84, 2009.

[78] K. Alba and I. A. Frigaard. Dynamics of the removal of viscoplastic fluids from inclined pipes. *Journal of Non-Newtonian Fluid Mechanics*, 229, 43–58, 2016.

[79] J. F. Freitas, E. J. Soares, and R. L. Thompson. Viscoplastic–viscoplastic displacement in a plane channel with interfacial tension effects. *Chemical Engineering Science*, 91, 54–64, 2016.

[80] P. Petitjeans and T. Maxworthy. Miscible displacements in capillary tubes. Part 1. Experiments. *Journal of Fluid Mechanics*, 326, 37–56, 1996.

[81] C. Y. Chen and E. Meiburg. Miscible displacements in capillary tubes. Part 2. Numerical simulations. *Journal of Fluid Mechanics*, 326, 57–90, 1996.

[82] J. Scoffoni, E. Lajeunesse, and G. M. Homsy. Interface instabilities during displacements of two miscible fluids in a vertical pipe. *Physics of Fluids*, 13, 553–556, 2001.

[83] J. Kuang, P. T. Petitjeans, and T. Maxworthy. Velocity fields and streamline patterns of miscible displacements in cylindrical tubes. *Experiments in Fluids*, 37, 301–308, 2004.

[84] R. Balasubramaniam, N. Rashidnia, T. Maxworthy, and J. Kuang. Instability of miscible interfaces in a cylindrical tube. *Physics of Fluids*, 17, 052103, 2005.

[85] S. M. Taghavi, T. Seon, D. M. Martinez, and I. A. Frigaard. Influence of an imposed flow on the stability of a gravity current in a near horizontal duct. *Physics of Fluids*, 22, 031702, 2010.

[86] S. M. Taghavi, T. Seon, K. Wielage-Burchard, D. M. Martinez, and I. A. Frigaard. Stationary residual layers in buoyant Newtonian displacement flows. *Physics of Fluids*, 23, 044105, 2011.

[87] P. Redapangu, K. Chandra Sahu, and S. P. Vanka. A study of pressure-driven displacement flow of two immiscible liquids using a multiphase lattice Boltzmann approach. *Physics of Fluids*, 24, 102110, 2012.

[88] S. M. Taghavi, K. Alba, and I. A. Frigaard. Buoyant miscible displacement flows at moderate viscosity ratios and low Atwood numbers in near-horizontal ducts. *Chemical Engineering Science*, 69 (1), 404–418, 2012.

[89] K. Alba, S. M. Taghavi, and I. A. Frigaard. Miscible density-stable displacement flows in inclined tube. *Physics of Fluids*, 24 (12), 123102, 2012.

[90] K. Alba, S. M. Taghavi, J. R. de Bruyn, and I. A. Frigaard. Incomplete fluid–fluid displacement of yield-stress fluids. Part 2: highly inclined pipes. *Journal of Non-Newtonian Fluid Mechanics*, 201, 80–93, 2013.

[91] A. J. Poslinski, P. R. Oehler, and V. K. Stokes. Isothermal gas-assisted displacement of viscoplastic liquids in tubes. *Polymer Engineering & Science*, 35 (11), 877–892, 1995.

[92] M. Zare, A. Roustaei, and I. A. Frigaard. Buoyancy effects on micro-annulus formation: density stable displacement of Newtonian–Bingham fluids. *Journal of Non-Newtonian Fluid Mechanics*, 247, 22–40, 2017.

[93] M. Savery, W. Chin, and K. B. Yerubandi. Modeling cement placement using a new 3-D flow simulator. *Paper AADE*, 2008.

[94] W. R. Landrum, J. E. Porter, R. D. Turner, et al. Rotating liners during cementing in the grand isle and west delta areas, louisiana. *Journal of Petroleum Technology*, 37 (07), 1–263, 1985.

[95] S. Pelipenko and I. A. Frigaard. On steady state displacements in primary cementing of an oil well. *Journal of Engineering Mathematics*, 46 (1), 1–26, 2004.

[96] M. Carrasco-Teja, I. A. Frigaard, B. R. Seymour, and S. Storey. Viscoplastic fluid displacements in horizontal narrow eccentric annuli: stratification and travelling wave solutions. *Journal of Fluid Mechanics*, 605, 293–327, 2008.

[97] Y. Bu, L. Tian, Z. Li, R. Zhang, C. Wang, and X. I. Yang. Effect of casing rotation on displacement efficiency of cement slurry in highly deviated wells. *Journal of Natural Gas Science and Engineering*, 52, 317–324, 2018.

[98] E. Comparini. A one-dimensional Bingham flow. *Journal of Mathematical Analysis and Applications*, 169, 127–139, 1992.

[99] E. Comparini and E. De Angels. Flow of a Bingham fluid in a concentric cylinder viscometer. *Advances in Mathematical Sciences and Applications* , 6, 97–116, 1996.

[100] N. J. Balmforth, Y. Forterre, and O. Pouliquen. The viscoplastic Stokes layer. *Journal of Non-Newtonian Fluid Mechanics*, 158, 46–53, 2009.

[101] G. I. Taylor. The dispersion of matter in turbulent flow through a pipe. *Proceedings of the Royal Society of London A*, 223 (1155), 446–468, 1954.

[102] J. B. Grotberg and O. E. Jensen. Biofluid mechanics in flexible tubes. *Annual Review of Fluid Mechanics*, 36 (1), 121–147, 2004.

[103] P. Schweizer and S. F. Kistler. *Liquid film coating: Scientific principles and their technological implications.* Springer Science & Business Media, 2012.

[104] Y. Hallez and J. Magnaudet. Turbulence-induced secondary motion in a buoyancy-driven flow in a circular pipe. *Physics of Fluids*, 21, 081704, 2009.

[105] K. C. Sahu, H. Ding, P. Valluri, and O. K. Matar. Pressure-driven miscible two-fluid channel flow with density gradients. *Physics of Fluids*, 21, 043603, 2009.

[106] E. Lajeunesse, J. Martin, N. Rakotomalala, and D. Salin. 3D instability of miscible displacements in a Hele-Shaw cell. *Physical Review Letters*, 79, 5254–5257, 1997.

[107] E. Lajeunesse, J. Martin, N. Rakotomalala, D. Salin, and Y. Yortsos. Miscible displacement in a Hele-Shaw cell at high rates. *Journal of Fluid Mechanics*, 398, 299–319, 1999.

[108] E. Lajeunesse, J. Martin, N. Rakotomalala, and D. Salin. The threshold of the instability in miscible displacements in a Hele-Shaw cell at high rates. *Physical Review Letters*, 13 (3), 799–801, 2001.

[109] C. Jiao and T. Maxworthy. An experimental study of miscible displacement with gravity-override and viscosity-contrast in a Hele-Shaw cell. *Experiments in Fluids*, 44 (5), 781–794, 2008.

[110] F. Graf, E. Meiburg, and C. Haertel. Density-driven instabilities of miscible fluids in a Hele-Shaw cell: linear stability analysis of the three-dimensional stokes equations. *Journal of Fluid Mechanics*, 451, 261–282, 2002.

[111] J. Fernandez, P. Kurowski, P. Petitjeans and E. Meiburg. Density-driven unstable flows of miscible fluids in a Hele-Shaw cell. *Journal of Fluid Mechanics*, 451, 239–260, 2002.

[112] J. Martin, N. Rakotomalala, and D. Salin. Gravitational instability of miscible fluids in a Hele-Shaw cell. *Physics of Fluids*, 14 (2), 902–905, 2002.

[113] N. Goyal and E. Meiburg. Unstable density stratification of miscible fluids in a vertical Hele-Shaw cell: influence of variable viscosity on the linear stability. *Physics of Fluids*, 516, 211–238, 2004.

[114] H. Langer and H. Offermann. On the solubility of sodium chloride in water. *Journal of Crystal Growth*, 60 (2), 389–392, 1982.

[115] C. D. Green K. Ynickcih, and D. W. Sawyer. Pressure and temperature dependence of self-diffusion in water. *Faraday Discussions*, 66, 27–42, 1978.

[116] J. S. Kim, Z. Wu, A. R Morrow, A. Yethiraj, and A. Yethiraj. Self-diffusion and viscosity in electrolyte solutions. *The Journal of Physical Chemistry* , 116, 12007–12013, 2012.

[117] K. J. Muller and H. G. Hertz. A Parameter as an indicator for water-water association in solutions of strong electrolytes. *The Journal of Physical Chemistry* , 100, 1256–1265, 1996.

[118] G. Leal. *Advanced transport phenomena: fluid mechanics and convective transport processes*. Cambridge University Press, 2007.

[119] B. Eckhardt, T. M. Schneider, B. Hof, and J. Westerweel. Turbulence transition in pipe flow. *Annual Review of Fluid Mechanics*, 39, 447–468, 2007.

[120] L. P. Dake. Fundamentals of reservoir engineering. *Elsevier*, 8, 1983.

[121] A. Amiri, F. Larachi, and S. M. Taghavi. Buoyant miscible displacement flows in vertical pipe. *Physics of Fluids*, 28 (10), 102105, 2016.

[122] K. C. Sahu and S. P. Vanka. A multiphase lattice Boltzmann study of buoyancy-induced mixing in a tilted channel. *Computers & Fluids*, 50 (1), 199–215, 2011.

[123] N. Goyal and E. Meiburg. Miscible displacements in Hele-Shaw cells: two-dimensional base states and their linear stability. *Journal of Fluid Mechanics*, 558, 329–355, 2006.

[124] M. O. John, R. M. Oliveira, F. H. C. Heussler, and E. Meiburg. Variable density and viscosity, miscible displacements in horizontal Hele-Shaw cells. Part 2. Nonlinear simulations. *Journal of Fluid Mechanics*, 721, 295–323, 2013.

[125] R. Govindarajan and K. C. Sahu. Instabilities in viscosity-stratified flow. *Annual Review of Fluid Mechanics*, 46, 331–353, 2014.

[126] L. J. Tichacek, C. H. Barkelew, and T. Baron. Axial mixing in pipes. *AIChE Journal*, 3 (4), 439–442, 1957.

[127] B. Ebrahimi, P. Mostaghimi, H. Gholamian, and K. Sadeghy. Viscous fingering in yield stress fluids: a numerical study. *Journal of Engineering Mathematics*, 97, 161–176, 2016.

[128] J. V. Fontana, S. A. Lira, and J. A. Miranda. Radial viscous fingering in yield stress fluids: onset of pattern formation. *Physical Review E*, 87, 013016, 2013.

[129] J. V. Fontana and J. A. Miranda. Finger competition in lifting Hele-Shaw flows with a yield stress fluid. *Physical Review E*, 88, 023001, 2013.

[130] P. R. de Souza Mendes, E. S. S. Dutra, J. R. R. Siffert, and M. F. Naccache. Gas displacement of viscoplastic liquids in capillary tubes. *Journal of Non-Newtonian Fluid Mechanics*, 145 (1), 30–40, 2007.

[131] D. A. de Sousa, E. J. Soares, R. S. de Queiroz, and R. L. Thompson. Numerical investigation on gas-displacement of a shear-thinning liquid and a viscoplastic material in capillary tubes. *Journal of Non-Newtonian Fluid Mechanics*, 144, 149–159, 2007.

[132] H. M. Caliman, E. J. Soares, and R. L. Thompson. An experimental investigation on the Newtonian–Newtonian and viscoplastic–Newtonian displacement in a capillary tube. *Journal of Non-Newtonian Fluid Mechanics*, 247, 207–220, 2017.

[133] A. Salehi-Shabestari, A. Ahmadpour, M. Raisee, and K. Sadeghy. Flow and displacement of waxy crude oils in a homogeneous porous medium: a numerical study. *Journal of Non-Newtonian Fluid Mechanics*, 235, 47–63, 2016.

[134] A. Salehi-Shabestari, M. Raisee, and K. Sadeghy. Immiscible displacement of viscoplastic waxy crude oils: a numerical study. *Journal of Porous Media*, 20 (5), 2017.

[135] J. F. Freitas, E. J. Soares, and R. L. Thompson. Immiscible Newtonian displacement by a viscoplastic material in a capillary plane channel. *Rheologica Acta*, 50, 403–422, 2011.

[136] C. Gabard and J. P. Hulin. Miscible displacements of non-Newtonian fluids in a vertical tube. *European Physical Journal E*, 11, 231–241, 2003.

[137] V. Nirmalkar, R. P. Chhabra, and R.J. Poole. Laminar forced convection heat transfer from a heated square cylinder in a Bingham plastic fluid. *International Journal of Heat and Mass Transfer*, 56 (1–2), 625–639, 2013.

[138] J. Y. Kim, J. Y. Song, E. J. Lee, and S. K. Park. Rheological properties and microstructures of Carbopol gel network system. *Colloid and Polymer Science*, 281, 614–623, 2003.

[139] C. H. Lee, V. T. Moturi, and Y. Lee. Thixotropic property in pharmaceutical formulations. *Journal of Controlled Release*, 136, 88–98, 2009.

[140] F. K. Oppong and J. R. de Bruyn. Diffusion of microscopic tracer particles in a yield-stress fluid. *Journal of Non-Newtonian Fluid Mechanics*, 142 (1–3), 104–111, 2007.

[141] P. R. de Souza Mendes and E. S. S. Dutra. Viscosity function for yield-stress liquids. *Journal of Non-Newtonian Fluid Mechanics*, 14 (6), 296–302, 2004.

[142] K. Huang, J. W. Wan, C. X. Chen, Y. Q. Li, D. F. Mao, and M. Y. Zhang. Experimental investigation on friction factor in pipes with large roughness. *Experimental Thermal and Fluid Science*, 50, 147–153, 2013.

[143] R. Glowinski and P. Le Tallec. Augmented Lagrangian and operator-splitting methods in nonlinear mechanics. *Physics of Fluids*, 19, 084106, 2007.

[144] A. Roustaei. Yield stress fluid flows in uneven geometries: applications to the oil and gas industry. *Ph.D. thesis*, University of British Columbia, 2016.

Annexe A

Lubrication model for 3-layer flow in plane channel geometry

In the main text of the paper, we considered the vertical pipe geometry, which was well suited to the experiment. For the purpose of comparison, we now turn to a 2D symmetric plane channel geometry in order to quantify the conditions of the stationary layer state, and to compare it with our pipe geometry calculations. The channel has height $\hat{D}$ and it is completely vertical, similar to the pipe. Similarly, a lighter fluid is displaced by a heavy fluid in the downwards direction. Analogous to our pipe geometry, and using Cartesian coordinates, the lubrication approach leads to a dimensionless evolution equation for the interface height, $y = h(Z, T)$:

$$\frac{\partial h}{\partial T} + \frac{\partial q}{\partial Z} = 0, \tag{A.1}$$

for which we find:

$$q = \left(-\frac{2}{3} h^6 h^4 - \frac{2}{3} h^3 + \frac{1}{8} h^2 \right) \chi + \frac{3}{2} h - 2h^3. \tag{A.2}$$

It is now straight forward to calculate the critical value of χ and h for which the entire flux passes through the heavy layer while the interface speed is exactly equal to zero. We find that for vertical symmetric plane channel geometry, the interface height of $h_s \approx 0.33$ is stationary at $\chi_s \approx 118$.

Annexe B

Concentration function coefficients

The functions in equation (2.5) can be analytically calculated as follows:

$$f_0 = 1, \tag{B.1}$$

$$f_1 = \frac{1}{480} \frac{\left(240y^2 \ln\left(\sqrt{(1-4y^2)}+1\right) + 120\sqrt{(1-4y^2)} - 240y^2 \ln\left(1-\sqrt{(1-4y^2)}\right)\right)}{\sqrt{(1-4y^2)}}, \tag{B.2}$$

$$f_2 = \frac{1}{480} \frac{\left(40\sqrt{(1-4y^2)} + 320y^2\sqrt{(1-4y^2)}\right)}{\sqrt{(1-4y^2)}}, \tag{B.3}$$

$$f_3 = \frac{\frac{1}{480}\frac{\left(15\sqrt{(1-4y^2)}+90y^2\sqrt{(1-4y^2)}+180y^4\ln\left(\sqrt{(1-4y^2)}+1\right)\right)}{\sqrt{(1-4y^2)}}}{-\frac{180y^4\ln\left(1-\sqrt{(1-4y^2)}\right)}{\sqrt{(1-4y^2)}}}, \tag{B.4}$$

$$f_4 = \frac{1}{480} \frac{\left(256y^4\sqrt{(1-4y^2)} + 6\sqrt{(1-4y^2)} + 32y^2\sqrt{(1-4y^2)}\right)}{\sqrt{(1-4y^2)}}. \tag{B.5}$$